Tuneable Magnetic Properties of 3d Transition Metals Using Carbon Allotropes

Shoug Mohammad Ali Alghamdi

School of Physics and Astronomy

University of Leeds

Submitted in accordance with the requirements for the degree of

Doctor of Philosophy

April 2019

This thesis is dedicated to my parents, my husband Bader Alhijhaji, and to my sons Bassam and Basiem.

Intellectual Property Statement

The candidate confirms that the work submitted is her own, except where work which has formed part of jointly authored publications has been included. The contribution of the candidate and the other authors to this work has been explicitly indicated below. The candidate confirms that appropriate credit has been given within the thesis where reference has been made to the work of others.

For all thesis, Dr. O. C*é*spedes provided guidance for experiments and data analysis. Design and optimisation of C_{60} is done by Dr. M.C. Wheeler and Dr. O. C*é*spedes. The figures 4.4 and 4.23 were obtained in collaboration with Mr. Alistair Walton. I contributed to samples growth and characterisation. Cross-sectional high resolution TEM measurements in Figures 4.19 and 4.20 were performed by Mr. John Harrington and Dr. Zabeada Aslam in Leeds Electron Microscopy and Spectroscopy centre-LEMAS. However, all analysis of this section was done by me.

Acknowledgements

My heartfelt gratitude goes to my supervisor Dr. Oscar Céspedes for guiding me through my PhD with his valuable insights, suggestions and eye for detail. Without his unlimited patience, encouragement and support this work would not have been possible.

I would also like to give special thanks to my co-supervisor Prof. Bryan Hickey for all his support and guidance, and to the rest of the academic staff, including Prof. Chris Marrows, Dr. Thomas Moore and Dr. Satoshi Sasaki, who helped and inspired me during many productive discussions.

I must especially thank Dr. Gavin Burnell and Dr. Mannan Ali, who motivated me by their strong dedication to their work and encouraged me to believe in my abilities. Special thanks also go to Dr. Mannan Ali for all his help in the lab during the early days of my PhD.

Particular gratitude goes to Dr. Fatma Al Ma'Mari, who gave freely of her support and encouragement throughout the research and kept me motivated and positive during the long days of writing up the thesis.

Thanks also to Dr. Wafa Ezzawam for being a wonderful listener and sharing the good times.

I am extremely grateful to Dr. May Wheeler, Dr. Tim Moorsom and Matthew Rogers for sharing their skill, expertise and knowledge during the experimental work.

I would also like to thank Amy Westerman, Dr. Katharina Zeissler, Dr. Kowsar Shahbazi, Dr. Risalat Khan, Kathryn Moran, Dr. George Stefanou, Sean Stansill, Matthew Vaughan, Benjamin Steele, Dr. Rowan Temple, Satam Alotibi, Mohammed Alyami and Alistair Walton for their help and cooperation during my PhD. Great appreciation goes to the cryogenic technicians in the group and to Brian Chesworth from the mechanics

workshop for our cake time on Thursdays!
I am grateful to all the members of the Condensed Matter Group for providing such a great working environment, and particularly thanks go to Taibah University for their financial support and giving me the opportunity to study in the UK.
Thank you to Prof. Ahmed A. Al-ghamdi for his encouragement to study abroad.
Finally, a big thank you to my parents, my husband, my lovely sons, and also to my sisters and brothers, for all their love and encouragement and for being always by my side.
Thanks everyone!

Abstract

This research describes changes in the magnetic properties of 3d transition metals with hybrid nanocarbon and molecular carbon interfaces. Sputtered amorphous carbon (a-C) offers a simple and cheap pathway to tune the magnetic properties of transition metal thin films for magnetic memories and different spintronic applications. Here, amorphous nanocarbon films were RF-sputtered. Annealing the films changed the structure from amorphous to nanocrystalline as determined by Raman spectroscopy. The RF-sputtered a-C films were then coupled with pure iron (Fe) and iron nitride ($Fe_xN_{(1-x)}$) to study the magnetic properties for both hybrid interfaces at different annealing temperatures. Before annealing, hybridisation at the Fe/a-C interface leads to magnetic softening, with a reduction in coercivity (H_c) up to a factor of 5 for a Fe/a-C/Fe trilayer and a 10-30% lower saturation magnetisation as a function of the metal film thickness. On the other hand, after annealing, inter-diffusion and graphitisation of the carbon layer results in increased coercivity, also by a factor of 5, with the highest energy product being of the order of 53 kJ per m^3 of iron in a 10 nm film annealed at 500 °C. Kerr microscopy images of the films show a reduction in domain size and increased pinning points after annealing. Similar results were obtained when Fe is doped with nitrogen, with a $BH_{(max)}$ of 9 kJ per m^3 in a 9 nm $Fe_xN_{(1-x)}$/with RF-sputtered a-C was annealed at 500 °C. RF-sputtered carbon overlayers and post-processing can therefore be used to tune the anisotropy, domain configuration and magnetic properties of metallic thin films in a synthesis methodology that, for some applications in thin film technologies, could be simpler and cheaper than the use of heavy noble metals and/or rare earths.

C_{60} was also coupled with Fe and Co and the resulting Fe/C_{60} bilayer

samples show changes in H_c after annealing when the metallic layer is > 4 nm. Low temperature experiments at Co/C_{60} exhibited massive increases in coercivity (H_c). The H_c also rose as a result of annealing the film. Low temperature MR measurements point to an exchange spring effect. The research findings emphasise the importance of the hybridisation effects between the nanocarbon and molecular π orbitals and 3d bands of metals in controlling the magnetic properties at the interfaces before and after annealing.

CONTENTS

Abbreviations

AC	alternating current
a-C	amorphous carbon
AMR	anisotropic magnetoresistance
AFM	atomic force microscopy
BH_{max}	magnetic energy product
DC	direct current
DOS	density of states
DW	domain wall
E_F	Fermi energy
FC	field cooled
FCC	face centred cubic
FM	ferromagnet
HOMO	highest occupied molecular orbital
LUMO	lowest unoccupied molecular orbital
MR	magnetoresistance
OSC	organic semiconductor
RE	rare earth
RF	radio frequency
SQUID	superconducting quantum interference device
SOC	spin orbit coupling
TEM	transmission electron microscopy
VSM	vibrating sample magnetometry
XRD	x-ray diffraction
XRR	x-ray reflection

CHAPTER 1

Introduction

Spintronics is one of the most active areas of physics research and is a fast-growing discipline of science and technology due to the high speed and low power consumption required in computing [1–3]. Recently, much attention has been paid to the use of the organic semi-conductor (OSC) in spintronics [2–8] because of the interesting properties of molecular materials, for instance mechanical [9–12] and chemical flexibility [6]. Utilising OSCs has added new features and functions to the new spintronic devices that conventional semiconductors cannot provide [10–14]. This is due to the low-spin orbit coupling and low hyperfine interaction in OSCs [15]. The spin-orbit coupling in most OSCs is very small due to their small atomic number [Z], where the strength of the spin-orbit interaction is proportional to Z^4 [16–18]. Moreover, the hyperfine interaction is also weak in the absence of hydrogen, given the π-conjugated nature of transport molecular orbitals as well as the deficiency of the magnetic moment in the ^{12}C nuclei [18]. Consequently, the spin polarisation of the carriers is anticipated to be maintained for prolonged periods ($\sim 1\mu$s) [4, 18].

Over the years, many types of organic semiconductor were used as spin transport layers in devices [19]. In 2002, the first organic spintronic device was fabricated by Dediu et al. They engineered a device containing two $La_{0.7}Sr_{0.3}MnO_3$ (LSMO) electrodes, separated by a 70-500 nm narrow channel of sexithieny1 (6T). A strong magnetoresistance (MR) of about 30% was measured at room temperature for 100-200 nm 6T channel lengths. A spin diffusion length of 200 nm was estimated in this organic layer at room temperature [16, 20]. Many researchers carried on their studies on devices with the same construction using Alq_3 and other OSCs as a spacer layer. Various signs and magnitudes of MR were obtained even within devices of the same structure such as LSMO/Alq_3/Co [21]. These variations in results are evidence of the effect of the interface properties [21]. OSCs have paved the way for the creation of new spintronic devices with multi-functional behaviour, facilitating the sensing of electrical, magnetic, chemical and optical stimuli [18].

The hybrid interface effect plays a key role in spin-based technologies relying on molecular interfaces [22]. The effect of hybridisation at FM/organic interfaces has attracted significant attention over the last few years due to its potential in spintronic

applications [4, 21, 23]. The key role of charge transfer across metal/organic interfaces has been investigated previously [21, 24, 25]. Charge transfer and hybridisation between the π-carbon orbitals and the d-orbitals of transition metals leads to the formation of hybrid metal-carbon states, so the magnetic properties can be altered due to spin-polarised charge transfer [8, 9, 26–28].

C_{60} has a strong effect on the magnetisation reversal at Fe/C_{60} interfaces grown on MgO substrates and capped by 3 nm of Ta. Mallik et al. have reported an induced magnetic moment in non-magnetic fullerenes of about 2.95 μ_B per cage, which was observed at the interface of an Fe(15nm)/C_{60}(40nm) bilayer. This induced magnetic moment in C_{60} indicates a spin-polarised charge transfer at the Fe/C_{60} interface [29]. The hybridisation underlines the importance of chemical tuning of OSC/ferromagnetic interfaces via hybridisation between molecular orbitals and 3d bands in Fe [30]. X-ray absorption spectroscopy has shown significant hybridisation between 3d bands in Fe and C_{60} orbitals in a C_{60}/Fe(001) system. C_{60}/Fe(001) were prepared on MgO substrates and annealed at 450 °C for one hour [31]. The Fe_3O_4/C_{60} interface showed the induced magnetic moment of C_{60} due to the electronic interaction between the π orbital in C_{60} and 3d bands in Fe_3O_4 [26]. Recently, Al MaMari et al. investigated the emergent magnetism at room temperature between non-magnetic transition metal elements through C_{60} molecular interfaces. It was shown that Cu(2 nm)/C_{60}(15 nm) and Mn(5 nm)/C_{60}(15 nm) thin films exhibited ferromagnetic behaviour at room temperature with magnetisation of 50 emu/cm^3 and 15 emu/cm^3 respectively. The hybridisation at the interfaces leads to a change in the DOS due to charge transfer across the metal/molecular interface [27]. Hybrid magneto-C_{60} interfaces have been studied in bilayer and multilayer thin films of Co/C_{60}. The results indicate a reduction in the magnetisation of the Co while inducing magnetisation in C_{60} [32]. This is due to the molecule becoming doped with spin polarised electrons when in contact with the ferromagnetic metal [32]. A Ni/graphene interface has also been studied and the results show a strong hybridisation effect between the graphene π and 3d bands in Ni [33].

First measurements in carbon nanotubes investigated by Céspedes et al [34] gave evidence for contact-induced magnetism at the interface between a ferromagnet and

carbon nanotube [34]. Coupling metal films with carbon layers can enhance the graphitisation of carbon [35–38]. Graphitisation is a change that can occur when heated between 425 °C and 600 °C for long periods of time [39, 40]. The graphitisation in a-C/Co/a-C trilayer has been observed. A study using transmission electron microscopy (TEM) confirmed the role of annealing temperature in fully crystallising the samples between 500 °C and 600 °C, and the TEM showed the diffusion of a-C in this system [41, 42]. In addition, increasing the annealing temperature caused an increase in the coercivity (H_c) from 510 Oe to 650 Oe. This effect was obtained in a carbon/cobalt alloy (CoCrPt)/carbon system, and the thin film was annealed at 400 °C and 600 °C for 2 hours. The coercivity (H_c) showed a slight increase as the annealing temperature was increased. The coercivity value for the as-deposited sample was 510 Oe and rose to 650 Oe for the annealed sample at 600 °C [41]. Fe/C thin films were also deposited on SiO_2 glass substrates and the effect of annealing the substrates during the deposition process was investigated. The coercivity rose to 200 Oe as the temperature of the substrate was increased to 350 °C. On the other hand, Fe_3C films demonstrated an increase in Ms as the substrate temperature was increased. This indicated that the thin films crystallised according to the increase in temperature [43].
Wu et al. fabricated Fe/Fe_3C composites that showed changes in ferromagnetic properties after annealing. The magnetisation increased when the composites were annealed at 700 °C. Due to change in the reaction time that can be also attributed to an increase of the coercivity of about 200 Oe at 650 °C [44].
TEM has also been used to investigate the reaction between amorphous carbon and Fe. Annealing a-C/Fe/a-C at 500 °C produces more diffraction spots and drops the intensity of bcc iron rings. When the rings are complete, this indicates the formation of a continuous layer of cementite (the iron carbide phase) and exists below 550 °C as expected. However, as the annealing temperature is brought up to 550 °C (Fe_3C), a-C atoms diffuse into the Fe layer and eventually create a nano-graphitic phase [45].

Magnets are required in many everyday applications, from sensing to computing and information storage [46, 47]. Rare earth elements such as Gd, Nd or Dy are combined with ferromagnetic materials such as iron or cobalt to produce compounds that have big hysteresis loops with high coercivities and energy products [48]. At the same time, noble metals such as Pt or Ir are used to change the anisotropy and magnetic

structure of thin films for magnetic storage applications [49, 50]. In order to meet future energy needs, many studies have been carried out on different systems. For example, FePt nanocrystals protected via an encapsulating graphite shell, show increased H_c measurements of up to 2.5 kOe at room temperature. Annealing the FePt nanoparticles can produce a H_c of up to 30 kOe [50]. Compounds of FM material with rare earth elements, such as neodymium iron boron, aluminium nickel cobalt (Alnico) and samarium cobalt (Sm-Co) leads to increase the $(BH)_{max}$ [47, 48]. For example a typical composition of $Nd_{17}B_8Fe_{77}$ has a high energy product of about $(BH)_{max}$ = 290 kJ/m^3 [51]. Cobalt (Co) can become harder when in contact with rare earth elements, and attain a coercivity of up to (3-5) kOe useful for data storage applications [52, 53]. Studying the effect of annealing on the magnetic properties of Co/Gd multilayers with different number of repeats has shown a rise in coercivity from 15 Oe to 50 Oe at 427 °C due to inter-diffusion at the Gd/Co interface [54]. Lee et al. investigated the effect of annealing temperature on the magnetic properties of Pt/Co. The saturation magnetisation (Ms) in Pt(0.2 nm)/Co(t_{Co}) increased with the thickness of the Co layer, but was slightly reduced when it was annealed at 400 °C. This was due to the intermixing of Co and Pt during annealing [55].

In the present thesis we focus our investigations on systems with RF-sputtered amorphous carbon (a-C). In the development of technological applications using thin films, amorphous carbon (a-C) has some ideal qualities, including the extremely low price of the target material, low thin film roughness when deposited at room temperature, and compatibility with the growth of layers sensitive to degradation. Furthermore, amorphous carbon thin films display mechanical, chemical, and optical features, which are accredited to the flexibility of the sp^1, sp^2 and sp^3 concentration hybridisation sites [56]. We have also involved C_{60} in our investigations because of its higher spin-orbit interaction due to the curvature of the molecule [17]. The spin lifetime increases due to the very weak hyperfine interaction in C_{60} [57] and thus C_{60} molecules have an advantage over other organic materials containing hydrogen, which have a stronger hyperfine interaction.

The research investigated the structure and growth conditions of RF-sputtered amorphous carbon (a-C) thin films on Fe in order to obtain a better understanding of their

characteristics and magnetic properties.

Chapter 2 outlines the theoretical background to the experimental work and sets out some of the findings of previous studies in the field. Firstly, we describe the basic concept of carbon and its allotropes, and discuss details of the magnetism between ferromagnetic materials and nanocarbon. Some concepts related to magnetism such as exchange energy, the fundamentals of magnetic anisotropy, domain wall formation and energy product are discussed.

Chapter 3 describes the experimental techniques used in this research, including sample growth, structural, magnetic and transport characterisation. For sample growth, we discuss the deposition of RF-sputtered a-C samples by RF magnetron sputtering, DC magnetron sputtering, and the in-situ thermal sublimation of C_{60}. The annealing process also plays an important part in our investigations as we document the effect of annealing on the magnetic properties of the samples. X-ray reflectivity (XRR) is used to study the structure of the samples and determine the thickness and roughness of films. Raman spectroscopy is also used to study the bonding structure in carbon before and after annealing. The magnetic properties are obtained using superconducting quantum interference device (SQUID-VSM) magnetometry and Kerr microscopy. Low temperature transport measurements are taken to investigate the AMR effect in Co/C_{60} thin films.

This research seeks to fine tune the magnetic properties in order to obtain a high $(BH)_{max}$. The interfacial effect between RF-sputtered a-C and transition metals is addressed in two chapters: Chapter 4 discusses Fe/RF-sputtered a-C interfaces and Chapter 5 deals with $Fe_xN_{(1-x)}$/RF-sputtered a-C interfaces. These chapters focus on the structure and magnetic properties of thin films before and after annealing. Information about the carbon structure is obtained by Raman spectroscopy before and after annealing. The magnetisation and coercivity results were obtained using SQUID and the formation of the domains was observed using Kerr microscopy before and after annealing the samples. The results obtained by each method are discussed in detail in these chapters.

In Chapter 6, we present the results of using low temperature transport and magnetometry to study the interfacial properties of transition metals and C_{60}. The magnetic properties at Fe/C_{60} interfaces and Co/C_{60} interfaces at room temperature, different annealing temperature and low temperature are discussed in detail. Magneto-transport measurements were taken to investigate the domain wall anisotropic magnetoresistance effect on the Co/C_{60} system and to confirm the data obtained via SQUID-VSM.

In Chapter 7 we briefly summarise the experimental findings of this research and suggest directions for future work.

CHAPTER 2

Theoretical Background

2.1 Introduction

The hybrid interface between 3d transition ferromagnetic metals and nano-carbon plays a significant role in altering the magnetic properties of 3d transition metals [58]. In this chapter we discuss carbon and its allotropes, and introduce the topic of magnetism in ferromagnetic metals (FM) - nanocarbon and the use of nanocarbon to tune magnets. We also explain the exchange interaction and discuss magnetic anisotropy, which is a major feature of this research. Finally, we illustrate the formation of domains structure and discuss the magnetic energy product.

2.2 The Element Carbon and its Allotropes

2.2.1 Carbon Bonding

The element carbon has broad industrial and scientific applications [59] and appears in various allotropes such as diamond, fullerenes and graphite [60, 61]. Although the potential for allotrope formation is not exclusive to carbon, the properties of its allotropes are exceptionally diverse compared to those of other Group IV elements. For example, diamond is the hardest naturally-occurring substance, transparent to the visible spectrum, and an electrical insulator, while graphite is a opaque electrical conductor. Fullerenes are different again, being a family of large carbon molecules with stable forms, in contrast to the unlimited networks of graphite and diamond. This wide range of features is a consequence of how the atomic orbitals in carbon are hybridised during chemical bond formation [62].

In order to understand the formation of different carbon-based materials, we first need to look at the electronic configuration of the element. Carbon has an electronic configuration of $1s^2\ 2s^2\ 2p^2$ in its ground state. It has 4 L shell electrons, where the atomic orbitals 2p and 2s within the carbon atom can experience three distinct hybridisations designated as sp^3, sp^2, and sp^1 [60, 63] as illustrated in Figure 2.1 [64].

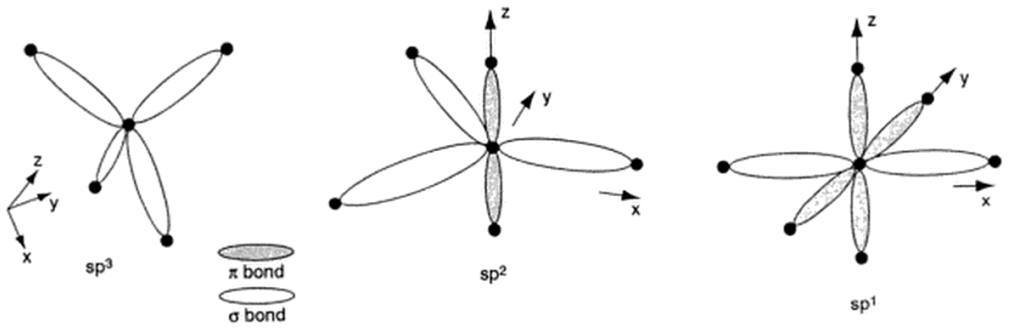

Figure 2.1: Hybridisations in carbon, designated as sp^3, sp^2, and sp^1. The σ and π bonds act as the lower energy bonding molecular orbitals (σ and π) Diagrams taken from [64].

A single 2s orbitals and two of three 2p orbitals of carbon are joined in sp^2 hybridisation to create three sp^2 orbitals [62]. Moreover, sp^2 hybrid orbitals are trigonally expressed in planes at angles of 120° from each other (Figure 2.2), and possess one valence electron in every orbital. The other valence electrons are placed in the rest of the 2p orbitals, having a perpendicular axis to the plane of the 3 sp^2 orbitals [62]. The 3 sp^2 hybrid orbitals within the carbon atom create 3 σ bonds, having the orbitals in nearby molecules or atoms [60]. The sp^2 atom's fourth electron lies in a p-π orbital, which is positioned normal to the σ bonding plane. A weaker bond is formed by this π orbital, having an π orbital in either one or more nearby atoms [65].

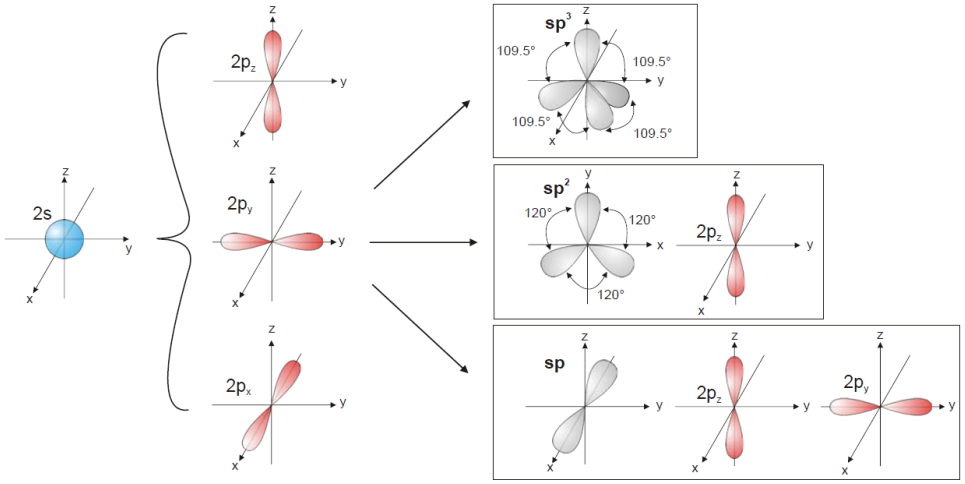

Figure 2.2: Linear combinations of the carbon outer orbitals (2s, $2p_x$, $2p_y$ and $2p_z$), which can be taken to provide the hybridised sp^3-sp^2- or sp-orbitals, which create σ-bonds with other atoms. The rest of the unhybridised p-orbitals create π-bonds with the atoms nearby. Taken from [60].

Due to hybridisation, π bonds are formed by the lateral overlap of p orbitals along a plane perpendicular to the inter-nuclear axis. The π bonds have delocalised electrons over the single molecule, and due to this delocalisation electron transport can happen by interaction between the π-orbitals of adjacent molecules. A strong covalent σ-bond can be formed between adjacent carbon atoms with hybrid orbitals by the overlap of molecular orbitals along the inter-nuclear axis. However, the σ bonds are localised and are not responsible for the electron transport.

2.2.2 Carbon allotropes and sputtering

Carbon, as noted, possesses exceptional capacity to undergo various hybridisations. Thus, carbon can create various structures with different geometries and fractions of sp^3 and sp^2 bonding in both crystalline as well as non-crystalline forms (Table 2.1). The features and structures of the two crystalline carbon forms are well known, graphite having fully (100%) sp^2 bonding and diamond having 100% sp^3 bonding. The non-crystalline stage of carbon is a combination of sp^2 and sp^3 orbitals with features

between those of graphite and diamond. Features of some carbon allotropes are shown in Table 2.1 below [62].

Table 2.1: Features of different forms of carbon, a-C denotes amorphous carbon. Taken from [62].

	Density ($g.m^{-3}$)	Hardness (GPa)	sp^3%	Hydrogen%	Band gap (eV)
Diamond	3.515	100	100		5.5
Graphite	2.267	-	0		0
Evaporated a-C	1.9-2.0	2-5	<5		0.4-0.7
Hard a-C:H	1.6-2.2	10-40	30-60	20-40	0.8-1.7
Soft a-C:H	0.9-1.6	<5	50-80	40-65	1.6-4

The compositions of different amorphous carbons can be exhibited in a ternary stage diagram (Figure 2.3). Normally, only sp^3 and sp^2 sites are found in amorphous carbon, with the possibility of nitrogen and hydrogen being present [62]. An amorphous carbon (a-C) thin film can be described as a network of disordered carbon stages with medium and short-range order [65]. Furthermore, amorphous carbon thin films display mechanical, chemical, optical and thermal features which are attributed to the flexibility of the sp^1, sp^2 and sp^3 concentration hybridisation sites as well as the atomic connectivity inside the carbon network [65].

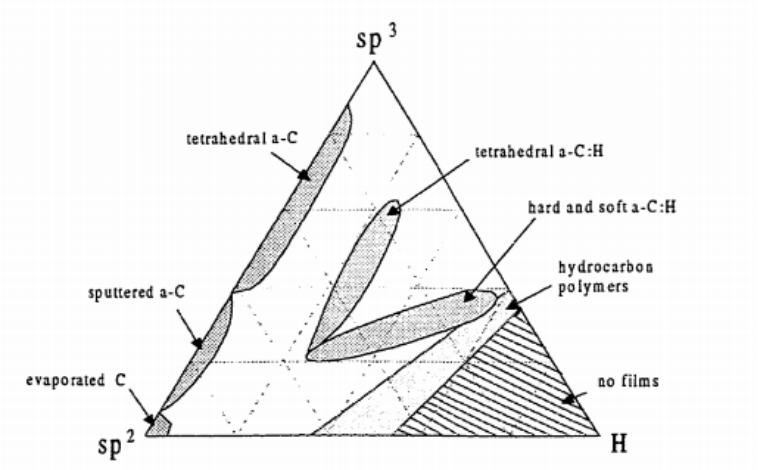

Figure 2.3: The compositions of amorphous carbon as well as hydrogenated amorphous carbon, adapted from [62].

C_{60}(buckminsterfullerene or buckyballs) is a carbon-based organic semiconductor. It was discovered by Kroto et al in 1985 [66]. Buckminsterfullerene has attracted much attention in the field of molecular spintronic devices because it can easily form high quality films by thermal sublimation without damage from any metals deposited on the top [66, 67]. The Fermi levels of ferromagnetic materials are higher than the lowest unoccupied molecular orbital (LUMO) levels of C_{60}, which means that spin is easily injected compared to other organic materials [68, 69]. C_{60} is made up of 20 hexagonal and 12 pentagonal faces and it is a close spherical cage molecule as shown in Figure 2.4.

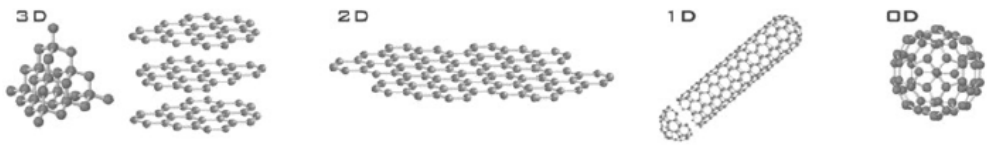

Figure 2.4: Carbon and its allotropes: 3D diamond lattice and graphite, 2D graphene. 1D single wall carbon nanotube, 0D C_{60} or buckyball. Diagrams from [70].

The crystal structure of C_{60} is face-centred cubic (FCC) at room temperature. It also has a disordered structure and natural diamagnetic properties. It sets an induced magnetic dipole moment to the external magnetic field. Below temperatures of 260 K, crystalline C_{60} molecules reorientate themselves in an inequivalent fashion on the Bravais sites of the FCC lattice. This first order change transition produces a simple cubic structure. If the temperature decreases to 90 K and below, the rotational degrees of freedom become frozen [71].

The properties of buckminsterfullerene are listed in Table 2.2 and are dependent on growth conditions. C_{60} has a high electron affinity of about 2.6 eV [70, 72, 73] and low LUMO (the lowest unoccupied molecular orbital) [69, 74] which leads to a strong increase in the charge transfer. The magnetism appearing in Tetrakis (dimethylamino) ethylene [TDAE]-C_{60} was found to emerge from this type of charge transfer mechanism [75]. The relative orientations of the C_{60} molecules play an important part in the charge transfer occurring at temperatures below 16 K [76]. The charge transfer and the hybridisation effect could lead to a change in the magnetic properties at transition metal-nanocarbon interfaces [27, 58].

Table 2.2: Properties of C_{60} [70].

Property	Value
crystal structure	FCC
density (g/cm^3)	1.65
lattice constant (Å)	14.5
sublimation temperature (K)	800
conductivity	n-type semiconductor
resistivity (Ω m)	1 x 10^{14} room temperature
electron affinity (eV)	2.6
Fermi energy for HOMO (eV)	6.2
Fermi energy for LUMO (eV)	4.5

2.3 Magnetic ordering at metallo-molecular interfaces

Understanding the basic principles of hybrid interfacial states has been a recent research focus [3]. The study of hybrid interfaces between inorganic materials has broadened to include interfaces between inorganic and organic substances. For example, observations show that magnetism is induced at the interfaces of ferromagnetic materials and carbon nanotubes [34]. Hybridisation is characteristic of the chemical bonds which appear at the interface of a magnetic surface and organic molecules, and has been investigated [8, 21]. Steil and colleagues have explained the mechanism of the charge carrier transfer that occurs across the ferromagnetic material/organic interface and have also clarified the role of hybrid states in efficient spin filtering properties [77].

2.3.1 Organic molecules in magnetism

Identifying the uses of organic molecules in magnetism has become an important focus in recent years [78–80]. McConnell's design for a ferromagnetic (FM) molecular solid was the first theoretical work in this area [81]. He introduced the idea that ferromagnetic spin coupling occurs in a molecular system. It appears when a region of negative spin density in one molecule overlaps with a region of positive spin density in another molecule leads to the incomplete cancellation of anti-ferromagnetic coupled spin components. A new term in the Hamiltonian has been used to support the above mechanism. An interaction appears between two neighbouring molecules A and B

$$\hat{\mathcal{H}} = -2S_A S_B \sum_{ij} J_{ij} \rho_A^i \rho_B^j \tag{2.1}$$

where S_A and S_B together are the total spins on molecules A and B , and ij are coupled by exchange interaction J_{ij} where i and j indicate the atoms located in molecules A and B. ρ_A^i and ρ_B^j are the spin densities on atoms i and j. If the magnetic coupling is negative, then the two neighbouring molecules (A and B) will show a ferromagnetic exchange interaction, if the interaction atoms for the spin densities have opposite signs (negative product) that exhibit a positive coupling due to the limitation of this mechanism. The second mechanism developed by McConnell further explains the alignment of the spin in charge transfer complexes that the excited triplet states propagate along a

donor and acceptor molecule and gives rise to the magnetic ordering [82]. This opens new pathway to altering the magnetism via organic molecules [58].

2.3.2 The use of molecules to tune magnets

Efforts have been made to understand how to engineer the magnetism generated by organic molecules. The spin-dependent density of states of a molecule can be modified by contact with an inorganic ferromagnetic interface. This interfacial effect becomes more complicated when a hard, metallic electrode makes contact with a soft organic layer [83, 84]. Barraud et al [21] found that the nature of spin injection into molecules depends on the chemical bonds between the organic and the magnetic electrodes at the interface. They also noted that these chemical bonds can be engineered to provide good control over the properties of spintronic devices [21].

The hybrid metal-nanocarbon states are created due to hybridisation between the d-orbitals of metals and the π carbon orbitals, as well as charge transfer that affects the magnetic properties in the system owing to a spin polarised charge transfer [28].

Bairagi et al [28] observed a strong increase in interfacial magnetic anisotropy in C_{60}/Co(0001) and decrease in perpendicular magnetic anisotropy (PMA) in C_{60}/Fe(110). An increase in H_c indicated a 3.2 ML Co film with C_{60} coverage (ML) as shown in Figure 2.5a. This enhancement can be related to an increase of the out-of-plane magnetic anisotropy. However, the magnetisation is reduced due to the hybridisation between C atoms and d-orbitals of Co and give a sign of the reduction of magnetic moment in the Co (Figure 2.5a). A change in the effective anisotropy (K_{eff}) of the 6.4ML Co film has been demonstrated as a function of C_{60} coverage (ML) as shown in Figure 2.5b. The data shows Δ (K_{eff}) fully saturated at around 0.7 ML of C_{60}, and below 0.7 the magnetic anisotropy energy (MAE) undergoes a change that can be induced by the hybridisation between Co and C_{60} [28]. By Gruber et al [85] recorded that in the magnetic coupling at room temperature between Co and MnPc (manganese phthalocyanine), molecules were separated by a Cu spacer. The magnetisation amplitude and direction of the molecules were tuned by changing the thickness of the Cu and improved according to an interlayer exchange coupling mechanism as presented in Figure 2.5c [85].

The interface between tris(8-hydrixyquinolate) aluminium (Alq_3) and the magnetic

electrode NiFe was investigated by Morley et al [86]. The results indicate a change in the coercivity of different NiFe thickness coupled with 10 nm of Alq_3 as shown in Figure 2.5d . The H_c decreases when the metallic layer become thick due to a strong bonding at NiFe/Alq_3 interfaces. Morley et al, also showed that the coercivity of the NiFe (10 nm) films is smaller than Fe (10 nm) when both coupled with poly(2,5-bis(3-hexadecylthiophen-2-yl)thieno[3,2-b]thiophene (PBTTT). This is because NiFe is magnetically soft [87].

Moorsom et al [32] documented VSM data on a Co/C_{60} bilayer sample and Co/Cu/C_{60} samples with a thickness of 2 nm Cu, 5 nm of Co and variations in the thickness of the C_{60} layer, all samples being measured at 100 K. Figure 2.5e shows that the coercivity of the Co/C_{60} bilayer samples is enhanced in comparison to the sample with a Cu spacer layer. This enhancement in coercivity is due to an antiferromagnetic coupling between the Co and the first layer of C_{60}. The saturation magnetisation (M_s) of the Co is decreased when Co is in contact with C_{60}, compared to when the Cu spacer layer is present. This can be related to the fact that the spin doping effect is interfacial and the introduction of the Cu spacer layer into the Co/C_{60} causes further quenching of this effect. Another possibility is that the charge is transferred from the Co layer to the C_{60} layer [32].

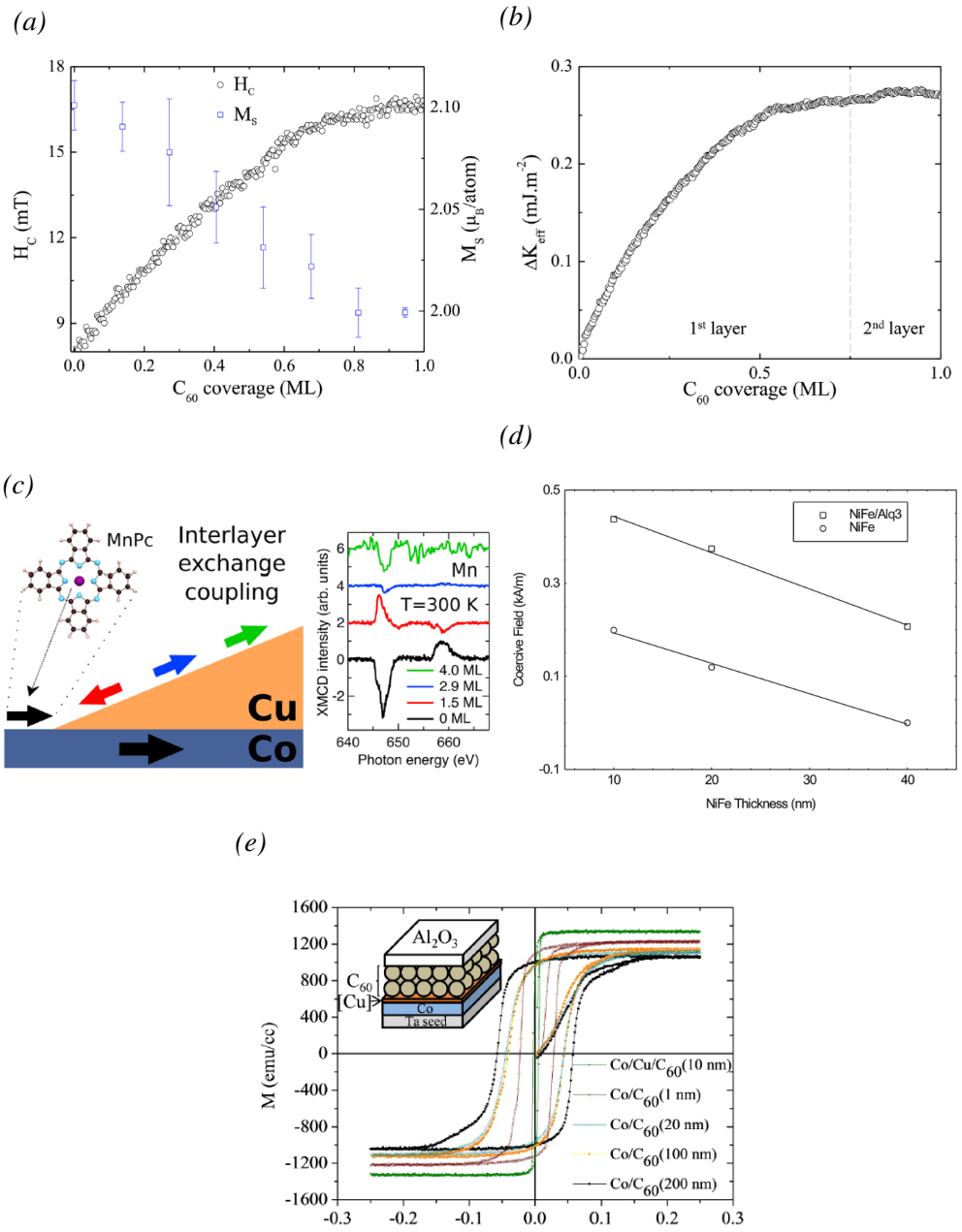

Figure 2.5: Shows (a) change in coercivity and saturation magnetisation as a function of C_{60} coverage for a 3.2 ML Co film, (b) change in the interfacial magnetic anisotropy against C_{60} coverage for a 6.4 ML Co film, (c) interlayer exchange coupling for the structure of Co/Cu(d_{Cu})/MnPc, (d) Coercivity as a function of NiFe thickness for a typical structure of NiFe/Alq_3 and NiFe films and (e) enhancement in the H_c of the Co(5 nm)/C_{60} system with different thicknesses of C_{60} measured at 100 K.Taken from [28, 32, 85, 86].

The molecules and inorganic materials are formed by molecular orbitals and a continuum of states, respectively. In organic semiconductors, the LUMO and the HOMO are the orbitals used in charge transfer in the system, whereas in inorganic crystals the valence and conduction bands are involved.

Two main bonding mechanisms, physisorption and chemisorption, can be observed when an organic molecular system comes in contact with metal surfaces. The physisorption mechanism is characterised by a weak adsorption energy of less than 0.1 V and the molecule to metal surface distance is large, at $\geq$ 3 Å. The chemisorption interaction, on the other hand, has a large adsorption energy of $\geq$ 0.5 V, and the distance from the molecule to the surface is $\leq$ 2.5 Å.

These interactions affect the surface of metals and the orbitals of the molecule, leading to changes in the magnetic and electronic properties at the metallo-molecular interfaces.

Weak van der Waals interactions [88] are used to characterise the physisorption mechanism and propose a broadening of the molecular electron levels owing to their proximity to the states of metals. The metallo-molecular interactions cause rearrangement of the electron density and the alignment of the orbitals adjusts closer to Fermi levels [7, 89, 90]. However, a new quantum mechanical system can be formed due to chemisorption between the surface of the metals and the orbitals in the molecule.Due to strong hybridisation and charge transfer between π-d interfacial states. The π-d are molecular orbitals (π orbitals) and the metallic states (d-states) [83].

Therefore, in studying the interfaces between organic molecules and inorganic ferromagnetic materials, we need to understand the effects on the density of states (DOS) of both materials. On the one hand, the DOS in ferromagnetic metals (metallic surface) is broad and the spins are split into majority (spin-up) sub-band and minority sub-band (spin-down) electrons, as shown in Figure 2.6. On the other hand, the DOS in the organic material is made up of discrete molecular energy levels, so that only the LUMO is close enough to the Fermi energy (E_F) of the metallic surface. If there is no interaction at the hybrid interface between the ferromagnetic metal and the organic molecule, then the electronic structure is a superposition of each density of state of the two spin components. However, when the organic molecule comes into contact with the ferromagnetic metal, the density of states is altered in two ways.

Firstly, the molecular orbitals become broader, owing to electrons leaking in and out of

the molecule, leading to a broadening of the DOS. This broadening effect depends on the interaction at the interface, where proximity and symmetry of the molecular levels have an important effect on the degree of interaction. Moreover, in the ferromagnetic material there is an imbalance in energy for the up and down spins. Thus, the molecular orbitals for up and down spin electrons are broadened by different amounts owing to different energy between up and down spin electrons in metals.
Secondly, the energy level in the molecular orbitals is shifted and this shift can be spin-dependent. The shifting can be aligned in a particular spin-polarised molecular orbital with the Fermi energy E_F, which here is the major dominating component, as shown in Figure 2.6. However, if the minority spin ends up at E_F, this leads to a change in the magnetic properties at the metallo-molecular interfaces [21, 83].

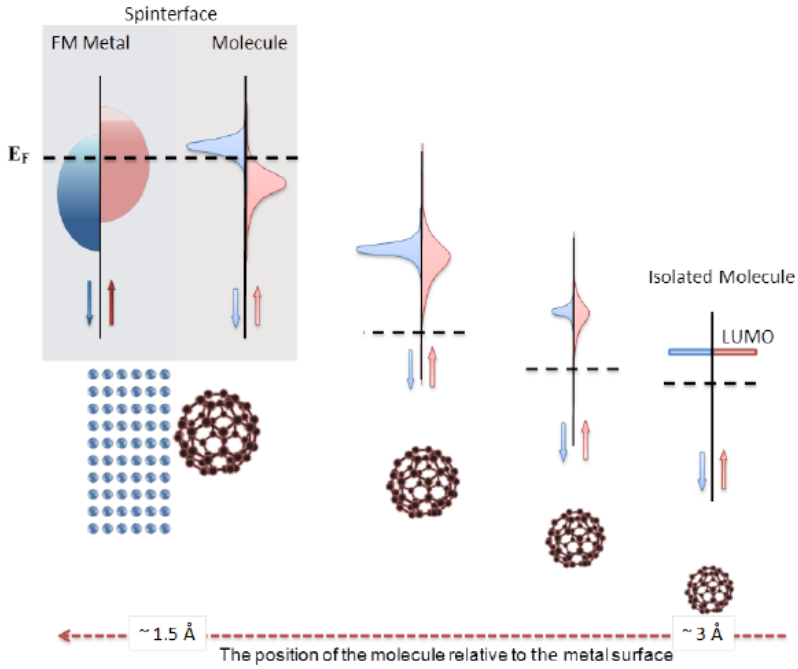

Figure 2.6: Hybridisation at the molecular and ferromagnetic metal interface. The molecule has discrete levels whereby the ferromagnetic metal is characterised via a band structure. The lower section shows the molecule C_{60} when it is closer to the metal surface, and the upper section represents the DOS of both the ferromagnetic metal (left) and the isolated molecule (right). When the physisorption and chemisorption interactions become stronger, coupling the isolated molecule to the FM metal changes the DOS of the isolated molecule. The initial discrete molecular orbitals broaden and shift their position to the Fermi level E_F of the FM metal as show on the left. Figure taken from [91].

2.4 Magnetic Anisotropy

The total energy of the ferromagnetic system has an exchange energy that can be described as a different energy between antiparallel and parallel spin orientations given by

$$E_{ex} = -2JS_1S_2 \tag{2.2}$$

where is J the exchange constant, S_1, and S_2 are spins. J is positive in the ferromagnetic system where the spins have parallel orientation. In ferromagnetic materials, the magnetisation may prefer a certain orientation (easy axis), which makes the material magnetically anisotropic. When the magnetisation is away from the easy axis energy is needed which is know as anisotropy energy [92]. Magnetic anisotropy in ferromagnetic materials is categorised by the crystal structure (magnetocrystalline anisotropy) and the shape of the film (shape anisotropy) [93, 94].

2.4.1 Magnetocrystalline (MC) anisotropy

Magnetocrystalline (MC) anisotropy leads the magnetisation to align in a certain crystallographic direction. The rotation become very hard when the coupling between the crystalline lattice and orbital motion of electrons is strong, thus higher energy is needed to rotate the magnetisation depending on the crystalline axes [95]. The samples in this case have a magnetisation in the particular direction of the crystalline axis (easy axis). During deposition, anisotropy can be induced in the thin film owing to the applied magnetic field creating a preferred axis. Depending on the shape of the lattice structure, there are two types of crystal anisotropy.
1- The crystalline anisotropy is dependent on the angle between a specific crystalline axis (θ) and the magnetisation. In a cubic lattice system, cubic anisotropy is observed. The most common examples are BCC iron and FCC nickel. The magnetocrystalline anisotropy energy is represented as

$$E = KV\left(\alpha_1^2\alpha_2^2 + \alpha_2^2\alpha_3^2 + \alpha_1^2\alpha_3^2\right) \tag{2.3}$$

where K is the anisotropy constant, V is the volume of the sample, and α is the cosine of the angle (θ) between M (magnetisation) and the crystal axis.

2- Uniaxial anisotropy will dominate a uniaxial hexagonal system such as that found in cobalt. It has an orientation-dependent energy, in this case the anisotropy energy is given by;

$$E = K_1 V \sin^2(\theta) + K_2 V \sin^4(\theta) + \ldots \tag{2.4}$$

where is θ is the angle between the magnetisation and the easy axis, and K_1,K_2 are first order and second order anisotropy constants [96, 97].

2.4.2 Shape anisotropy

At the surface of the material that is uniformly magnetised, the spin is aligned and magnetic charges are created by the discontinuous magnetisation at the surfaces. These charges result in a field with orientation opposite to the external applied magnetic field. This field is expressed as the demagnetising field H_d [98], which is dependent on the shape of the sample and proportional to the magnetisation given by

$$H_d = N_d M \tag{2.5}$$

where N_d is the demagnetisation factor. The shape anisotropy is written as,

$$K_d = 1/2 N \mu_0 M^2 \tag{2.6}$$

where M is the magnetisation and μ_0 is the magnetic permeability of free space.

Perpendicular anisotropy in thin film:
The total anisotropy energy in thin film is given by

$$E = K_{eff} V \sin^2 \theta \tag{2.7}$$

when K_{eff} is the effective anisotropy, and V is the volume of the sample,

$$K_{eff} = K_V + \frac{2K_s}{t} \tag{2.8}$$

In this equation the effective anisotropy is equal to volume anisotropy K_V and surface anisotropy K_s, and t is the thickness of the thin film. K_V includes a contribution from the shape anisotropy and another from the magnetocrystalline anisotropy. The orientation of the surface anisotropy K_s is perpendicular to the plane of the film. This depends on the structure of the atomic orbitals at the interface and the spin orbit interaction [99].

2.5 Exchange interaction

The behaviour of ferromagnetic materials is characterised by the spontaneous alignment of the magnetic moments with their neighbours to minimise the interaction energy between them. This magnetic ordering occurs at a specific critical temperature known as the Curie temperature T_c. Above this temperature the materials become paramagnetic. In paramagnetic materials, the spins are in a random orientation owing to the thermal energy. The exchange interaction can be explained by the Pauli exclusion principle [94] in terms of quantum mechanics. If two adjacent atoms overlap at the orbitals of outer valence electrons, the electrostatic energy forming the Coulomb interaction is minimised when the direction of spins are parallel to each other. This occurs due to the Pauli principle, two parallel spins cannot share a common orbital and thus they stay apart. Consider, two electrons (a) and (b) have space coordinates r_1 and r_2, and wave functions $\psi_a\ (r_1)$ and $\psi_b\ (r_2)$ respectively, then, the total wave function of the electrons is

$$\Psi_{1,2} = \psi_a\ (r_1)\psi_b\ (r_2) \tag{2.9}$$

The electrons are fermions and are indistinguishable, and the Pauli exclusion principle prevents fermions from occupying the same quantum state. So, the total ψ will be antisymmetric to exchange.

$$\Psi_{1,2} = -\Psi_{1,2} \tag{2.10}$$

In the electrons the total ψ is a product of the space and spin wave functions combining a symmetric spatial state with an antisymmetric spin wave function leading to the achievement of symmetry. The spin singlet state is $\chi_S\ (S{=}0)$ whereas the spin triplet state is $\chi_T\ (S{=}1)$. The total wave functions for these are Ψ_S and Ψ_T respectively, including the spatial and spin components as in the following equations,

$$\Psi_S = \frac{1}{\sqrt{2}}\left[\psi_a(r_1)\psi_b(r_2) + \psi_a(r_2)\psi_b(r_1)\right]\chi_S \tag{2.11}$$

$$\Psi_T = \frac{1}{\sqrt{2}}\left[\psi_a(r_1)\psi_b(r_2) - \psi_a(r_2)\psi_b(r_1)\right]\chi_T \tag{2.12}$$

The exchange energy E_{ex} is given by

$$E_S - E_T = 2 \int \psi_a^*(r_1)\psi_b^*(r_2)\hat{\mathcal{H}}\psi_a(r_2)\psi_b(r_1)dr_1dr_2 \tag{2.13}$$

where E_{ex} is the difference between the electrostatic energies of E_S for singlet states and E_T for triplet states, and $\hat{\mathcal{H}}$ is the Hamiltonian. A spin-dependent Hamiltonian can be written as,

$$\hat{\mathcal{H}} = -2\sum_{ij} J_{ij}\mathbf{S_1}.\mathbf{S_2} \tag{2.14}$$

where the exchange integral is $J<0$, $E_S < E_T$, in this case the singlet state is favoured. The spins are aligned antiparallel and indicate an antiferromagnetic interaction. When $J>0$ and $E_T < E_S$ this gives rise to a ferromagnetic interaction where the triplet state is favoured, and the spins are aligned in parallel [94, 100].
In 1938, Edmund Stoner [101] identified a criterion to predict the itinerant ferromagnetism of metals at room temperature. The Stoner criterion states that ferromagnetism appears when the exchange energy is greater than the kinetic energy as result of flipping a spin. The three elements that satisfy the Stoner criterion are iron (Fe), cobalt (Co) and nickel (Ni), which have spontaneous ferromagnetism at room temperature. Other transition metals exhibit diamagnetic or paramagnetic interactions. The magnetic moments in ferromagnetic materials align to a given direction because of the exchange interaction between them.
The Stoner criterion explains why some transition metals are ferromagnetic while others are not, despite having an unfilled 3d shell. The criterion is also a good predictor of ferromagnetic ordering in an intermetallic compounds.

$$ID(E_F) \geq 1 \tag{2.15}$$

This condition is satisfied when the product of the *DOS* at Fermi energy $D(E_F)$ and the exchange interaction (I) is greater than one, to obtain ferromagnetism [94].

In the Stoner criterion, the energy splits the DOS between the spin down and up bands, according to Stoners equation 2.15. This split into bands is known as exchange splitting Δ_{ex} as shown in Figure 2.7. The splitting takes place in the absence of a magnetic applied field and in the presence of spontaneous magnetisation. The Stoner criterion will not be fulfilled if spontaneous magnetisation is not observed [102].

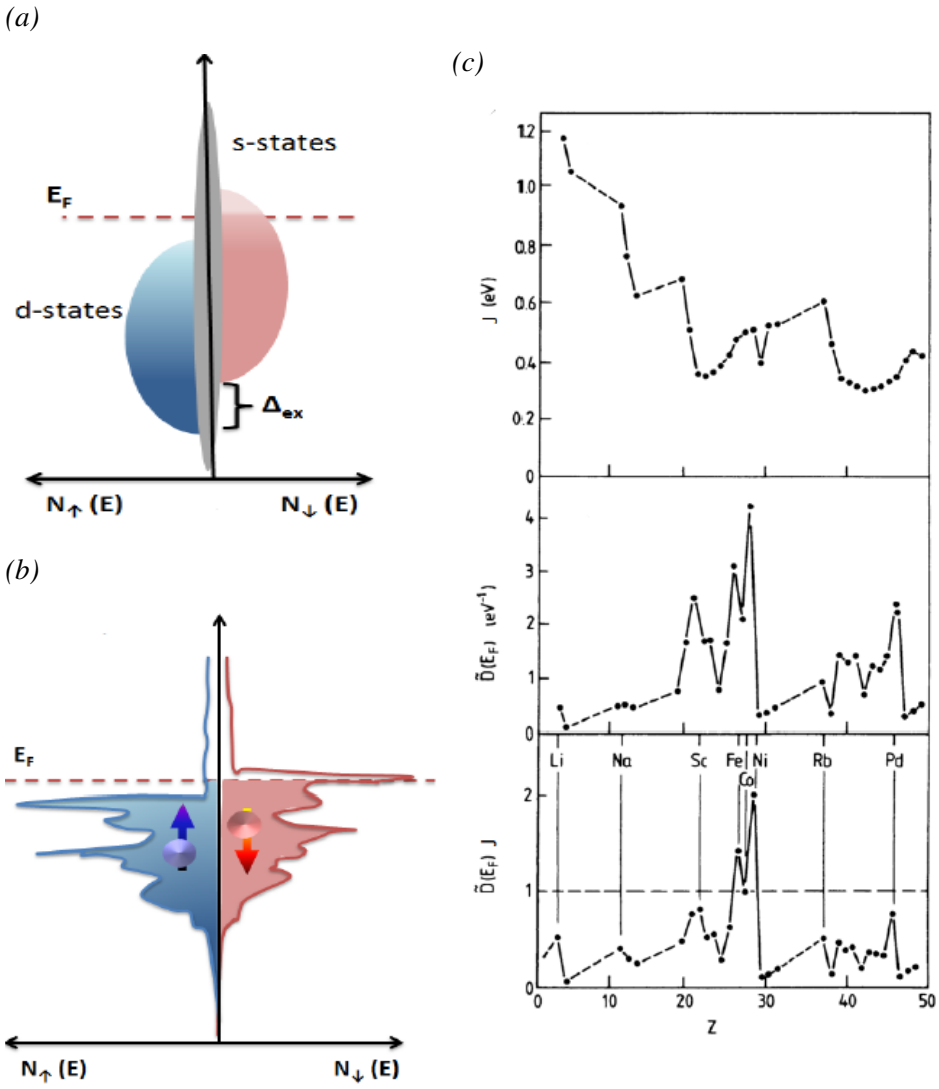

Figure 2.7: (a) The narrow s and the broad d electron bands contribute to the density of states. (b) The spin-dependent density of states in nickel (Ni). Due to the exchange coupling, d states in this case are split, adapted from [102]. (c) The exchange integral J and the density of states at the Fermi energy $D(E_F)$ as a function of the atomic number Z. The bottom graph in (c) shows the product of the exchange integral and the density of states where the elements with values above one show ferromagnetism (Fe, Co and Ni). Two elements are close to reaching the ferromagnetic conditions, i.e. Sc and Pd. Taken from [103].

2.6 Magnetic domain wall

Magnetic materials are subdivided into domains in order to minimise their energy. The magnetic moment is uniform for each domain. When the magnetisation changes from one orientation to a different one at the interface between two magnetic domains this phenomenon is known as a domain wall (DW) [94].

2.6.1 Magnetic domain formation

In thin films, more domains form in the first place due to energy associated with the dipolar field saved by the formation of the magnetic domains. If $\nabla.B=0$ and $B=\mu_0\ (H+M)$, then

$$\nabla \cdot \mathbf{H} = -\nabla \cdot \mathbf{M}. \tag{2.16}$$

where B is the magnetic flux density, H is the magnetic field, M is the magnetic moment per unit volume and μ_0 is the magnetic permeability of free space. At the edges of the thin films, if the magnetisation stops and starts the magnetic field diverges, and this produces a demagnetising field, the corresponding energy is given by

$$E_D = -\frac{\mu_0}{2}\int_V \mathbf{M}\cdot\mathbf{H}_D dV, \tag{2.17}$$

where H_D is the demagnetising field and V is the volume of the thin film. Some thin films demagnetise along one of their principal axes, and so there is a reduction in the energy

$$E_D = \frac{\mu_0}{2} N\mathbf{M}^2 V, \tag{2.18}$$

where N is a demagnetising factor and V is the thin film volume. The formation of the magnetic domains is balanced in to the cost of a domain wall and a demagnetising field.

Figure 2.8 shows three types of magnetic domain structure in ferromagnetic thin films. A large dipolar energy can be observed in a single domain structure, where there is no domain formation as shown in Figure 2.8a. Figure 2.8b shows how the film breaks into

two domains, reducing the dipolar energy. The formation of a closure domain structure (many domain walls) quenches the dipolar energy, as shown in Figure 2.8c [94].

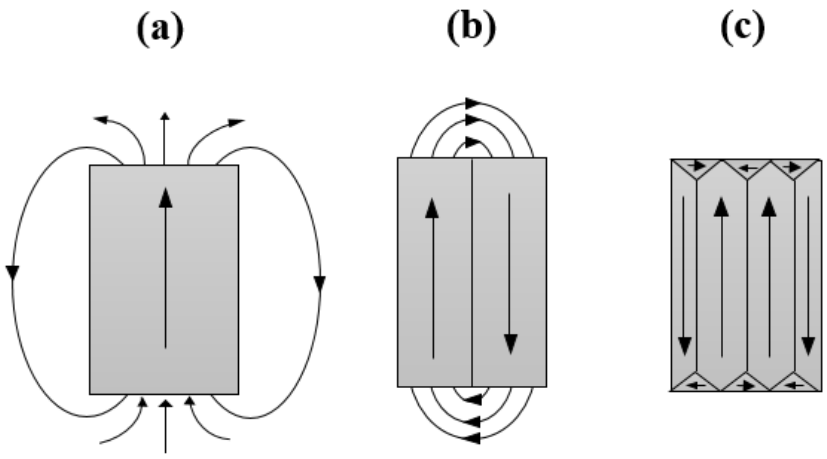

Figure 2.8: Different magnetic domain structures in ferromagnetic thin film. (a) shows a large dipolar energy with no domain wall, and in (b), two domains are produced due to the reduction in dipolar energy. In (c) the closure domain structure quenches dipolar energy and forms a number of domain walls.

2.7 Energy product

The energy product is the most important parameter for permanent magnets, i.e. getting the maximum value of BH obtainable from the hysteresis loop. The energy product illustrates how much field is generated and how close to the magnet. The integral $\int B.HdV$ over all space will be zero for a permanent magnet so it can be split into the integrals outside and inside the magnet, given by

$$\int_{all\,space} B.HdV = \int_{inside\,magnet} B.HdV + \int_{outside\,magnet} B.HdV = 0 \qquad (2.19)$$

where B=$\mu_0 H$ outside the magnet. So the useful energy of the magnet is given by,

$$\int_{outside\,magnet} \mu_0 H^2 dV = -\int_{inside\,magnet} B.HdV \qquad (2.20)$$

The maximum energy product can be described as a measurement of the maximum amount of work that a permanent magnet is capable of outside the magnet. This is measured as half the product of the coercive field and the remanent magnetic flux density which is equal to twice the energy stored in the stray field of the magnet as shown in the following equation

$$(BH)_{max} = \frac{1}{2}(B_r H_c) \tag{2.21}$$

where B_r is the remanent magnetic flux density and H_c is the coercive field. For a high energy product, a large coercivity is required, and remanence such as in a hard magnetic material as shown in Figure 2.9 [104].

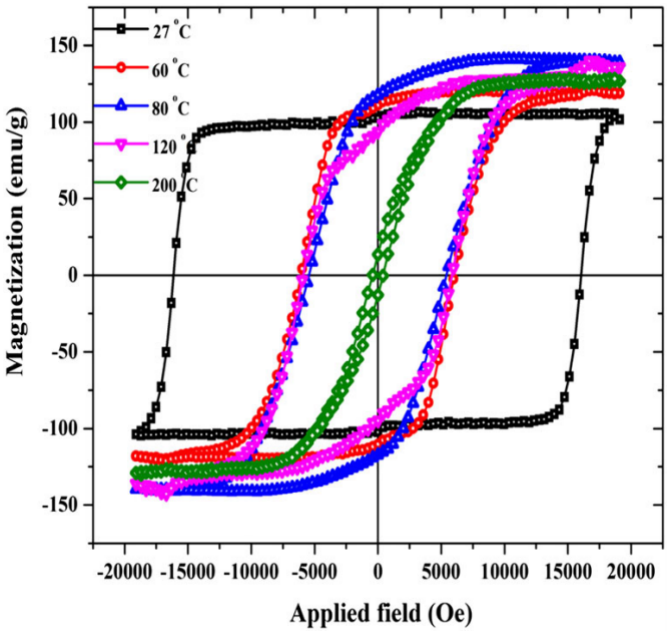

Figure 2.9: Magnetisation curves as a function of applied magnetic field for NdFeB at various temperatures from 27 °C to 200 °C. Taken from [104].

CHAPTER 3

Experimental methods

3.1 Introduction

In this chapter we describe the experimental techniques used to fabricate and characterise the thin film multilayers of Fe/RF-sputtered amorphous carbon (a-C), Fe/C_{60} and Co/C_{60}. The samples were grown using magnetron sputter deposition and thermal sublimation. Several techniques were involved in characterising the structural, magnetic, electrical properties of the samples. To investigate the structure of the samples, X-ray reflectivity (XRR) was used in order to measure the thickness of the films. Raman spectroscopy was also used to monitor carbon graphitization after annealing at 100-750 °C. A superconducting quantum interference device vibrating sample magnetometer (SQUID-VSM) was used to study the magnetic properties with a sensitivity down to 10^{-8} emu. Kerr microscopy was used in order to image the magnetic domain structure. Low temperature electrical transport measurements were used to investigate the anisotropic magnetoresistance in the Co/C_{60} system. The procedures followed in all of the above techniques are discussed in detail in this chapter.

3.2 Sample Fabrication: Sputtering deposition system

Physical vapour deposition was employed in this research to grow high quality metallic and amorphous carbon thin films on a substrate. Figure 3.1 shows the general principle of sputtering, whereby incident particles collide with the surface or near-surface atoms of a target with enough energy to split bonds as well as displace atoms. If one or more atoms are released from the solid during this procedure, they are deemed to be sputtered atoms [105].

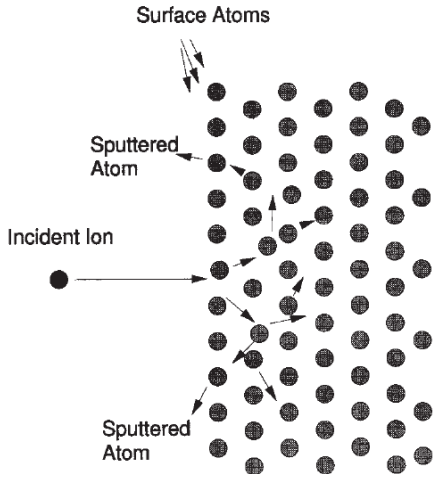

Figure 3.1: Schematic representation of the sputtering principle where a high energy particle collides with the surface of the target material. This leads to eject the target atoms from the surface [105].

During the sputtering process, Ar gas is ionised to form a plasma, which is then electrically accelerated towards a target, leading to the emission of atoms which are then deposited on the substrate. We will use RF and DC magnetron sputtering, and the choice depends on the material to be deposited. RF-sputtering is generally used to grow insulating thin films, in this thesis is RF-sputtered a-C, whereas DC sputtering is used to grow metallic thin films (Ta, Fe, Co, W, Cu, Nb and Al).

In this thesis, our sputtering system comprises of two magnetic guns and six non-magnetic targets as well as an RF magnetron and an evaporation source for the deposition of C_{60} by thermal sublimation. A maximum of 16 different sample holders can be incorporated into the growth, and a shutter within the system allows the deposition of multilayers of different materials. Computer software is used to control the shutter position and the sample wheel. The substrates are cut to a 4 mm $\times$ 4 mm size and cleaned first with acetone, then with isopropanol in an ultrasonic cleaner and dried using nitrogen gas/compressed air before sputtering. Cleaning the substrates improves adherence to the substrate surface. All the targets are pre-sputtered for 10 minutes before growing by energetic Ar^+ ions bombardment to clean and remove contaminant surface layer [106]. In the DC sputtering system involved in this thesis, a pair of electrodes (cathode and anode). The cathode was based at a DC voltage around 400 V and

the target material placed on the front surface. The cover of the target (the target can) functioned as the anode, which is usually grounded with a base pressure of 10^{-8} Torr.

In this thesis, RF sputtering was used to grow 0.5-40 nm thick amorphous carbon thin films. The XRR data for sputtered amorphous carbon are fitted using the software Bede to get further information about the roughness. The X-ray reflectivity (XRR) curve with its fitting is shown about 0.55 nm roughness. Creating a plasma using DC constitutes the most basic technique; however, this requires two conductive electrodes through which the DC current is passed. Since the amorphous carbon layers are electrically insulating, the most common technique is to apply a coupled RF plasma [65, 107] and in the majority of cases the usual radio frequency supplied to the electrode is 13.56 MHz [64, 108]. Using this method, it is possible to deposit insulator films via RF magnetron sputtering at rates considerably higher than those obtainable via DC techniques [109].

To go from room pressure to 20-30 m Torr, the sputter chamber is pumped first with a roughing pump. High vacuum conditions are then created by using a cryo-pump with a base pressure in the main chamber of about 10^{-7} Torr after 12 hours. Water vapour is drawn out using a Meissner trap by forming a low surface temperature of 77 K on the tubing placed on the top of the chamber walls in which liquid nitrogen flows, further reducing the pressure within the chamber to 10^{-8} Torr. The composition of the pressure and gas/water content in the chamber can be determined using a residual gas analyser (RGA) [91].

Figure 3.2 shows a diagram of the DC sputtering tool used in this thesis. For magnetron sputtering, permanent magnets are placed beneath the target surface in order to confine the plasma by the Lorentz force. The magnetic field forms a closed loop path which traps the electrons around the surface of the target. The ejected electrons due to the magnetic field move in cycloid orbitals immediately above the target. Increasing the orbital motion of the electrons strongly increases the probability of ionisation of the argon gas, which effectively increases the sputtering rate [70, 107, 110].

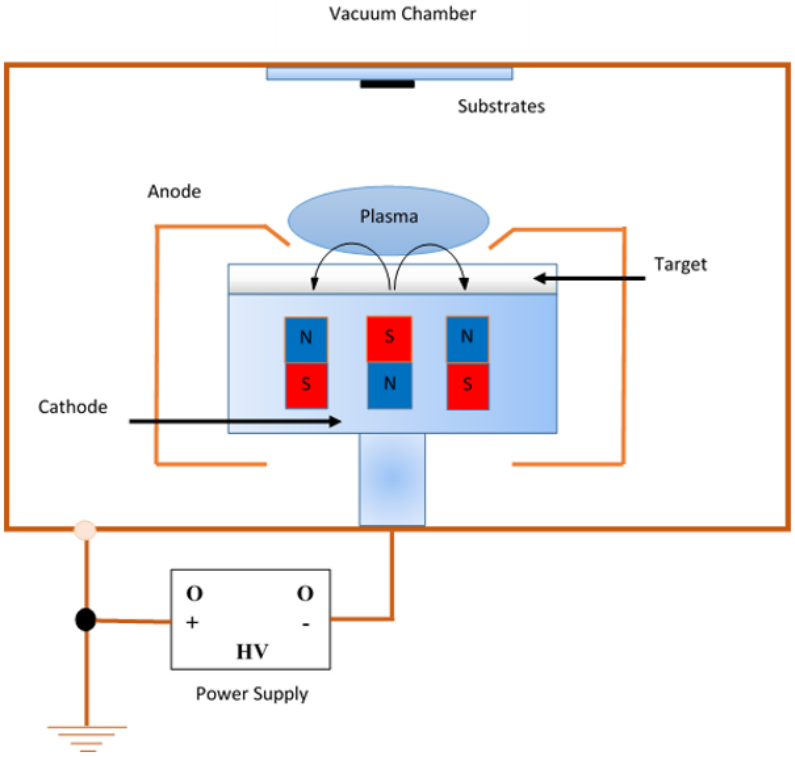

Figure 3.2: Diagram of a DC magnetron sputtering system. A DC voltage is applied across the anode (the target can) and cathode (target), after introducing the sputtering gas (argon) into the evacuated chamber. The argon atoms are ionised owing to the accelerated electrons between the cathode and anode, resulting in a plasma. The ionised ions bombard the target at speed, ejecting metal ions from its surface which are then deposited on the substrate in a thin layer. To enhance the ionisation rate and trap electrons, magnets are placed underneath the target.

Figure 3.3 shows a diagram of the RF-sputtering used in this study. The oscillating radio frequency (RF) voltage applied between the electrodes is typically around 13.56 MHz. The introduction of argon into the chamber and the ionisation due to the applied voltage causes a beam of high energy positive argon ions to be accelerated towards the target. The argon ions bombard the atoms of the target and cause the ejection of metal ions from the target surface due to the transfer of momentum from the argon ions and subsequent atom collisions [111]. The metal ions are then deposited on the substrate [110].

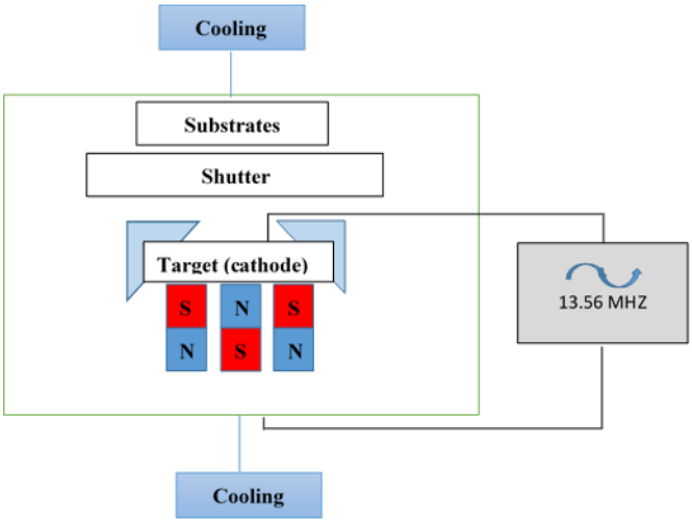

Figure 3.3: Diagrams show RF magnetron sputtering, here the cover of the target and target holder are the anode and the cathode respectively.

The first main goal of this thesis is the optimisation of the growth conditions for amorphous carbon (a-C) thin films by using RF sputtering. This was a new material of study for the Condensed Matter group at the University of Leeds. The growth parameters such as power and time were varied then the structure of deposited/sputtered carbon were later annealed at a range of temperatures. Figure 3.4 shows the power range used versus the deposition rate and total film thickness estimated by XRR.

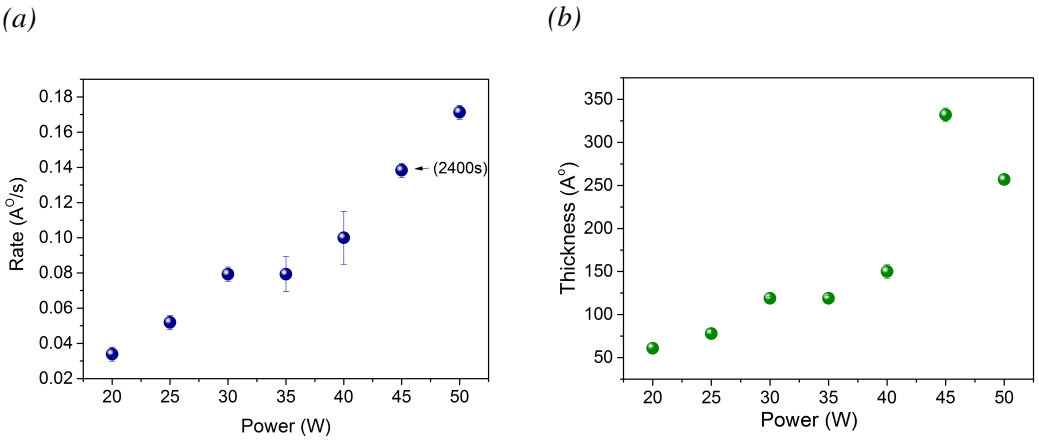

Figure 3.4: (a) The deposition rate (b) the thickness of the RF sputtered carbon as a function of growth power. The films are deposited for 1500 s, whereas one sample (45 W) is grown for 2400 s. The samples were grown via sputtering where the base pressure was 2×10^{-8} Torr in the main chamber and argon flow rate was 24 SCCM (standard cubic centimetres per minute).

Throughout this study, C_{60} molecules were deposited via thermal sublimation in the same sputtering chamber without breaking vacuum. C_{60} in powder form is placed in a crucible and heated by a tungsten filament. The tungsten filament is attached to two copper electrodes. A high current of approximately 20 A is applied to the copper rods. Before growing the C_{60} thin films, the molecule source was pre-heated to actual deposition temperature in order to remove the solvent impurities and the fullerene oxides, and produce pure fullerene thin films [112].

To prevent the evaporation source from overheating, it is encased by a water-cooled system. A quartz crystal monitor is used to determine the thickness of the deposited thin films, usually 10-20 nm. The crystal oscillates at a resonant frequency in the MHz range. The resonant frequency varies as the mass of the deposited material changes. This leads to a change in frequency which is used to determine the thickness and the growth rate. In order to have a reliable film thickness the tooling factor can be calibrated by measuring the Kiessig fringes via XRR after each growth. A schematic diagram of the thermal sublimation source used in this project is shown in Figure 3.5.

Obtaining uniform C_{60} layers is very important for this work. The magnetic properties can be affected by the thicknesses and roughness of the C_{60} layer. This parameter can be altered by varying the growth rate of C_{60}. Higher rates result in smoother films, but with bigger variations in thickness from calibration. An optimal rate of 0.7-1 Å/s is found for filament currents of 20-21 A.

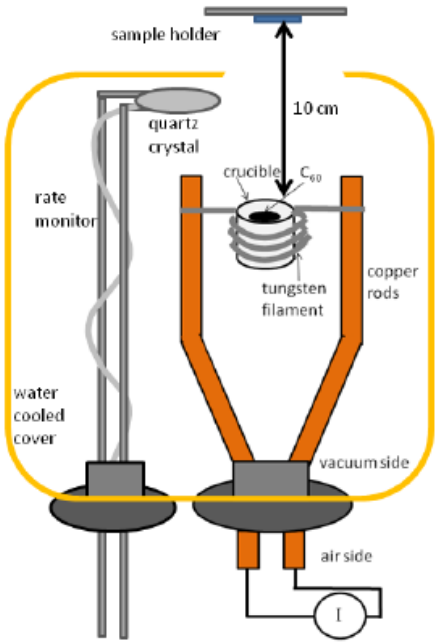

Figure 3.5: Diagram of the fullerene C_{60} source. The C_{60} (powder) is placed in an aluminium crucible attached to a copper rod. The crucible is heated by applying a current of about 20 A through a tungsten filament. The current heats the tungsten filament to several hundred Kelvin. Taken from [70].

3.3 Sample annealing process

In this thesis, the as deposited carbon thin films are amorphous. After measurement, they were subsequently annealed to obtain a nano-crystalline structure and the post annealing changes were investigated. The samples were placed in a tube furnace to be annealed at different temperatures (100-750 °C) for different time intervals from one

hour to ten hours at a pressure of 10^{-5} Torr. The tube furnace heats up to a specific temperature and then cools down to room temperature at a consistent rate of 5 °C per minute to avoid strain on the films.

3.4 Structural characterisation

3.4.1 X-ray reflectivity

X-ray diffraction (XRD) and X-ray reflectivity (XRR) make use of the coherent interference of scattered Xrays to obtain information about the structure of materials [70, 113].
The parameters that can be determined in XRR are the thickness, roughness and/or inter-diffusion between layers. X-rays are high-energy electromagnetic radiation with short wavelength (in our case Cu- Kα with λ= 1.54 Å). They are produced when high-speed electrons collide with a metal target inside a vacuum tube. The usual technique to generate X-rays in a laboratory utilises a vacuum tube containing a tungsten cathode filament. An AC voltage is used to heat the filament, which generates electrons via thermionic emission. Electrons are accelerated under high potentials that range from 5 to 80 kV directed towards a metal target (anode) to excite the electrons in the target to higher energy levels. These electrons then relax into their ground state and X-ray photons are emitted. The incident X-ray go to the sample, which is rotated together with the detector in order to measure the X-ray counts [114]. The incident X-ray onto a crystalline material then scatters waves from the parallel planes of the atoms in the crystal. Then interference happens, which can be constructive or destructive. To determine the thickness of a thin film, the constructive peaks are mapped by a diffraction curve. The X-ray photons can be collimated when directed through filters and slits. From the angular positions of the constructive peaks on the diffraction curve we can obtain the thickness (t) of a thin film.

The incidence X-rays on the thin film at angle ω is reflected and detected by a moveable detector at angle θ as shown in Figure 3.6. The incident beam angle ω and the detector angle θ are equal in order to measure at the specular condition, where the

coherent scattering of X-rays can be investigated. The intensities of the reflected wave were observed as a function of the angle 2θ as shown in Figure 3.6. Reflection from the film/substrate interface can occur when the critical angle θ_c is exceeded. Oscillations can be observed when multiple interference of X-rays reflect off the surface of the film and the interface between the film and substrate. These oscillations are known as Kiessig fringes and can be used to derive the thickness (t) of a thin film by analysing the reflectivity intensity curves [70, 115].

$$\lambda = 2t\sqrt{\sin^2\theta_n - \sin^2\theta_c}, \tag{3.1}$$

Where n is an integer, λ is the wavelength, θ_c the critical angle, and θ_n is the position of the constructive peaks [115–117].

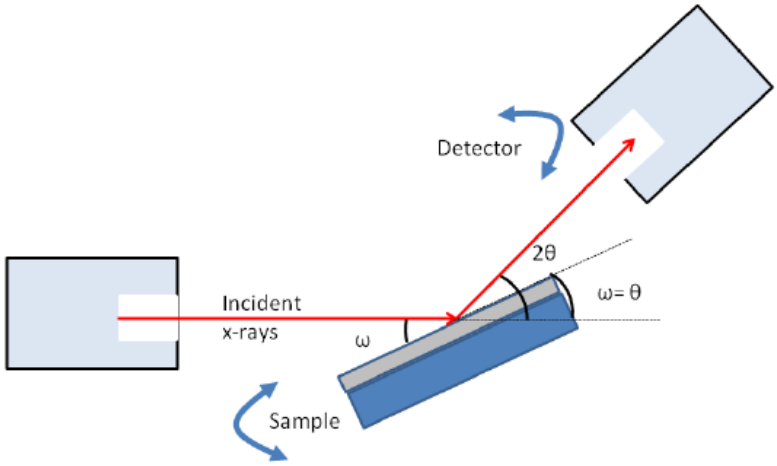

Figure 3.6: Schematic representation of X-ray reflectivity (XRR). The X-rays were incident on the sample at angle ω and X-rays reflected to a movable detector from the sample at angle θ. The measurements have been taken in specular conditions, where ω=θ and there is coherent scattering of X-rays. Taken from [70].

Figure 3.7a presents a typical example of scattering from a single thin film sample. The roughness of an amorphous carbon sample sputtered at 30 W for 25 minutes is 5.5±0.1 Å as determined by a Bede fitting as shown in Figure 3.7b. This roughness

is in agreement with literature values [56]. In this work, the thickness of the metallic film strongly affects the magnetic properties. Therefore, it is important to keep consistency between the different samples and growths, in particular when depositing very thin metallic layer for instance below 0.5 nm. A few seconds or small fluctuation in pressure, power to get difference thickness will lead to significant differences in thickness of a few nanometres. Calibration samples with superlattice structures were grown by depositing one material on top of a different material in a repetitive sequence in order to obtain a right value of thickness for thinnest metallic layer thin films. The thickness and the time of a superlattice can be determined from the angular position of the peaks using equation 3.1 [118]. The data for a superlattice structure obtained from X-ray reflectivity was fitted by Bede software [119], where parameters such as thickness, roughness and densities for each individual layer can be extracted from the fit.

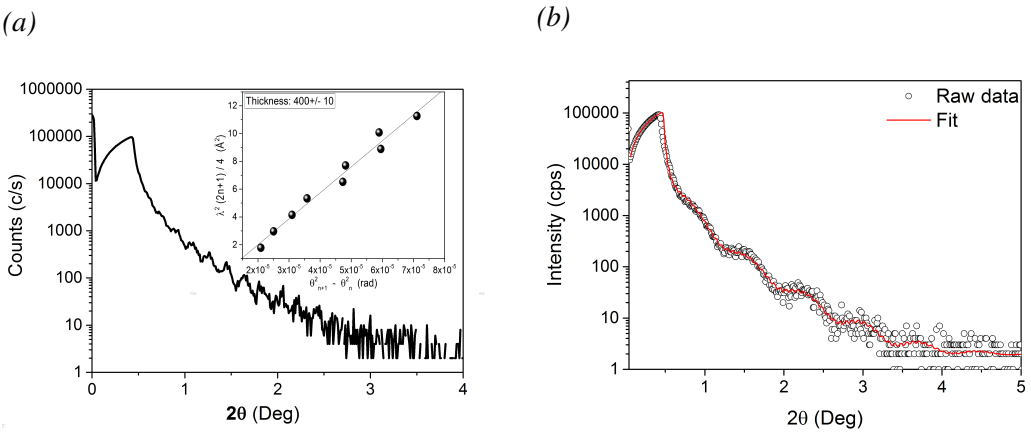

Figure 3.7: X-ray reflectivity measurements of (a) a single layer of RF-sputtered amorphous carbon (400±10 Å) and the thickness of was obtained using the Kiessig equation. Inset, the Bragg peaks for fitting the data in (a) and the matching sample thickness. (b) Data taken from Bede report showing a 5.5±0.1 Å roughness in a RF-sputtered a-C film 120±2 Å thick. Open circles show the raw data and the solid red line shows fitting the data.

3.5 Raman spectroscopy

Raman spectroscopy is a technique used to study the structure of the materials based on the inelastic scattering of monochromatic light. The technique is named after Sir Chandrasekhara Venkata Raman, who developed it in 1928 [120].
Characteristically, a monochromatic source when incident on a sample causes photons to scatter. The majority of these photons are scattered elastically, a phenomenon known as Rayleigh scattering. However, about one in 10^6 - 10^7 of the photons are scattered inelastically, with a resulting shift in the frequency of the photons, which is termed the Raman effect. The three types of elastic and inelastic scattering of photons are shown in Figure 3.8; these are (elastic) Rayleigh, (inelastic) Stokes and anti-Stokes scattering. In Stokes scattering photons lose energy by exciting the material to a higher energy vibrational state whereas anti-Stokes scattering photons gain energy from vibrating atoms. Frequency changes depend on the modes or transitions, for instance the rotational or vibrational modes of the sample. Induction of a dipole moment P takes place when an electric field $\bar{E}$ is incident to a given sample. The polarisability α depends on the molecular structure as well as the bonds of the material [121]. The equation can be written as:

$$P = \alpha \bar{E} \tag{3.2}$$

The frequency of an incident electromagnet wave is ν_0 gainst the electric field $\bar{E}$. The electric field $\bar{E}$ is time dependent, and defined as

$$\bar{E} = \bar{E}_0 \cos(2\pi\nu_0 t) \tag{3.3}$$

Where, The electric field $\bar{E}$ is time dependent (t) and $\bar{E}_0$ is the energy of the ground state.Therefore, the induced vibration of the dipolar moment can be described as,

$$P = \alpha \bar{E}_0 \cos(2\pi\nu_0 t) \tag{3.4}$$

For any given molecular bond, there are vibrational modes allowed to which the atoms are locked. The vibrational modes are quantised with the energy of a specific vibrational mode $\bar{E}_{vib}$ written as,

$$\bar{E}_{vib} = (j + 1/2)h\nu_{vib} \tag{3.5}$$

where j represents the vibrational quantum number and ν_{vib} represents the frequency of a vibrational mode. This polarisability is associated with the immediate position of atoms since the electrons perturbation by an electric field is dependent on the comparative location of atoms within the molecular structure. Thus, the physical dislocation from equilibrium because of a vibrational mode dQ can be linked to the maximum dislocation Q_0 by

$$dQ = Q_0 \cos(2\pi\nu_{vib}t) \tag{3.6}$$

The polarisability for small dislocations can be described using a Taylor series,

$$\alpha = \alpha_0 + \frac{\partial\alpha}{\partial Q}dQ \tag{3.7}$$

Combining the previous equations helps in relating the polarisability to the physical dislocation,

$$\alpha = \alpha_0 + \frac{\partial\alpha}{\partial Q}Q_0 \cos(2\pi\nu_{vib}t) \tag{3.8}$$

$$P = \alpha_0\bar{E}_0 \cos(2\pi\nu_0 t) + \frac{\partial\alpha}{\partial Q}Q_0\bar{E}_0 \cos(2\pi\nu_0 t)\cos(2\pi\nu_{vib}t) \tag{3.9}$$

The strength of the dipole moment P can be separated into three terms which explain Rayleigh, Stokes and anti-Stokes scattering as indicated in equation 3.10, by the first, second and third terms respectively [70, 121].

$$P = \alpha_0\bar{E}_0 \cos(2\pi\nu_0 t) + \left(\frac{\partial\alpha}{\partial Q}\frac{Q_0\bar{E}_0}{2}\right)\{\cos(2\pi(\nu_0 - \nu_{vib})t) + \cos(2\pi(\nu_0 + \nu_{vib})t)\} \tag{3.10}$$

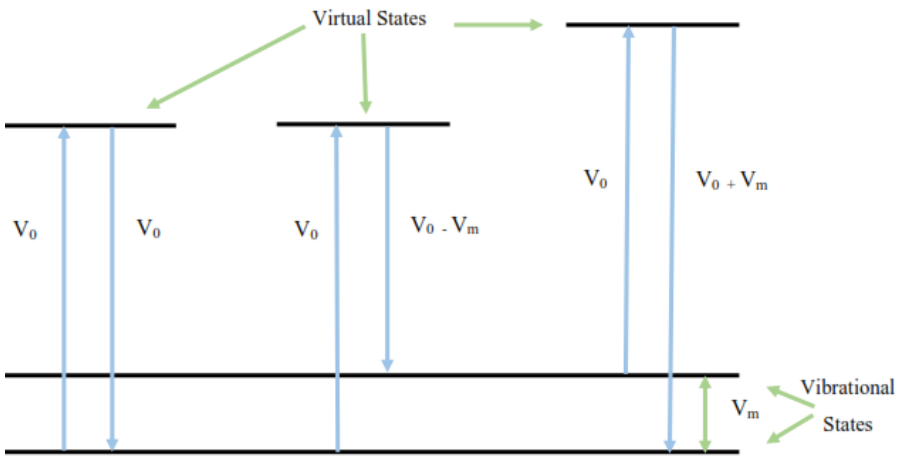

Figure 3.8: Diagram showing the transitions of photons in Raman spectroscopy. Whenever the frequency of a scattered photon is similar to the incident photon, the phenomenon is referred to as Rayleigh scattering. The Raman effect generally occurs when the frequency of the scattered photons shift from the incident frequency. This is known as Stokes when the frequencies shift up and anti-Stokes when the frequencies shift down.

The Raman spectrometer [122] used in this thesis is the Horiba-Jobin-Yvon LabRam HR800 system illustrated in Figure 3.9. First a laser emits monochromatic light which is reflected off a mirror via a number of filters. Then, the light travels through a line filter which constricts the Gaussian circulation of the photons around the required wavelength. The filtered light passes via an emission intensity filter to manage the intensity of light incident on a sample. The light that is filtered is then reflected by two two-way mirrors of a microscope and is finally reflected off a sample positioned underneath the microscope. The objective lenses of the microscope have magnifications of 10, 50 and 100. Focusing the microscope on the sample is done using a white light source together with a video captured by an USB camera. The light that is scattered off the sample travels via the microscope, reflecting off the first two-way mirror and then the second two-way mirror. The elastically scattered light is removed by a long wave pass filter letting through the inelastically scattered light to diffract off the diffraction grating. The diffracted light is detected by a charge coupled device (CCD) that measures the spectra of the light intensity at differ wave numbers. Rotation of the diffraction grating ensures measurement of a wide range of wavelengths. The size of the diffrac-

tion grating can be altered between 600 ln/mm and 1800 ln/ mm to vary the spectra resolution; however, a resolution enhancement leads to a narrower and less intense thinner spectrum band being incident on the CCD at any one given time. Three lasers can be utilised: a blue 473 nm diode, a green 532 nm Nd:YAG, and a red 633 nm HeNe pumped solid state laser [70]. Blue and green laser were used to characterise the samples in this research.

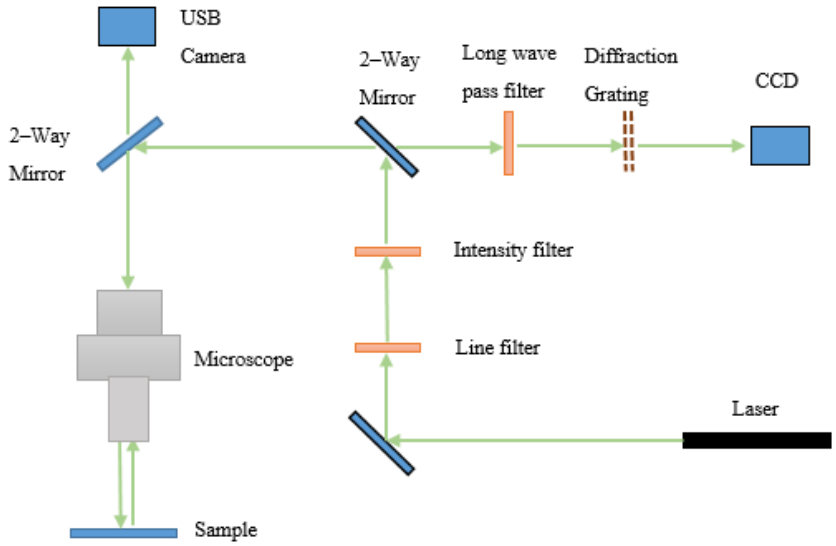

Figure 3.9: Schematic of the Raman spectrometer shows the operating process of an emitting laser. The diagram exhibits a Lab RAM HR800 with a laser excitation wavelength of 532 nm used in this research. A 1800 ln/mm grating was used to obtain a better resolution.

Robertson and Ferrari have provided a wide-ranging evaluation of the Raman spectra of carbon allotropes by a broad range of amorphous and disordered carbon allotropes [123]. Carbon has two main vibrational modes which provide characterisation of bond disorder and can be distinguished easily in the Raman spectra. The first vibration is the stretching mode (called the D peak) and the second one is the breathing mode (called the G peak). The D and G peaks are located at approximately 1360 and 1600 cm^{-1}, respectively, for visible excitation [123]. Because of the stretching movement, the G peak (Figure 3.10a) of all sp^2 atoms appears in both chains and rings.

The D peak occurs due to the breathing mode (Figure 3.10b) of sp^2 atoms in rings [123][124]. The Raman spectrum relies on bond disorder. The clustering of the sp^2 stage, the sp^2/sp^3 ratio and the presence of sp^2 chains or rings gives different shapes to the Raman spectra, as Figure 3.11 schematically indicates [124].

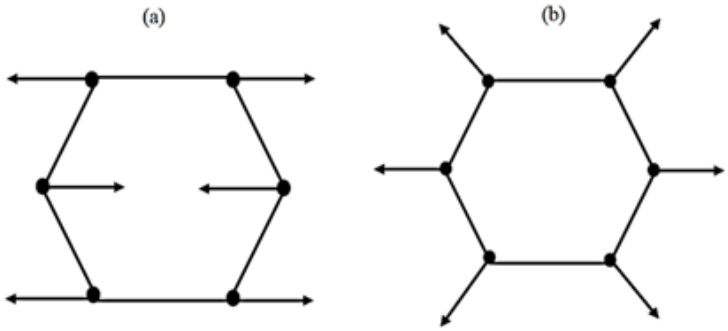

Figure 3.10: Schematic of carbon vibration modes. In (a) the G peak occurs due to the stretching motion of sp^2 and in (b) the D peak occurs because of the breathing modes of sp^2.

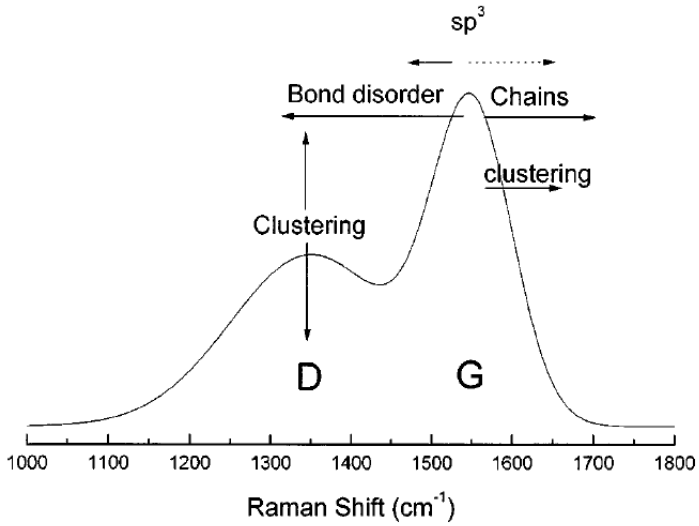

Figure 3.11: Schematic diagram of the D and G peaks on the Raman spectra. The dotted arrow marking the indirect influence of the sp^3 content on increasing G position intensity comparing to the D peak which indicates clustering of the sp^2. Taken from [124].

The behaviour of the Raman spectra in all forms of amorphous carbon can be classified by the three-stage model in Figure 3.12. The first stage is graphite to nanocrystalline graphite (NC-G) (0% sp^3). The G peak moves from 1581 to ~1600 cm^{-1} in the first stage and there is an increase of I(D)/I(G). The second stage is nanocrystalline graphite to a-C (~ 20% sp^3), the G peak decreases from 1600 to ~ 1510 cm^{-1} and the ratio of I(D)/I(G) is 0.1. The third stage a-C to ta-C (~ 100% sp^3) characterised by an increase in the G peak from ~ 1510 to 1570 cm^{-1} (or ~ 1630 cm^{-1} for sp^2 dimmers in ion implanted diamond). The ratio of I(D)/I(G) is very low or 0 [122, 124].

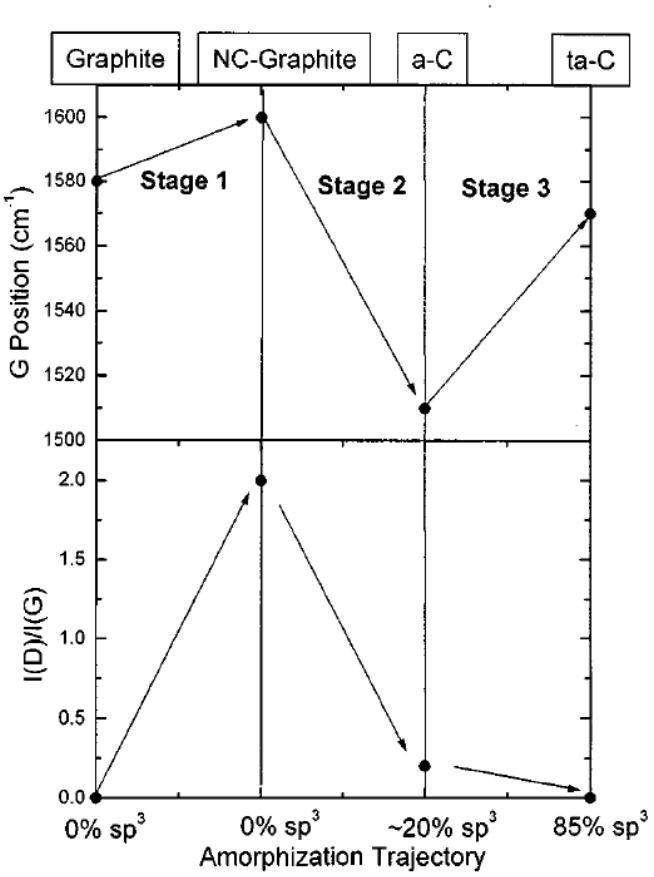

Figure 3.12: The amorphisation trajectory diagram characterised by the G position and I(D):I(G) ratio. Taken from [124].

Raman scattering spectroscopy [121] was used to analyse the films grown and the properties of the RF-sputtered amorphous carbon thin films grown on silicon oxide before and after annealing. Figure 3.13a shows the Raman spectra taken on an amorphous carbon sample before annealing with 119±2 Å thickness and grown on a Si/SiO_2 substrate using 35 W of power and sputtered for 25 minutes. The figure shows two silicon peaks at 520 cm^{-1} and 950 cm^{-1}. There are two primary carbon features shown by the spectra, the D peak and the G peak, which have frequencies of around 1360 and 1600 cm^{-1} respectively for visible excitation [123]. Figure 3.13b shows the Raman spectra taken on an amorphous carbon sample before annealing and after annealing at 400 °C grown on a Si/SiO_2 substrate using 50 W of power and sputtered for 25 minutes. Raman spectra indicate a shift in the G peak to high frequency as carbon annealed to 400 °C.

(a) *(b)*

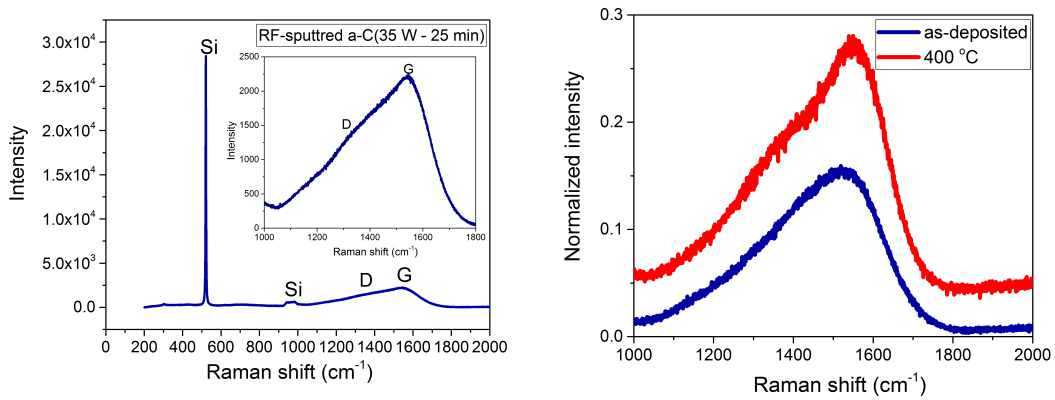

Figure 3.13: Raman spectrum of the amorphous carbon thin film showing (a) silicon peaks and G and D bands for as deposited RF-sputtered a-C film where D and G peaks around 1345-1355 cm^{-1} and 1570-1590 cm^{-1}, respectively [125, 126] (b) sample before (blue curve) and after annealing (red curve) at 400 °C grown on a Si/SiO_2 substrate using 50 W of power and sputtered for 25 minutes, the spectrums indicates shifting in the G peak after annealing at 400 °C.

Figure 3.14 shows the Raman peaks position and ratio for varying deposition powers. An increase in power up to 50 W lead to decrease in G position from 1570 to 1548 cm^{-1}, which means that the carbon thin films shifts from nanocrystalline (NC) graphite to amorphous carbon (a-C) as shown in Figure 3.14a. There are variations of the D and G peak intensities (I(D)/I(G)) between 0.3 and 0.5 with increasing power W, as shown in Figure 3.14b. This ratio range for the samples lies between amorphous carbon and nanocrystalline (NC). Most of the samples are closer to a-C ratio, so I(D)/I(G) is between 0.3 and 0.5. This range is in line with that of earlier studies, which found that the a-C ratio between I(D) and I(G) tends to be near zero [124]. Amorphous carbon has a 20% sp^3 content whereas NC-graphite has a zero sp^3 that consists of a clustering of the sp^2 bonds.

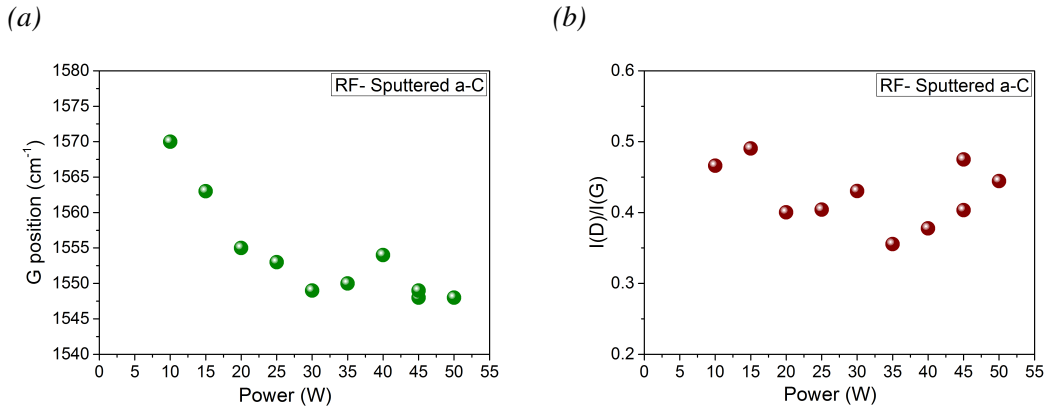

Figure 3.14: (a) G position obtained from Raman measurement as a function of growth power (b) The relationship between growth powers (W) and the ratio of I(D)/I(G). From G peak and the ratio I(D)/I(G) the data indicate movement from nanocrystalline graphite to amorphous carbon according to Figure 3.12. All the data here are taken before annealing.

A sample grown at 50 W was annealed in order to study the impact of annealing on the carbon structure. The annealing experiment was done in a tube furnace with a vacuum of 10^{-5} Torr, with annealing the sample at 200 °C, 300 °C and 400 °C. After every period, the sample was permitted to cool fully for 40 minutes before opening to air to avoid oxidation.

Figures 3.15a and 3.15b illustrate the relationship between growth power (W) and G position (cm^{-1}) as well as the relationship between the ratio I(D)/I(G) and power as

functions of annealing. The transformation from amorphous carbon to nanocrystalline graphite upon annealing is confirmed changes in from the G position (cm^{-1}), which increases from 1549 cm^{-1} to 1566 cm^{-1}. The noncrystalline carbon obtained when the film is annealed at 400 °C. Furthermore, there is a gradual increase in the ratio of I(D) and I(G) from 0.4 to 0.6, which is consistent with the findings of Ferrari and Robertson as discussed in this chapter [124]. Along with the other Raman results shown in Figure 3.15, it is clear that the carbon target produced by RF sputtering in our system is amorphous, which is the objective of this experimental work. Furthermore, the condition of the growth can be play an important key role in modulating the properties [127–129] of carbon thin films.

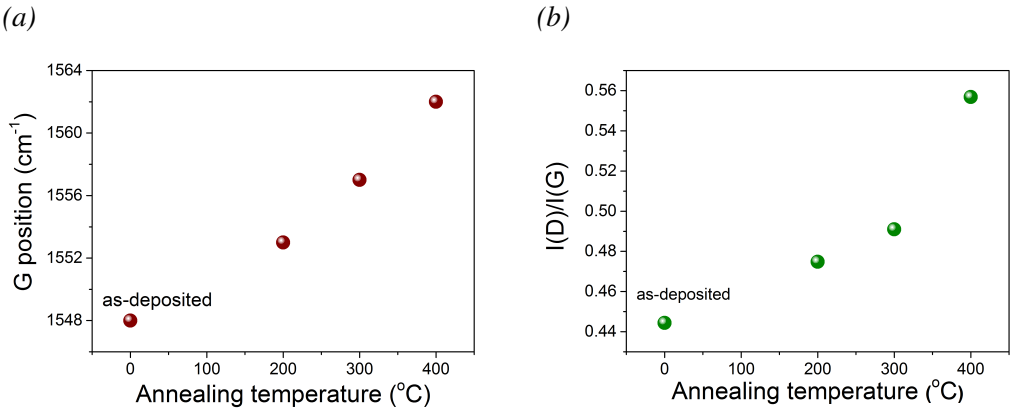

Figure 3.15: Raman measurements of sample grown of 50 W and annealed at different temperatures (a) shows the G position (cm^{-1}) and (b) the ratio I(D)/I(G) of sample annealed at different temperatures. The data indicate movement from amorphous carbon (20% of sp^3) to nanocrystalline graphite (0% of sp^3) after annealing [130] as according to Figure 3.12.

3.6 Magnetic characterisation

3.6.1 Superconducting Quantum Interference Device (SQUID) Magnetometer

In this research, a superconducting quantum interference device (SQUID) was used to study the magnetic properties of the thin films. The Quantum Design SQUID -VSM system is a very sensitive magnetometer which can measure very small magnetic moments of about 10^{-8} emu. The default vibration frequency is 14 Hz with 5 mm amplitude. The samples studied have a magnetic moment in the 10-100 μ-emu range. The SQUID magnetometer can measure the magnetic properties over a wide range of magnetic fields (up to 7 T) and temperatures (1.8 K to 1000 K).

The superconducting quantum interference device consists of two Josephson junctions, which, along with a superconducting loop, are inductively coupled to superconducting detection coils that are able to perform very sensitive magnetic measurements. The detection coils are formed as a second order gradiometer to reduce signals from external field. The second order gradiometer consists of a central coil with two symmetrical end coils connected in series and in opposition to the central coil as shown in Figure 3.16. All coils are located in the uniform field region of the superconducting coil. The SQUID-VSM measurement is performed by a vibrating magnetised sample which is mounted on a non-magnetic quartz rod placed within the superconducting detection coils. This produces a time-varying change in magnetic flux in the detection coils caused by vibrating the magnetised sample through the coils. The two Josephson junctions in parallel in a superconducting loop [131] and if there is no applied magnetic field, the input current splits equally through the Josephson junctions. When a small external magnetic field flows, a screening current I_s starts to circulate in the superconducting loop and generates a magnetic field which is equal and opposite to the applied magnetic field, that cancels the applied net flux. Increasing the screening current together with the magnetic flux leads the Josephson junction becomes resistive when the magnetic flux reaches half a quantum. The sign of the screening current changes and goes to zero at one flux quantum $\emptyset_o$. The vibration of the current in the detection coils leads to a change in the magnetic flux that produces an output voltage

V which is proportional to the magnetic moment of the sample. The SQUID feedback circuit is used as a null detector, so it cancels the current in the detection coils except the induced current owing to a change in flux in them [132, 133]. By using SQUID-VSM, hysteresis loops can be measured for different magnetic materials by measuring the magnetic moment at various field values. A magnetic moment against temperature can also be obtained.

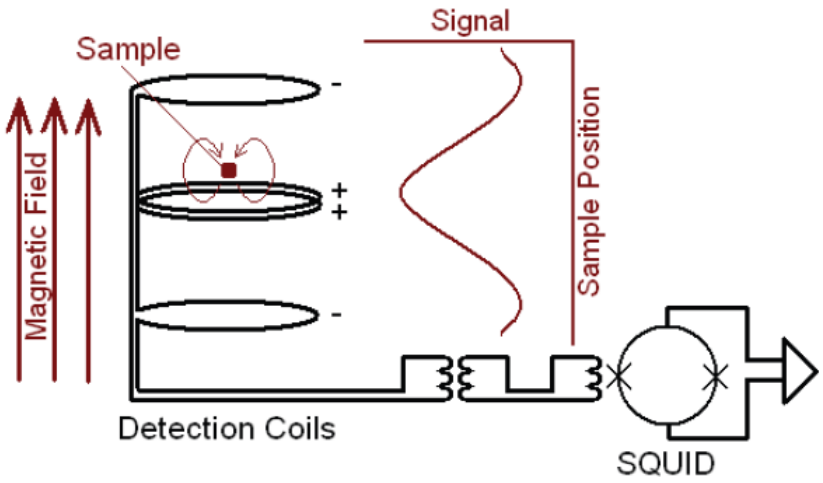

Figure 3.16: Schematic of a magnetometer (SQUID-VSM) detection system. SQUID-VSM contains superconducting detection coils attached to an input coil of inductance which is coupled in turn to the DC SQUID [91, 134].

3.6.2 Wide - field Kerr microscopy

In order to image the magnetic domain structure in a magnetic sample, we used Kerr microscopy. The Kerr effect was first observed in 1877 [135]. It is an effect exhibited by light when reflected off the surface of metallic thin films, causing a rotation of the polarisation (Kerr rotation). Measuring the Kerr effect depends on the measurement orientation. There are three possible forms (Figure 3.17) in which the Kerr effect can be measured; polar Kerr effect when the magnetisation of the sample is perpendicular to the surface, the transverse Kerr effect occurs when the magnetisation is parallel to the surface of the sample, the longitudinal Kerr effect occurs when the magnetisation

is in-plane. Kerr microscopy produces an images down to one micrometre resolution depending on the lens used. A white light emitting diode source is used. By using a camera, the reflected light from the thin film can be detected. The detected images show changes in the intensity of the light that is proportional to the local magnetisation of the thin film. By measuring the contrast across the surface of the films an image on the different contrasts/domains can be created by computer software [96].

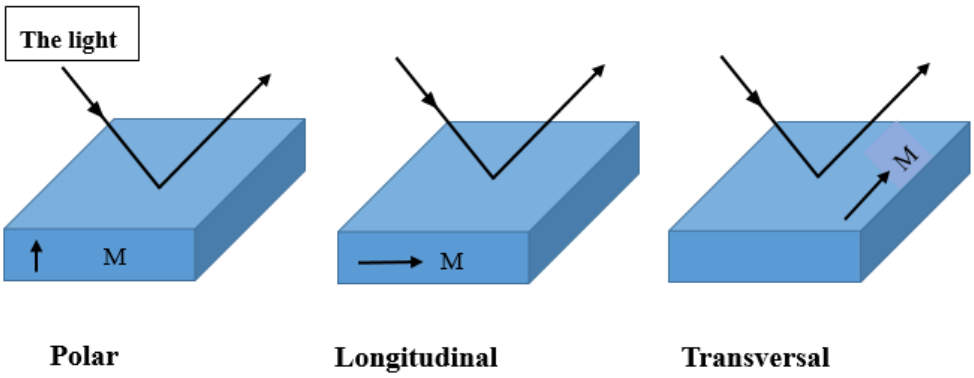

Figure 3.17: Illustration of the three possible configurations using Kerr microscopy. M is the magnetisation of the samples as indicated by the arrows.

3.7 Low temperature transport measurement

Electron transport measurement in this work is carried out in a helium (He) flow cryostat [136, 137] with a temperature range between 1.5 and 300 K. To perform electron transport measurements as shown in Figure 3.18, the samples are mounted onto a specially designed head (sample holder) which attaches to the end of a stick and is placed in the cryostat. The sample is surrounded by split pair superconducting coils that can produce a magnetic field of up to 3T. The cryostat consist of three parts. A variable temperature insert (VTI) is placed in liquid helium which allows the samples temperature to be adjusted with the flow of He gas. The temperature is controlled by a heater which is set at the bottom of the VTI, and the He gas flows via a needle valve. The needle valve (NV) is sited in the helium bath. The VTI is surrounded by a helium

jacket in order to obtain measurements at a specific temperature and to provide the gas flow. A nitrogen jacket around the He bath gives more insulation to the system [138]. To reduce the boil-off, a vacuum jacket is used around the cryostat.

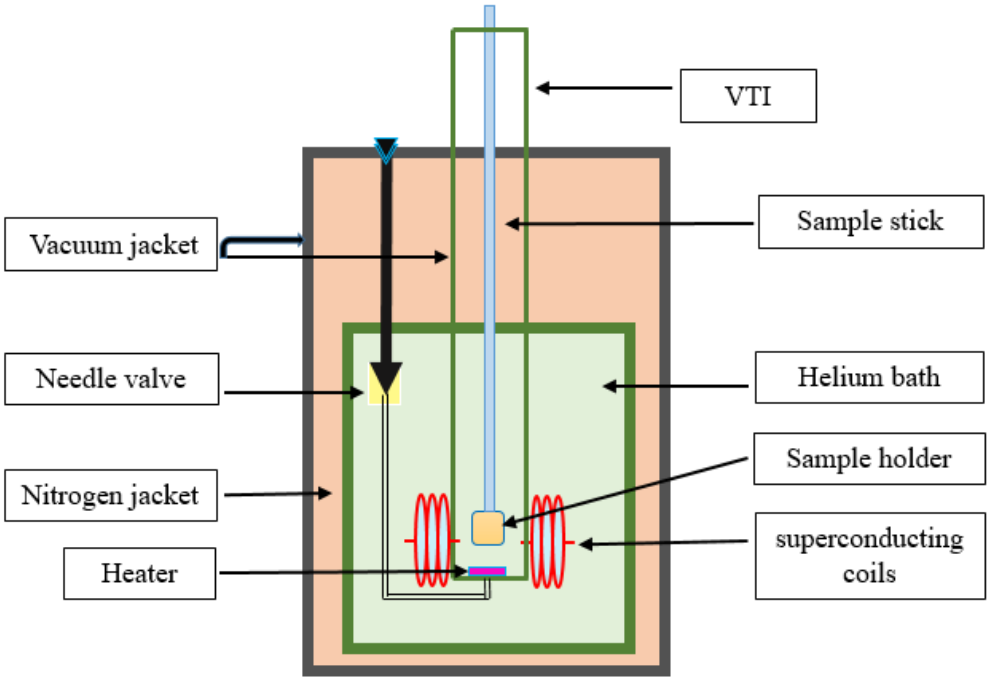

Figure 3.18: Schematic diagram of the helium cryostat apparatus. The cryostat operates in liquid He with a magnet that generates a field up to 3T.

The studied sample is the bilayer Co/C_{60} film of structure of Ta(4 nm)/Co(3 nm)/C_{60} (35 nm)/Al(10 nm). This film was grown on 4×4 mm^2 silicon oxide substrate where the electrical contacts (four point contacts) were formed using wire bonding. Keithley 6221 source meter was used to apply 2 mA and a lock-in amplier was used to measure voltages as it gives consistently good resolution of 2 nV. The magneto-transport properties were measured in a helium flow cryostat where magnetic field was 3 T. The magnetic field and charge current were both applied parallel to the easy axis of the Co/C_{60} thin film. The resistance of the sample was measured while the sample cooled down from 300 K to 5 K. This measurement presented a metallic behaviour of Co/C_{60}

bilayer where the resistance decreases as the temperature is lowered as shown in Figure 3.19.

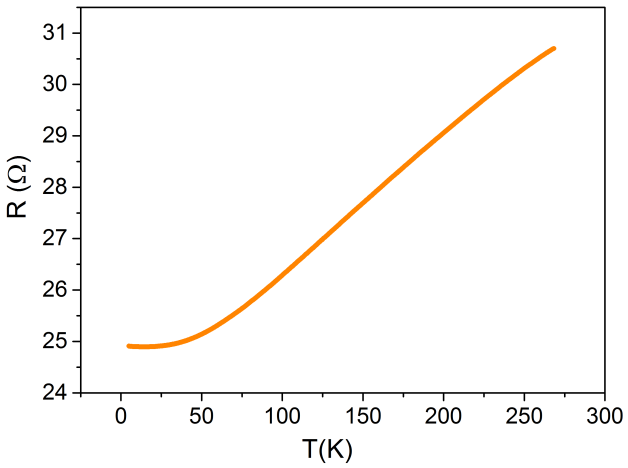

Figure 3.19: Raw resistance (R) data against temperature (T) for a sample of Ta(4 nm)/Co(3 nm)/C_{60}(35 nm)/Al(10 nm).

CHAPTER 4

Magnetic characterisation of Fe/RF-sputtered amorphous carbon interfaces

4.1 Introduction

This chapter introduces the magnetic properties of iron (Fe) with RF-sputtered amorphous carbon (a-C) thin films. The hybridisation between the d orbitals of the transition metal and the π carbon electrons leads to the formation of hybrid interfaces. A different Fermi level for the carbonbased material and the transition metal (as discussed in Chapter 2) leads to charge transfer at the interface. The charge transfer at the hybrid interface results in unexpected changes in the electronic and magnetic properties of the structure [8, 21, 28, 31, 32, 34, 139]. In this chapter, we investigate the magnetism of ferromagnetic metal (iron) thin films and RF-sputtered amorphous carbon before and after annealing. Annealing is used in this research due to the possibility of altering the bonding, orbital states, metallic coupling and structure of the carbon atoms.

In order to investigate interfacial effects between 3d ferromagnetic metals and RF-sputtered a-C, bilayer (Fe/a-C) and trilayer (Fe/a-C/Fe) structures were deposited via sputtering deposition at a base pressure of 10^{-8} Torr. These structures were investigated using SQUID-VSM, Kerr microscopy, TEM and Raman spectroscopy. The magnetometry (SQUID-VSM) results form a major part of this study, as they show the magnetic moment of the samples before and after annealing, with high sensitivity of about 10^{-8} emu (typically the moment of post-annealing samples in Fe/RF-sputtered a-C is of the order of 10^{-5} emu and 10^{-4} emu).

The temperature dependence of the magnetisation M_s (T) and coercivity H_c (T) was also investigated in Fe/RF-sputtered a-C, both in as-deposited and annealed samples. Raman spectroscopy was used to observe the change in the vibration modes of the carbon interfaces before and after annealing. Kerr microscopy was used to image the domain structure and make a comparison in domain size between as-deposited and annealed samples. Cross-section transmission electron microscopy (TEM) was used to check for iron and carbon diffusion.

4.2 Magnetometry of Fe/RF-sputtered a-C before annealing

4.2.1 Bilayer-system

We studied the thickness-dependent magnetic properties of Fe/RF-sputtered a-C grown on Si/SiO_2 substrates using SQUID-VSM magnetometry. The substrates were cut to 4 mm $\times$ 4 mm and cleaned in acetone and isopropanol (IPA) using an ultrasonic bath for approximately 5 minutes, then dried with compressed air before mounting in a vacuum chamber.

To investigate the magnetic effects of the Fe/RF-sputtered a-C, we deposited samples with the structure Ta(3 nm)/Fe(t)/RF- sputtered a-C(5 nm)/Al(5 nm), where (t) ranged from 3 nm to 20 nm. Fe/RF-sputtered a-C bilayers were deposited on top of a 3 nm thick layer of Ta to prompt Fe crystalline growth [140–142]. Control samples were also deposited for comparison by growing Ta(3 nm)/Fe(t)/Al(5 nm) without the a-C layer, where (t) also ranged from 3 nm to 20 nm. The control samples were measured in order to investigate the changes induced by coupling ferromagnetic material (Fe) and RF-sputtered a-C.

Magnetometry measurements of a typical bilayer system of Fe/RF-sputtered a-C show that the magnetisation changes due to RF-sputtered a-C are dependent on the thickness of the ferromagnetic (Fe) layer, as shown in Figure 4.1. Fe thin films $<$ 15 nm thick with a 5 nm RF-sputtered a-C layer on top have a lower magnetisation, which indicates that the bulk properties of Fe are fully apparent only when the metallic layer is thick enough. The dependence of the magnetisation on the thickness of the ferromagnetic layer arises for different growth number. These findings highlight the interfacial effect between ferromagnetic materials and RF-sputtered a-C due to hybridisation between the carbon and 3d metals band,and charge transfer at Fe/RF-sputtered a-C interfaces [27, 30]. In order to exclude the hybridisation and charge transfer effects across the interfaces, control samples without RF-sputtered a-C were measured and subtracted from the samples with the RF-sputtered a-C. The change in magnetisation between the samples with/out the RF-sputtered a-C is shown in Figure 4.1.

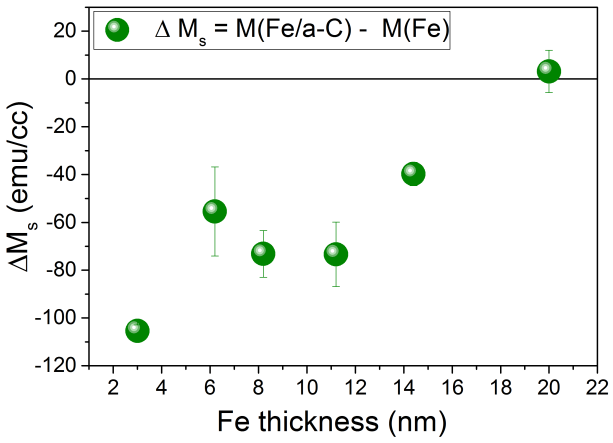

Figure 4.1: Room temperature measurements show magnetisation dependence on thickness of Fe films with structure of Ta(3)/Fe(t)/RF-sputtered a-C(5)/Al(5) compared with control samples of Ta(3)/Fe(t)/Al(5), where (t) is varying Fe thicknesses from 3 to 20 measured by SQUID-VSM. All thicknesses in brackets are in nm. The M_s here is the average value measured of about 10 samples at specific thicknesses.

The coercivity of our thin films is also dependent on the metallic layer thickness. In this work, the coercivity was measured to characterise metallo-molecule interfaces for the same sample structures [Ta(3 nm)/Fe(t)/a-C(5 nm)/Al(5 nm)] with and without RF-sputtered a-C. The measurements show that the coercivity is dependent on the thickness of the Fe layer at room temperature. Decrease in the coercivity appeared when RF-sputtered a-C was introduced into the structure, as presented in Figure 4.2, which shows the hysteresis loops measured at 300 K for a typical structure of Ta(3 nm)/Fe(12 nm)/a-C(5 nm)/Al(5 nm) and also without RF-sputtered a-C [Ta(3 nm)/Fe(12 nm)/Al(5 nm)].

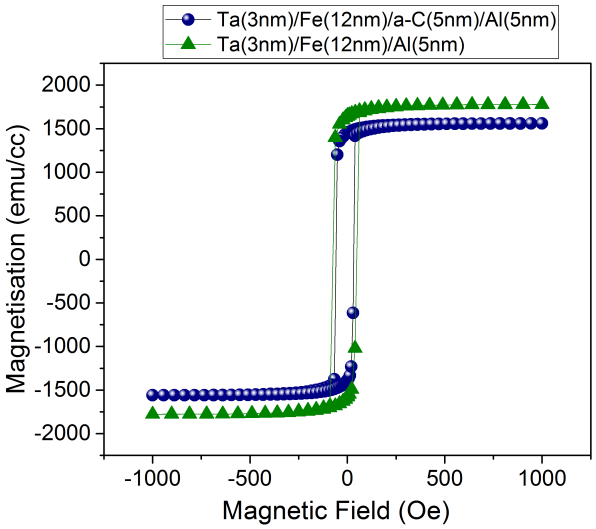

Figure 4.2: Hysteresis loops of Fe/RF-sputtered a-C and Fe taken at 300 K. They show a decrease in the coercivity of 70 Oe and a 5-10 % lower magnetisation when 5 nm of RF-sputtered a-C is introduced in the sample structure.

The coercivity H_c as a function of Fe thickness is plotted for samples with and without the RF sputtered a-C as shown in Figure 4.3a. The maximum change in coercivity was observed in samples with Fe layer thickness of 9.5 nm. The coercivity value of these samples dropped from 88 Oe to 59 Oe. Figure 4.3b shows the change in the H_c between Fe and Fe/a-C is dependent on the thickness of the magnetic layer (Fe), where H_c is the average value measured for 10 samples at each thickness. This change in H_c could be evidence that hybridisation at metal-nanocarbon interfaces leads to change in anisotropy [143] or spin orbital coupling. These experimental observations may underline that the RF-sputtered a-C has a strong effect on the coercivity of Fe. Achieving the smooth and symmetrical interface of magnetic layers is highly desirable in digital technology [144]. RF-sputtered a-C might be a good choice of material for this kind of application.

(a)

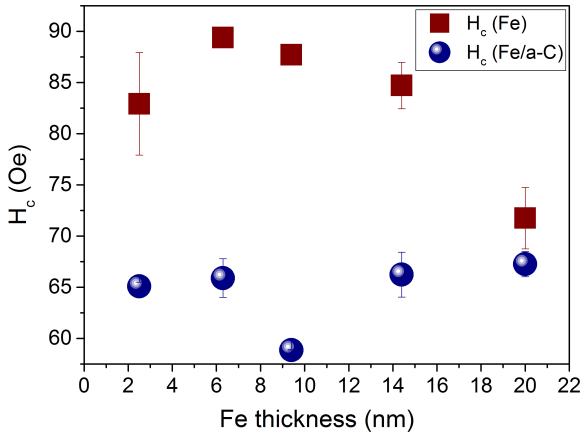

(b)

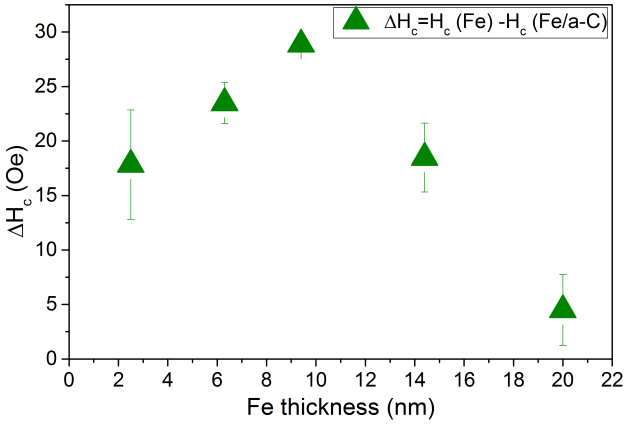

Figure 4.3: Coercivity extracted from hysteresis loops measured for all samples at room temperature, plotted as a function of Fe thickness. (a) H_c as a function of Fe thicknesses from 2.5 nm to 20 nm for samples of structure of Ta(3 nm)/Fe(t)/a-C(5 nm)/Al(5 nm) and Ta(3 nm)/Fe(t)/Al(5 nm). (b) The difference in coercivity between Fe and Fe/a-C as a function of Fe thickness at 300 K. The H_c here is the average value measured of about 10 samples at specific thicknesses.

4.2.2 Trilayer-system

The studied samples here are tri-layers of Fe(t)/RF-sputtered a-C(R)/Fe(t), with 1 nm $<$ t $<$ 21 nm and 0.2 nm $<$ (R) $<$ 11 nm where (t) represents the thickness of Fe and (R) is the thickness of RF-sputtered a-C.

Figure 4.4. shows samples with two Fe layers (10 nm) separated by an RF-amorphous carbon layer; the thickness of the RF-amorphous carbon was varied from 0 to 8 nm to investigate how the thickness of this layer affects the magnetic properties. Room temperature measurements for the samples with carbon thicknesses of 1 and 2 nm show a large decrease in coercivity that could indicate the transfer of charge from the magnetic layers to the carbon layer. The samples were measured in collaboration with Alistair Walton an undergraduate student under my supervision. This effect, shown at specific thicknesses, may indicate that the softness of the Fe/a-C/Fe system depends on how thick the layers are. RF-sputtered a-C layer has grown in between Fe layers that may be lead to make the system much softer. The measured H_c is observed to decrease dramatically with increasing RF-sputtered a-C layer, and may be due to greater roughness in this layer.

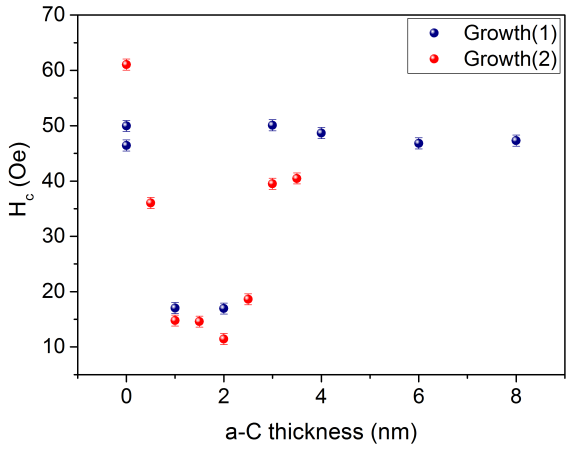

Figure 4.4: Coercivity plotted against RF-sputtered a-C (a-C) thickness. Various thicknesses of RF-sputtered a-C were measured at room temperature for different growth. The sample structure is Ta(3)/Fe(10)/a-C(t)/Fe(10)/Ta(5) and all thicknesses are shown in nm.

In order to investigate the effect of Fe thickness on this Fe/a-C/Fe system, different thicknesses of RF-amorphous carbon were grown between 2, 6.5, 10 and 20 nm of Fe, and capped with Al and measured before annealing using SQUID. Figure 4.5a shows the room temperature magnetisation corresponding to a samples with the structure of Ta(3 nm)/Fe(t)/a-C(R)/Fe(t)/Al(5 nm), where (R) is varied from 0.5 to 11 nm of RF-sputtered a-C thick, and (t) is varied to 2, 6.5 , 10 and 20 nm of Fe thick. The saturation magnetisation in samples before annealing is dependent on the thickness of the metallic layers where the M_s is increased with increasing the thickness of the Fe. The thickness of the Fe and RF sputtered a-C films has a significant influence on the magnetic properties [145]. The coercivity does not change when Fe layers are 6.5,10 and 20 nm, whereas 2 nm of Fe layers shows changes in H_c especially when the nanocarbon layer is less than 8 nm, as shown in Figure 4.5b. This could be due to a non-continuous or very thin layer of RF-sputtered a-C. Figure 4.5b also does not appear to show a minimum in the coercivity at the thin layer of RF-sputtered a-C as shown in Figure 4.4. This could be affected by the Al cap layer.

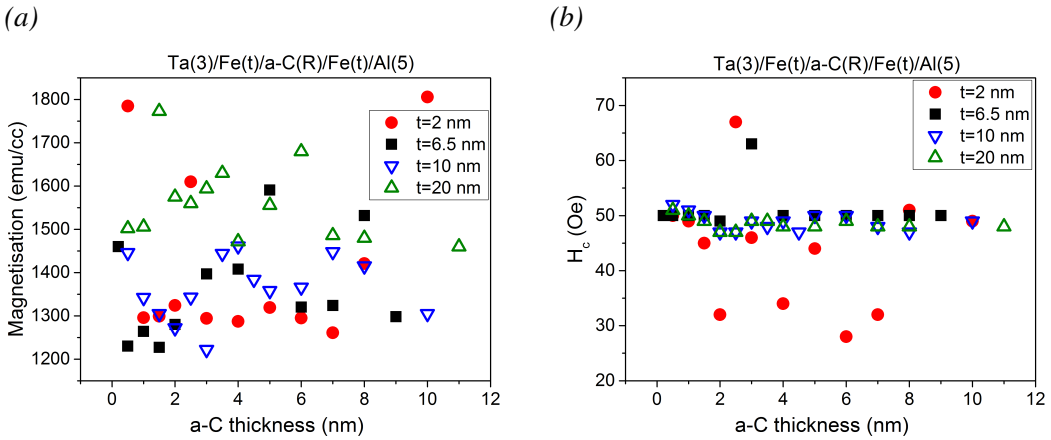

Figure 4.5: (a) The saturation magnetisation (b) coercivity verses RF-sputtered a-C (a-C) thickness. Various thicknesses of RF-sputtered a-C were measured at room temperature for different Fe thickness. The sample structure is Ta(3)/Fe(t)/a-C(R)/Fe(t)/Al(5) and all thicknesses are shown in nm, with $1 < t < 21$ and $0.2 < (R) < 11$ where (t) represent the thickness of Fe and (R) shows the thickness of RF-sputtered a-C.

4.2.3 Multilayer-system

The saturation magnetisation and coercive field of multi-layered samples of Ta(3 nm)/[Fe(10 nm)/a-C(5 nm)]x/Al(5) have been studied in order to investigate the coupling between magnetics layers before annealing. The number of interface layers (x) was varied from 2 to 5. Figure 4.6a shows a magnetisation of about 1600 emu/cc for the as-deposited samples except (3 nm) of Fe which shows a high magnetisation of about 1800 emu/cc. This could be result for the growth condition so the magnetic properties of the samples can be affected by various parameters, for example, the deposition pressure and substrate alignment. The coercive field is reduced from 50 Oe to 25 Oe when the number of repeat increases as shown in Figure 4.6b. This could be explained by increasing the RF-sputtered a-C content the charge transfer is raised from Fe to carbon layer [146]. Alternatively, the reduced H_c may be the result of decreasing the roughness with increasing number of interfaces.

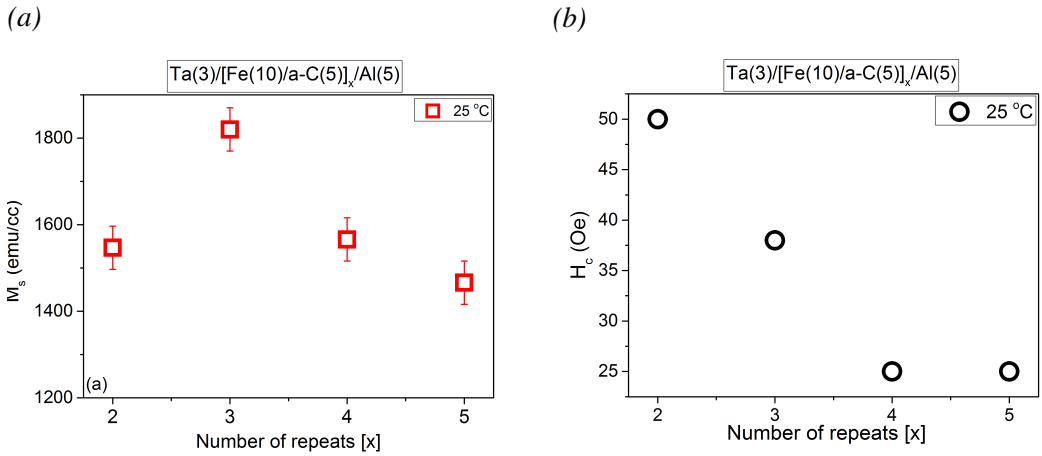

Figure 4.6: The dependence of (a) the saturation magnetisation (b) coercive field on the number of repetitions for Ta(3 nm)/Fe(10 nm)/RF-sputtered a-C(5 nm)/Al(5 nm) for as-deposited thin films. The samples ran from two repetitions (x=2) [Fe(10 nm)/RF-sputtered a-C(5 nm)]$_x$ to five repetitions (x=5).

4.3 Magnetometry of Fe/RF-sputtered a-C after annealing

4.3.1 Bilayer-system

Carbon-based materials have attracted attention due to their spin and structural properties [27, 32, 44, 147] . The effect of annealing at inorganic/organic interface has been also studied in samples of Ta(3 nm)/Fe(t)/a-C(5nm)/cap layer (5 nm). Aluminium (Al) and niobium (Nb), which have different melting points, were used as cap layers. Magnetic characterisation was obtained in samples annealed in the temperature range of 100 °C to 750 °C and measured in the SQUID-VSM magnetometer. The magnetic field up to 2 kOe was applied in plane along the easy axis of samples. The annealing process was done using a tube furnace in vacuum (10^{-5} Torr) for one hour. The typical sample size was 4mm $\times$ 4mm, being the optimum size for SQUID-VSM magnetometry.

4.3.1.1 Dependence of M_s on annealing temperature

The magnetisation at different temperatures was measured for samples as a function of an in-plane applied magnetic field up to 2 kOe to ensure that the thin films were saturated (Figure 4.7a). In hard magnetic thin films, remanence ratio is an important parameter [148]. The sample of a Ta(3 nm)/ Fe(10nm)/RF-sputtered a-C(5nm)/Al(5nm) measured in-plane and we calculated the remanence ratio. The results in Figure 4.7b show an initial decrease of M_r/M_s with annealing temperature. This may suggest that the annealing temperature play a significant key role in the magnetic anisotropy of the Fe/RF-sputtered a-C thin films. From the hysteresis loops, the saturation magnetisation M_s was extracted at different annealing temperatures for samples with different capping layers. There is an increase in the magnetisation when the samples were annealed up to 200 °C as presented in Figures 4.8. However, the magnetisation drops with further annealing above 400 °C for both samples capped with Al or Nb, as indicated in Figures 4.8a and 4.8b. These measurements can be understood as follows. The increase in magnetisation at annealing temperature of 200 °C may be evidence of changes in the Fe/RF-sputtered a-C structure. The data also shows that at 600 °C the magnetisation reached a value of 730$\pm$20 emu/cc for samples capped by Al, whereas the M_s value at 750 °C is 365$\pm$1 emu/cc for samples capped by Nb. The most probable explanation for this reduction in magnetisation is the metal/carbon diffusion resulting from annealing at high temperature. An another reason is that could be result in forming non-magnetic iron carbide layer at the Fe/a-C interfaces after annealing and also crystalline the system [147, 149].

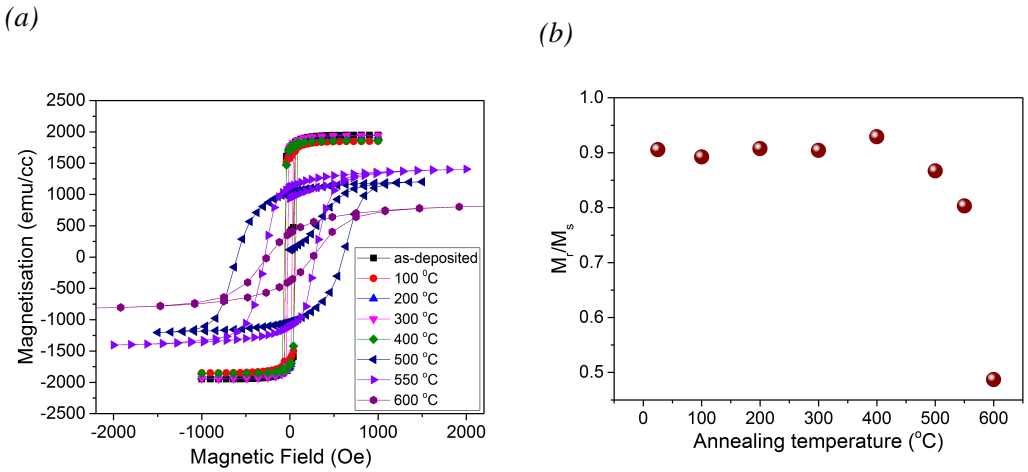

Figure 4.7: (a) Hysteresis loops of a Ta(3 nm)/Fe (10nm)/RF-sputtered a-C(5nm)/Al(5nm) sample measured in in-plane magnetic field. The measurements were obtained at room temperature for the as-deposited sample, and after annealing up to 600 °C. The bulk magnetisation in Fe which is about 1750 emu/cc [150, 151]. (b) Plots of M_r/M_s ratios against temperature (T) for Ta(3 nm)/Fe(10nm)/RF-sputtered a-C (5nm)/Al(5nm) samples.

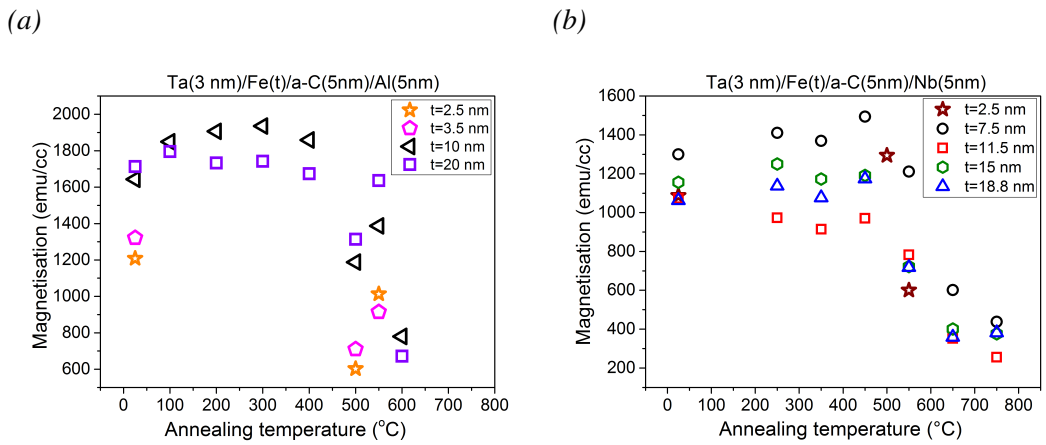

Figure 4.8: Magnetisation dependence on annealing temperature for different Fe concentrations using different capping layers. (a) Ta(3nm)/Fe(t)/RF-sputtered a-C(5nm)/Al(5nm).(b) Ta(3nm)/Fe(t)/RF-sputtered a-C (5nm)/Nb(5nm). The films were annealed at different temperatures for one hour in a vacuum. The first data points (at 25 °C) represents the samples before annealing.

4.3.1.2 Dependence of H_c on annealing temperature

This section describes the changes in H_c for Fe/RF-sputtered a-C interfaces as the annealing temperature is increased. Demonstrating the effect of post-annealing on H_c is perhaps the most interesting part of this research. In order to explore the impact of interfacial coupling between Fe and RF-sputtered a-C on the H_c Figure 4.9 shows the changes in H_c as a function of the annealing temperature in the range of 100 °C to 750 °C. H_c show the interfacial coupling and a significant reduction seems to be a factor of ~ 2 comparing to as-deposited samples up to annealing temperatures of 400 °C. However, above 500 °C the annealed thin films showed a significant increase in coercivity from 60 Oe in as-deposited films to 600 Oe. This change in coercivity when the samples were annealed above 500 °C can be attributed to diffusion, formation of pinning points, formation of carbides and/or the changes in carbon structure from amorphous to nano-crystalline. Formation of iron carbide should not take place until we reach $\sim$ 600 °C [152] when the coercivity drops in Fe/RF-sputtered a-C. The carbon diffusion may affect the coercivity, which could make the Fe/RF-sputtered a-C system into a hard material so RF-sputtered a-C magnetically hardens Fe after annealing. Another possible reason of increasing H_c is that the crystallinity of the thin films rises after annealing [43]. Krishnan et al showed the formation of crystalline Fe_3C after annealing the Fe/C multilayers at 500 K in a vacuum [147].
The interfacial effect in a metallo-carbon system appears to cause an increase in coercivity as a function of annealing temperatures, leading to the possibility of making Fe/RF-sputtered a-C thin films with a controlled value of coercivity (H_c). As a result, Fe/RF-sputtered a-C may become important in many applications requiring hard materials.

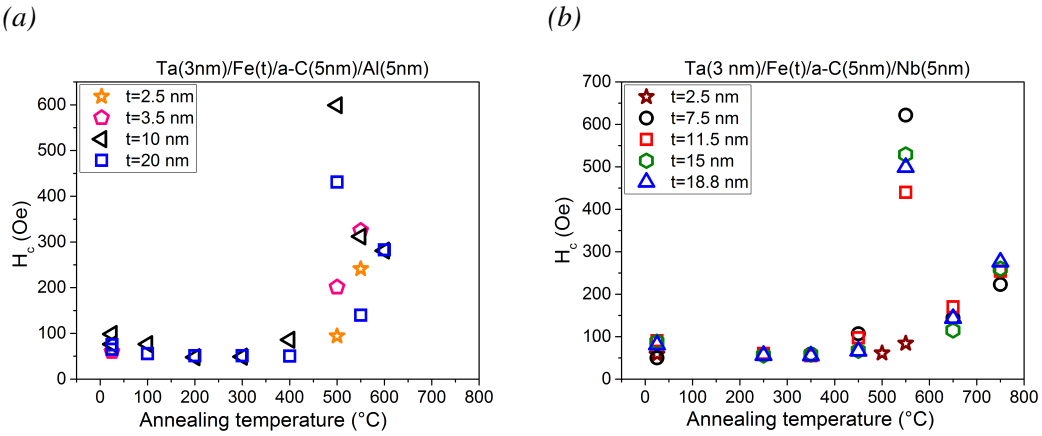

Figure 4.9: Effect of annealing temperatures on coercivity using different capping layers (a) 5 nm of Al (b) 5 nm of Nb. All of the samples were grown on top of Fe/RF- sputtered a-C with the structure and Si/SiO_2/Ta(3 nm)/Fe(t)/a-C(5nm)/cap (Al (5nm)) or (Nb (5nm)) from bottom to top, where 2 nm $<$ (t) $<$ 20 nm. The H_c values were extracted from in-plane M-H loops measured at room temperature.

4.3.2 Trilayer-system

In order to investigate the effect of annealing on the Fe/a-C/Fe system with carbon -mediated iron layers coupling, RF-amorphous carbon layers were grown between 2, 6.5, 10 and 20 nm thick of Fe films, and measurements after different annealing temperatures were made using SQUID. Figure 4.10a shows the magnetisation corresponding to a samples with the structure of Ta(3 nm)/Fe(6.5 nm)/a-C(t)/Fe(6.5 nm)/Al(5 nm), where (t) is varied from 0.5 to 9 nm thick, obtained in as-deposited and annealed samples. The saturation magnetisation in the samples before annealing dose not indicates much changing for all Fe thickness. The coercivity of trilayered samples for all thickness reaches a maximum value after annealing at 550 °C when the RF-sputtered a-C layer is approximately 3 nm. This could be due to improvements in the roughness and crystalline structure of the thin films after annealing, leading to a strong increase in coercivity [153]. The thickness of the Fe and RF-sputtered a-C films also has a significant influence on the magnetic properties [145]. The coercivity does not change before annealing and with the increase in annealing temperature when the nanocarbon layer is less than 2 nm, as shown in Figure 4.11a. This could be due to a non-continuous layer of RF-sputtered a-C. However, the magnetisation of this sample reduces as the

annealing temperature is increased. The magnetisation and coercivity in Figures 4.10 and 4.11 are extracted from the same samples.
Figures 4.10 and 4.11 also show M_s and H_c for different Fe thickness (2 nm,10 nm and 20 nm). The same trend appeared as shown in Figures 4.10a and Figures 4.11a when the Fe thickness was 6.5 nm. This observation can be attributed to crystallisation of the RF-sputtered a-C at 500 °C - 600 °C and its diffusion into the metallic layer. To clarify the above results more samples were studied in which both the Fe and RF-sputtered a-C thickness was varied. All of the results show clearly that the smaller thicknesses of both metallic and nanocarbon layers have showed no or small and a continuous interface is critical.

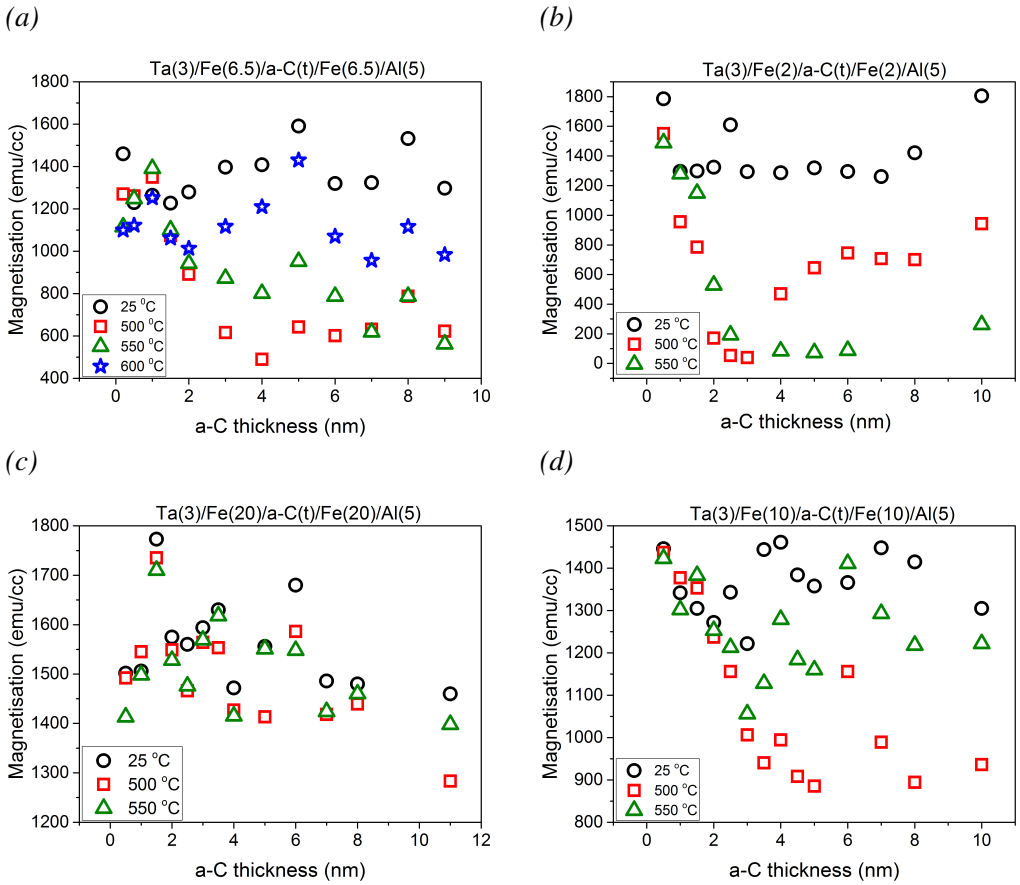

Figure 4.10: The variation of saturation magnetisation with the thickness of RF-sputtered a-C for trilayers of Fe(t)/RF-sputtered a-C (R)/F(t), with $1 < t < 21$ and $0.2 < (R) < 11$ where (t) represent the thickness of Fe and (R) shows the thickness of RF-sputtered a-C with (a) Fe= 6.5 nm thick layer, (b) Fe= 2 nm thick layer, (c) Fe= 20 nm thick layer, and (d) Fe= 10 nm thick layer. All the data points presented are extracted from hysteresis loops at room temperature as-deposited or after annealing at 500, 550 and 600 °C.

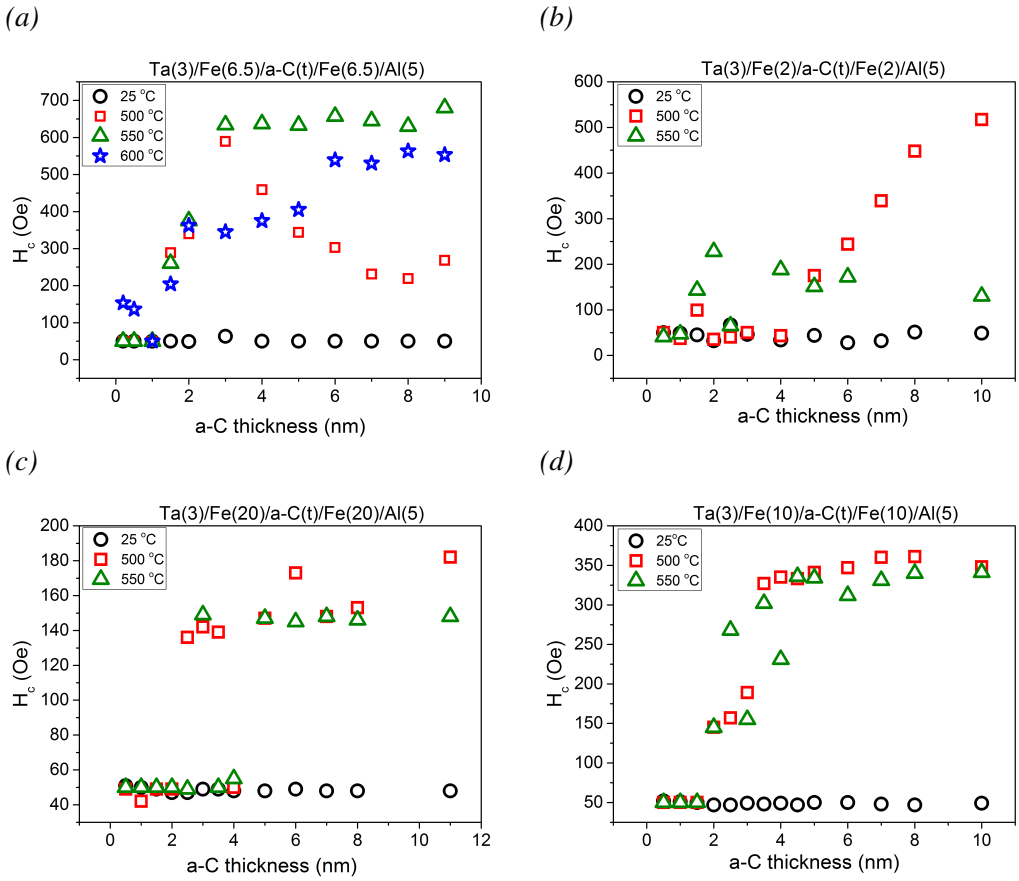

Figure 4.11: The variation of the coercivity with the thickness of RF-sputtered a-C for trilayers of Fe(t)/RF-sputtered a-C (R)/Fe (t), with $1 < t < 21$ and $0.2 < (R) < 11$ where (t) is the thickness of Fe and (R) is the thickness of RF-sputtered a-C with (a) Fe= 6.5 nm thick layer, (b) Fe= 2 nm thick layer, (c) Fe= 20 nm thick layer, and (d) Fe= 10 nm thick layer . All the data points presented are extracted from hysteresis loops measured at room temperature. All the samples were measured before annealing and after annealing up to 600 °C.

To observe and clarify the RF-sputtered a-C thickness effects on the trilayer magnetic properties the remanence ratio are studied. The magnetic field was applied in plane along the easy axis of samples. Remanence ratios M_r/M_s are plotted as a function of RF-sputtered a-C thickness as-deposited and after annealing the samples at 500 °C and 550 °C as shown in Figure 4.12. M_r/M_s ratio is dropped from 0.95 to 0.82 with further RF-sputtered a-C thickness increasing. M_r/M_s ratio is also enhanced after annealing the samples at 500 °C and 550 °C. The M_r/M_s ratio could be indirectly af-

fected by the magnetic anisotropy [154], which is enhanced after annealing at 500 and 550 °C. The formation of domains after annealing leads the magnetisation to align in a certain crystallographic direction that could enhance the magnetic anisotropy.

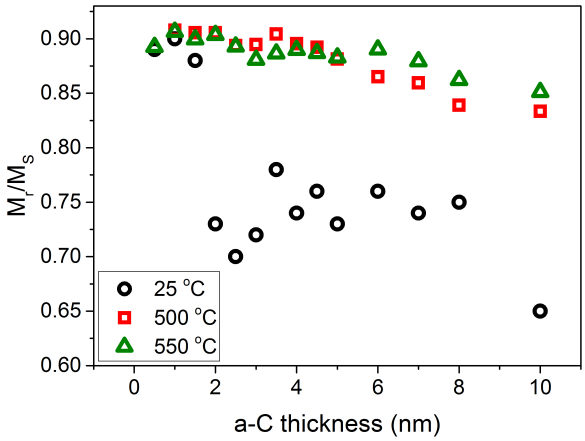

Figure 4.12: Shows the remanence ratio of Ta(3 nm)/Fe(10 nm)/a-C(t)/Fe(10 nm)/Al(5 nm), where (t) varied from 0.5 nm to 10 nm. M_r/M_s decreased with the increase of RF-sputtered a-C for all samples as- deposited and annealed at 500 °C and 550 °C.

4.3.3 Multilayer-system

The saturation magnetisation and coercive field of multi-layered samples of Fe/RF-sputtered a-C have been studied before annealing see section 4.2.3.In order to investigate the magnetics layers coupling after annealing the RF-sputtered a-C layer thickness was kept constant, at 10 nm and 5 nm respectively. The number of interface layers was varied from 2 to 5. Figure 4.13a shows the reduced magnetisation as the samples were annealed. This drop in magnetisation could be attributed to changes in crystallinity after annealing. This changing in the M_s after annealing may be due to the formation of a non-magnetic dead layer at the Fe/RF-sputtered interface [147]. A reduction in M_s has been reported in Fe_3C multilayers after annealing at 500 K. H_c shows a strong decrease with $t_{(FM)}$ in Fe_3C multilayers [147]. However, we found that the annealed samples exhibit an increase in coercivity from 50 Oe up to 350 Oe with increasing temperature as shown in Figure 4.13b. Here, the hybridisation effect between the π

carbon orbital and 3d metals band could play a significant role in altering the magnetic properties in interfacial coupling. The magnetisation and the coercive field exhibited consistent results in relation to the number of repetitions in the metallic-nanocarbon interfaces. Further AFM study is required to confirm the roughness dependence on the number of interfaces as reported in Cu/C_{60} system [91].

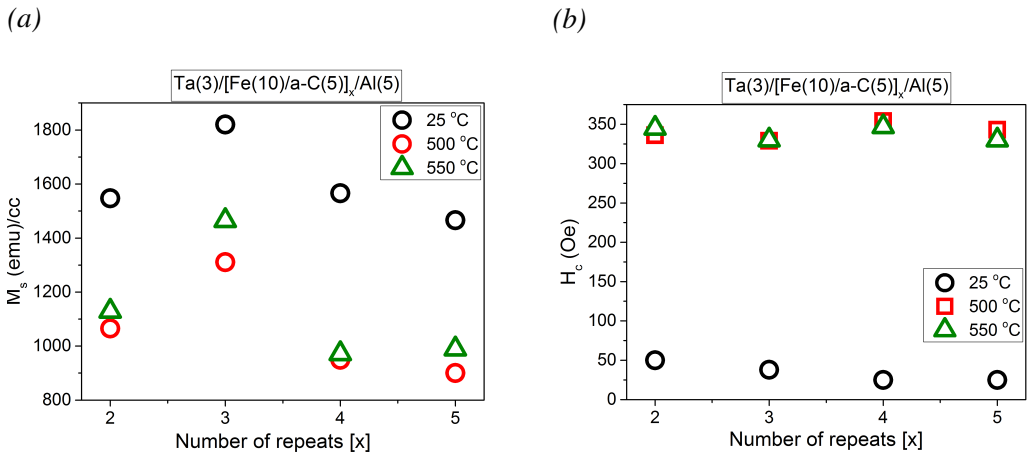

Figure 4.13: (a) The magnetisation versus the number of repetitions for Ta(3 nm)/Fe(10 nm)/RF-sputtered a-C (5 nm)/Al(5 nm) (b) The dependence of the coercivity on the number of interfaces for as-deposited and annealed samples. The samples ran from two repetitions (x=2) [Fe(10 nm)RF-sputtered a-C (5 nm)]$_x$ to five repetitions (x=5). All the samples were annealed at different temperatures for an hour under a vacuum (10^{-5} Torr).

4.4 Effect of the RF-sputtered a-C layer thickness on the magnetic properties after annealing

Here we explore how the thickness of the RF-sputtered a-C layer affects the magnetic properties of the samples. The studied samples have structure of Si/SiO_2/Ta(3 nm)/Fe(10 nm)/RF-sputtered a-C(t)/Al (5 nm), where (t) is varied from 0.5 nm to 25 nm. The magnetisation and the coercive field of the samples with different RF-sputtered a-C thickness are shown in Figure 4.14. In this experiment, the samples were heated to 500 °C and 550 °C at 10^{-5} Torr for one hour. As before, the magnetisation (M_s) and the coercivity (H_c) were measured at room temperature before and after

annealing. Before annealing, the measurements show that the magnetisation and the coercivity were slightly changed when the RF-sputtered a-C thick below 10 nm. After annealing the samples, a dependence on the thickness of the RF-sputtered a-C layer for annealed samples was observed. The M_s is decreased, whereas H_c is increased after annealing. This dependence is clearly observed for RF-sputtered a-C layers 2 nm and above see Figures 4.14a and 4.14b. The changing in the magnetic properties after annealing might be due to the formation of a non-magnetic dead layer at the Fe/RF-sputtered interface [147] as indicated in our Fe/RF-sputtered a-C multilayers after annealing.

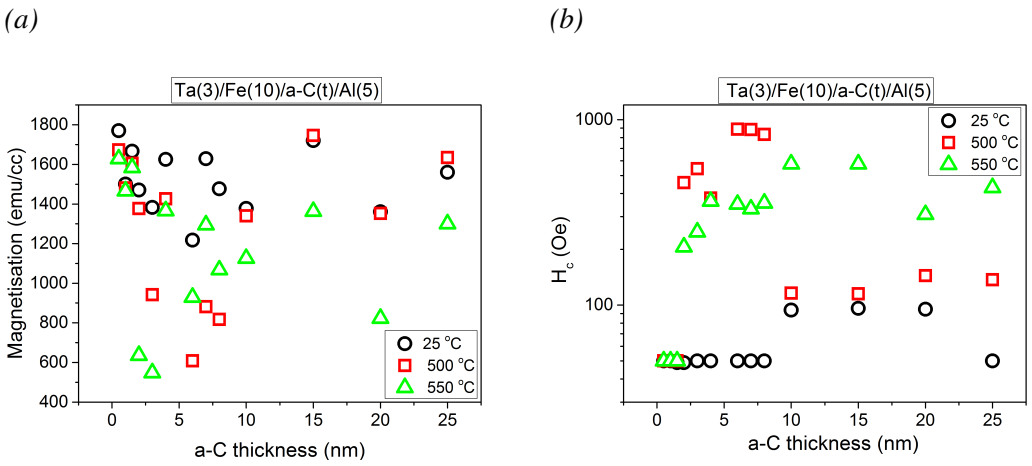

Figure 4.14: (a) Magnetisation (b) coercivity dependence on the thickness of RF-sputtered a-C for films with the structure Ta(3nm)/Fe(10nm)/a-C(t)/Al(5 nm), where (t) ranged from 0.5 nm to 25 nm. The magnetisation and coercivity measurements were performed at room temperature and the calculations of M_s performed by considering the thickness of the Fe layer.

4.5 Magneto-optical Kerr effect microscopy

To understand changes in coercivity, Kerr microscopy was used. A sample of Ta (3 nm)/Fe(20 nm)/a-C(5 nm)/Al(5 nm) grown on silicon dioxide was imaged before and after annealing at the specific annealing point where a change in the coercivity was measured see, Figure 4.15. The domains observed at the coercive field are much smaller and with lower contrast image after annealing the sample.

The data taken from both SQUID-VSM magnetometry and magneto-optic Kerr microscopy (μ MOKE) show changes in the hysteresis loop and the magnetic images, see Figure 4.15. Kerr images can offer information about samples pinning after applying an in-plane magnetic field. This could be expected because the density of pinning sites may increase when the Fe is diffused along grain boundaries and crystallised upon cooling. Pinning points are observed in the images that could also be due to structural defects in the sample.

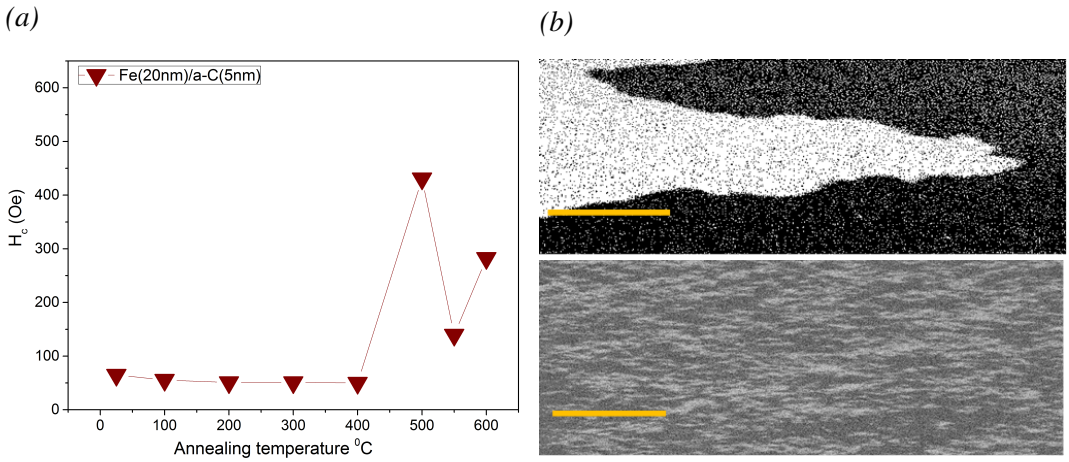

Figure 4.15: (a) The dependence of the H_c on the annealing temperature of sample with 20 nm of Fe thickness. (b) Magneto-optic Kerr microscopy (μMOKE) images taken at H_c show that an as-deposited sample of Ta(3 nm)/Fe(20 nm)/a-C(5 nm)/Al(5 nm) has large domains before annealing (top right image) whereas annealing the same sample at 500 °C (H_c peak) for 10 h reduces greatly the domain size (bottom right image). Scale bars are 100 μm.

4.6 Magnetic energy product $(BH)_{max}$ in the Fe/RF-sputtered a-C system

There is a demand for permanent magnets for use in different industrial applications, and nowadays these are manufactured mostly using rare earth materials [46]. Permanent magnets require high magnetic flux density (B) with high coercivity (H_c), since both of these parameters generate maximum magnetic energy products ($(BH)_{max}$) [155].

The magnetic energy product (BH) was calculated from both magnetisation and coercivity for the samples (equation 2.21). Figure 4.16a shows the calculated BH product for the samples with two different capping layers of Ta(3 nm)/Fe(t)/a-C(5 nm)/Al(5 nm) and Ta(3 nm)/Fe(t)/a-C (5 nm)/Nb(5 nm), with Fe thickness ranging from 7.5 nm to 20 nm. In these two structures the maximum value of coercivity was about 600 Oe after annealing at 500 °C, as shown in Figure 4.16; with the calculated maximum magnetic energy product at about 53 kJ/m^3. This value, according to the literature, lies between Alnico and ferrites [47], as shown in Figure 4.16b.

C_{60} was also introduced to the samples structure on top of RF-sputtered a-C. The objective was to use C_{60} to enhance the changes in the magnetic properties of ferromagnetic metals. The sample with a C_{60} layer has a structure of Si/SiO_2/Ta(3 nm)/Fe(10 nm)/a-C(5 nm)/C_{60}(20 nm)/Nb(5 nm). It was annealed in-situ in the SQUID-VSM up to 750 °C. The magnetometry measurements show that the $(BH)_{max}$ in the Fe/RF-sputtered a-C system was not greatly affected by the additional layer of C_{60} (20 nm). Also, the diffusion of RF-amorphous carbon into the Fe layer may allow the C_{60} to change the magnetic properties in the metallic-carbon structure. This gives an indication that hybridisation between the fullerene C_{60} (p_z orbital) and Fe (3d bands) was not formed due to the RF-sputtered a-C layer when the annealing temperature is below 500 °C. However, the results after using C_{60} in our system of Fe/a-C show a slight enhancement in the $(BH)_{max}$ value to 20 kJ/m^3 when the annealing temperature is above 500 °C. This shift in orbitals is consistent with the results obtained by Raman spectroscopy after annealing Fe/RF-sputtered a-C at 600 °C. After annealing at 600 °C, RF-sputtered a-C diffused into Fe leads to formation of carbide.

(a)

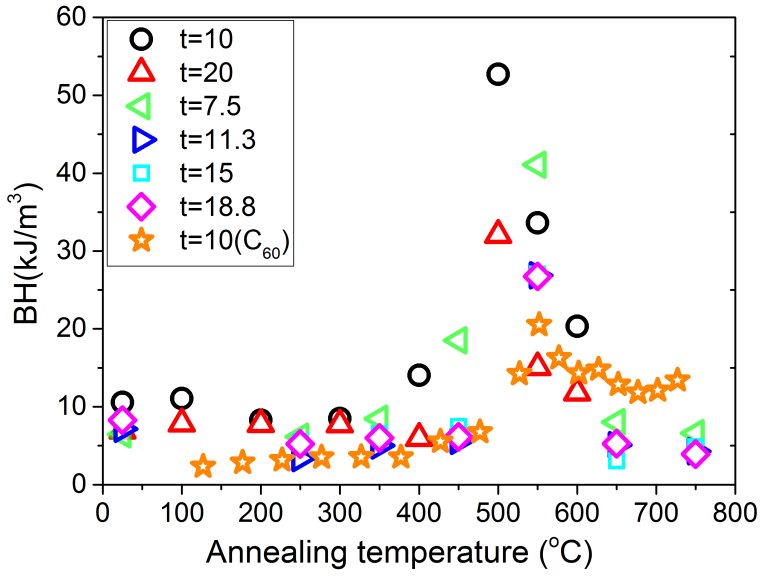

(b)

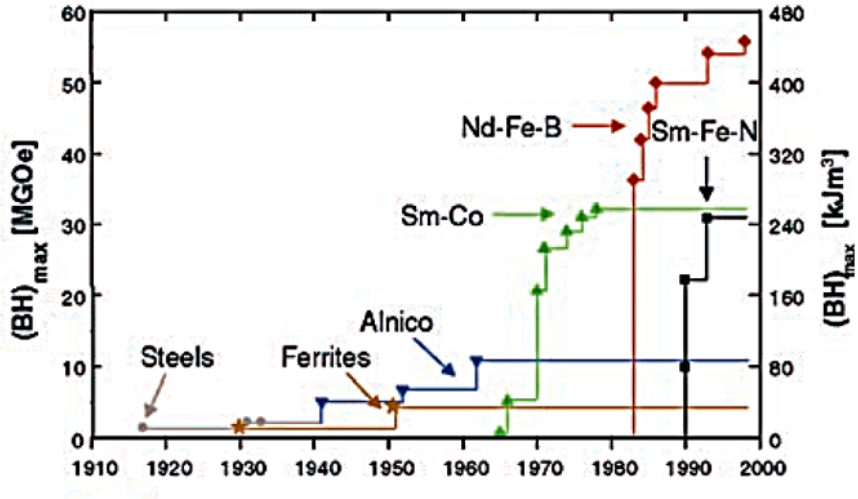

Figure 4.16: (a) The dependence of the energy product on the annealing temperature for samples of Fe/RF-sputtered a-C with different Fe thicknesses and Fe/RF-sputtered a-C/C_{60}. The BH values of Fe thicknesses only were calculated in order to derive the BH product. (b) This figure shows research carried out to develop the energy product of hard magnetic materials, taken from [47].

4.7 Raman spectroscopy and TEM characterisation at Fe/RF-sputtered a-C interfaces

4.7.1 Raman spectroscopy characterisation for Fe/RF-sputtered a-C bilayer before and after annealing

Raman spectroscopy measurements were carried out to investigate changes in the vibration modes of RF-sputtered a-C thin films in as-deposited and annealed films. We observed the change from amorphous carbon to a nano-crystalline graphite stage after annealing the thin films at 600 °C. The spectra after annealing show two peaks, the D and G vibration modes at 1360 and 1600 cm^{-1} respectively, as seen in Figure 4.17a. The G band occurs due to the stretching of C-C sp^2 sites in both rings and chains, whereas the D band is due to the breathing of the sp^2 present in rings only [122]. A sample of Ta(3 nm)/Fe(10 nm)/RF-sputtered a-C(5 nm)/Al(5 nm) was annealed at 100 °C - 600 °C for one hour in a vacuum 10^{-5} Torr. The Raman spectra of the Fe/RF-sputtered amorphous carbon with different annealing temperatures are presented in Figure 4.17b. Figure 4.17c shows the data extracted from these measurements, with a shift in the G peak position to higher frequencies from 1561 to 1598 cm^{-1}. At the same time, the ratio of I(D)/I(G) increases from 1.3 to 1.7 after annealing at up to 600 °C for one hour (Figure 4.17d).

With this information, we can confirm that the RF-sputtered a-C layer forms nano-crystalline graphite after annealing. This finding is consistent with the results we obtained in a Cu/RF-sputtered amorphous carbon system [58].

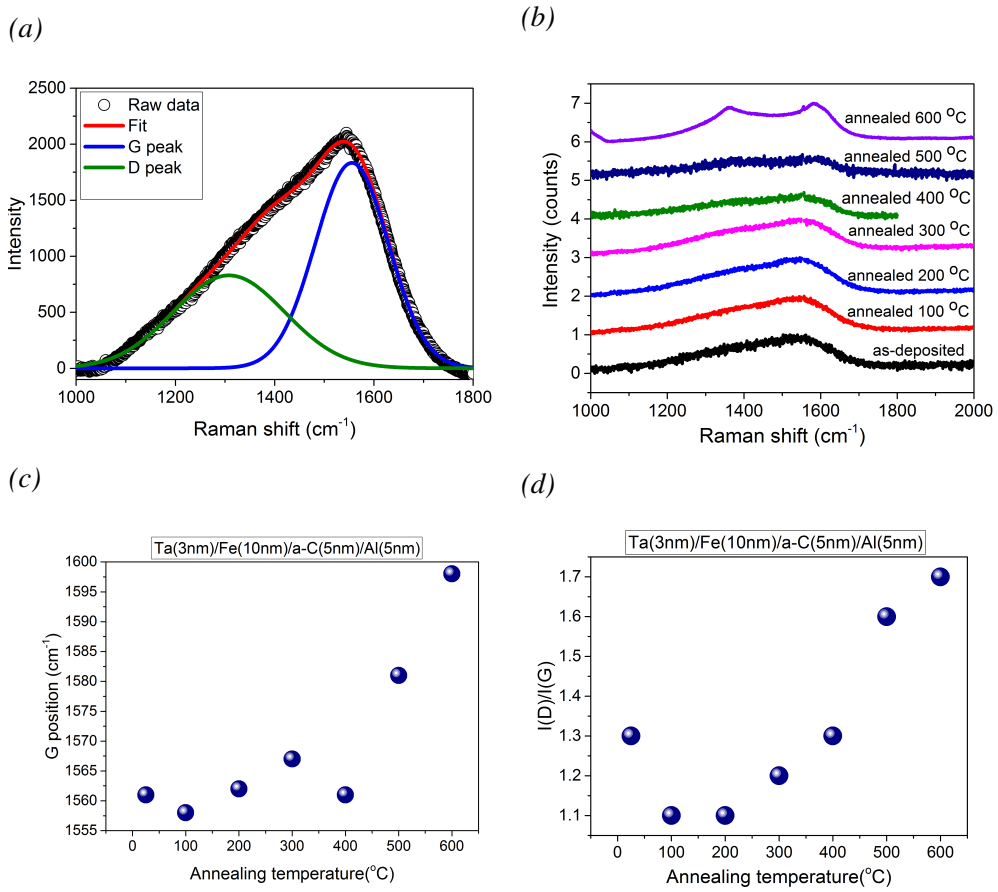

Figure 4.17: Raman spectrum for a sample of Ta(3nm)/Fe(10nm)/RF-sputtered a-C(5nm)/Al(5nm). (a) The (G and D) peaks as indicated by blue and green lines respectively. (b) The Raman spectrum at different annealing temperatures up to 600 °C. (c) The position of the G peak (cm^{-1}) and (d) the intensity ratio I(D)/I(G) are extracted from Raman measurements for sample at different annealing temperatures.Showing the change in sp^3 to sp^2 hybridisation. The data indicate movement from amorphous carbon (20% of sp^3) to nanocrystalline graphite (0% of sp^3) after annealing [130] as according to Figure 3.12.

4.7.2 Raman spectroscopy characterisation for Fe/RF-sputtered a-C trilayers before and after annealing

Raman measurements were also carried out for trilayer samples to compare with those in bilayers. Figure 4.18 shows the I(D)/I(G) and G positions of the as-deposited and annealed Fe(2 nm)/RF-sputtered a-C(t)/Fe(2 nm) trilayer film extracted from Raman

spectra measurements. The thickness of RF-sputtered a-C are varied from 4 nm to 10 nm. Below 4 nm, the Raman spectra cannot be obtained. The trilayer samples showed a shift in G position to higher frequencies and at the same time an increase in the ratio of intensities of I(D) to that of I(G). This observation strongly suggests that crystallisation of RF-sputtered a-C is possible above 500 °C [42] which is consistence with our observation in Fe/RF-sputtered a-C bilayer system.

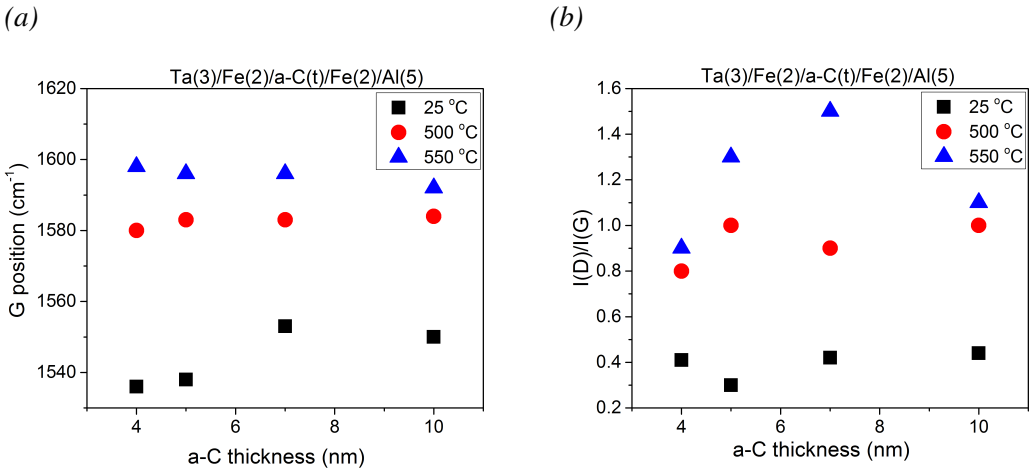

Figure 4.18: Raman spectra using a 473 nm blue laser with a 1800 grating. The shift in the G peak present in (a) and (b) increased the I(D)/I(G) ratio as the annealing temperature was increased. According to Figure 3.12, the ratio I(D)/I(G) indicate movement from amorphous carbon to nanocrystalline graphite. All of the data points are for films with the structure Ta(3nm)/Fe(2 nm)/RF-sputtered a-C (t)/Fe(2 nm)/Al(5nm), where (t) is varied from 4 to 10 nm thick.

4.7.3 Cross-section transmission electron microscopy (TEM) characterisation of Fe/RF-sputtered a-C bilayer before and after annealing

TEM images were taken of typical structures of Ta(3nm)/Fe(10nm)/a-C(5nm)/Al(5nm) before and after annealing. This technique is used in order to further characterise the interfaces and provide information about inter-diffusion before and after annealing.Figures 4.19a and 4.19b show also a cross-sectional high resolution TEM image for

the same sample 4.19a before and 4.19b after annealing. Figure 4.19c and 4.19d show the TEM cross section chemical analysis for images of each element in the Fe/RF-sputtered a-C sample before and after annealing. From the graphs, it can be seen that the as-deposited sample before annealing shows clear boundaries between the layers. It is also clear that the RF-sputtered a-C layer has a smooth interface [56, 65]. After annealing (sample annealed at 500 °C), the RF-sputtered a-C layer diffused partly into the metallic layers (Fe and Al). Furthermore, it is likely that the bottom part of the Fe layer remained pristine.

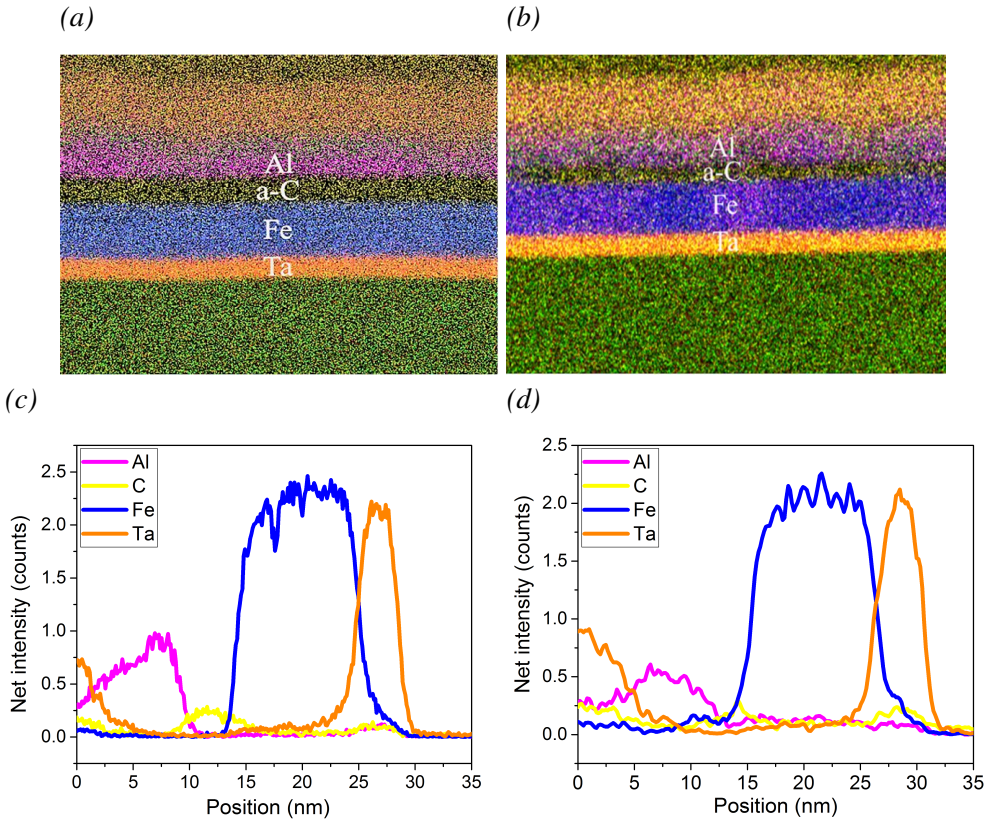

Figure 4.19: Cross-sectional high resolution of Fe/a-C/Al films annealed at 500 °C show the possibility of diffusion of RF-sputtered amorphous carbon before the formation of carbides. Image of Fe(10 nm)/RF-sputtered a-C(20 nm)/Al(5 nm) film (a) as-deposited and (b) annealed at 500 °C show the possibility of inter-diffusion of RF- sputtered a-C in this film after annealing with comparison to as-deposited sample. A line scan data show the composition of the multi-layers (c) before and (d) after annealing using TEM. Annealing will lead to carbon diffusion along the Fe thin film grain boundaries [156, 157].

Figures 4.20a and 4.20b show a cross-sectional high resolution TEM image of Ta(3 nm)/Fe(10 nm)/RF-sputtered a-C(20 nm)/W(5 nm) grown in similar conditions to the samples measured in Figure 4.19. These images show clearly the inter-diffusion of RF-sputtered amorphous carbon in this film after annealing. TEM cross section chemical analysis images (line scans) of the sample before and after annealing are shown in Figures 4.20c and 4.20d. They also show a clear inter-diffusion of RF-sputtered a-C in the system after annealing. Furthermore, the position of RF-sputtered a-C has changed as shown in Figure 4.19b. RF-sputtered a-C also with Fe layers seem to have exchanged places and completely inter-diffuse into each other after annealing as presented in Figure 4.20d.As well as Figures 4.20c and 4.20d show the position of Fe change from (30-40) nm to (14-24) nm.

SQUID-VSM data taken for this sample before and after annealing show typical changes in H_c after annealing, see Figure 4.20e. As expected, inter-diffusion between the Fe and RF-sputtered a-C interfaces after annealing has occurred, which will affect the magnetic properties at the nanocarbon interfaces.

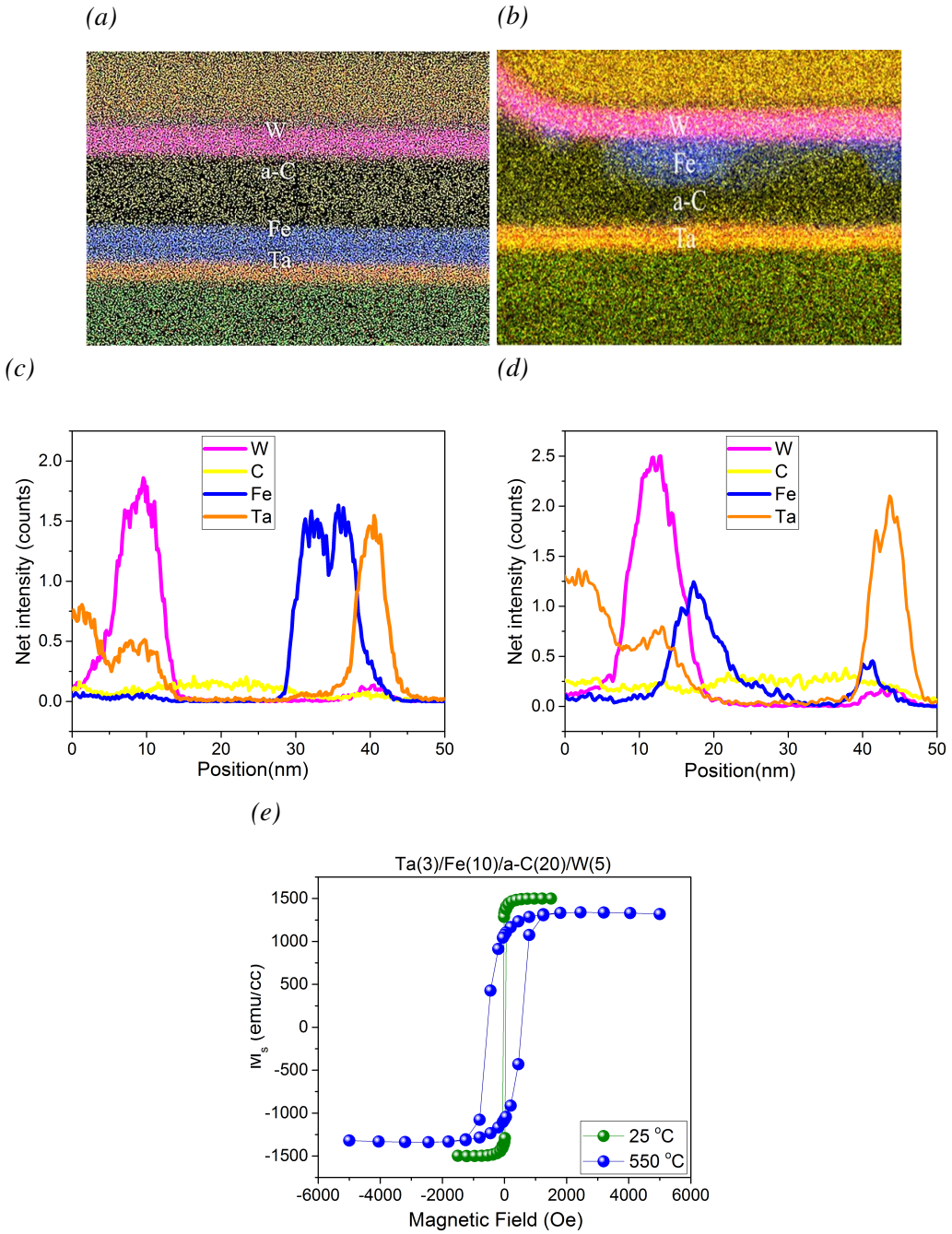

Figure 4.20: Cross-sectional high resolution of TEM images of Ta(3 nm)/Fe(10 nm)/RF-sputtered a-C(20 nm)/W(5 nm) films annealed at 550 °C show the possibility of diffusion of RF- sputtered amorphous carbon before the formation of carbides. The images show the composition of the multilayers (a) before and (b) after annealing using TEM. A line scans of film (c) as-deposited and (d) annealed at 550 °C show the possibility of inter-diffusion of RF- sputtered a-C in this film after annealing. (e) Results from SQUID-VSM confirm changes in H_c for this sample before and after annealing.

4.8 Effect of annealing time on the magnetic properties of Fe/RF-sputtered a-C

Further study has been done to investigate the effect of annealing time on the Fe/RF-sputtered a-C interfaces. For simplicity, bilayer samples of Ta(3 nm)/Fe(t)/RF-sputtered a-C(5 nm)/Al(5 nm) with different thicknesses of Fe were studied to probe the effect of annealing time on the magnetisation and coercivity. The samples were annealed for 10 hours instead of 1 hour and the magnetisation as a function of Fe thickness is shown in Figure 4.21a. The saturation magnetisation of the samples is closer to the bulk value of Fe when the metallic layer is over 15 nm thick. After annealing the sample at 500 - 550 °C for 10 hours, the magnetisation shows the same behaviour as observed for samples annealed for 1 hour, as presented in Figure 4.8.The coercivity in Figure 4.21b exhibits consistent results with the other sets of samples presented in Figure 4.9 where samples annealed for 1 hour and the maximum change in H_c about 600 Oe observed at 10 nm of Fe. This indicates that annealing the Fe/RF-sputtered a-C for a longer time does not change the interfacial coupling, mixing or inter-diffusion in metallic-nanocarbon systems. Control samples were grown without RF-sputtered a-C with the structure Ta(3 nm)/Fe(t)/Al(5 nm), where (t) varied from 10 nm to 30 nm. The magnetometry results show a slight change in M_s of about 20% and in H_c of about 8% after annealing at 550 °C as shown in Figures 4.22a and 4.22b, compared with the samples where RF-sputtered a-C is in direct contact with the metallic layer (Fe), see Figure 4.21. This changes in M_s and H_c of a control sample Ta(3 nm)/Fe(t)/Al(5 nm) after annealing could be explained by an increase of the antiferromagnetic coupling .This happens at the interface between the ferromagnet and antiferromagnet when an antiferromagnetic film is deposited on top of a ferromagnetic film the antiferromagnetic spins at the interface align to the ferromagnetic spins [158].

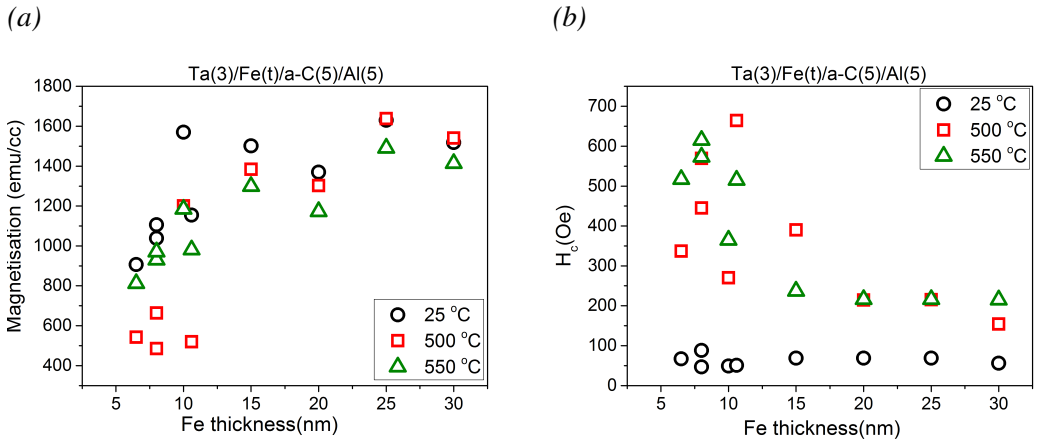

Figure 4.21: Change in (a) magnetisation and (b) coercivity taken from the hysteresis loops measured at room temperature. The sample structure of Ta(3nm)/Fe(t)/RF-sputtered a-C(5 nm)/Al(5 nm), where (t) is varied from 6 to 30 and annealed at different temperatures for 10 h. The thickness of all of the samples is given in nm.

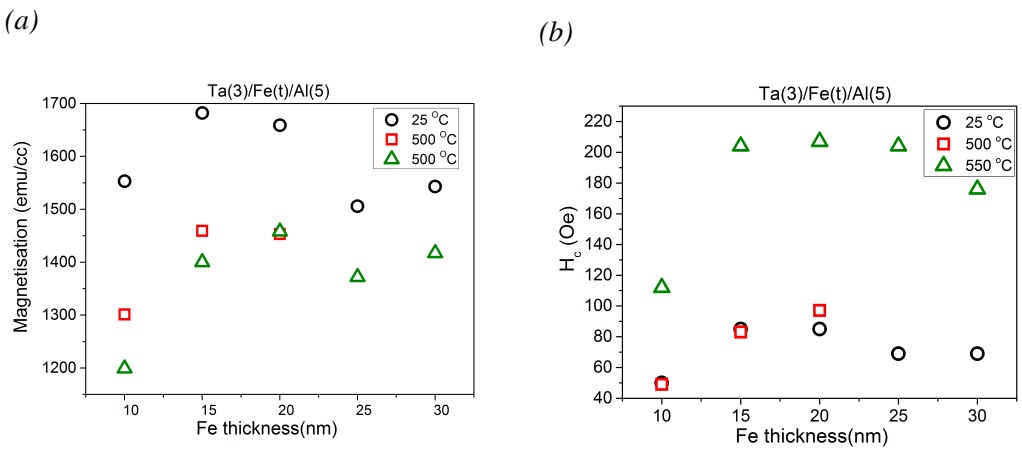

Figure 4.22: The magnetic properties (a) magnetisation and (b) coercivity for control samples of Ta(3 nm)/Fe(t)/Al(5 nm), where 9 nm > (t) > 31 nm. The data show the effect of annealing temperature on the magnetic properties.

4.9 Decoupling the Fe/RF-sputtered a-C interfaces

In order to confirm that the change in the magnetic properties is at least in part, due to hybridisation and charge transfer effects between the nanocarbon and the metal interface, Fe/RF-sputtered a-C samples with a spacer layer of Cu were grown and measured in collaboration with Alistair Walton an undergraduate student under my supervision. The magnetisation and coercivity dependence on the thickness of the Cu spacer in between Fe and RF-sputtered a-C is shown in Figures 4.23a and 4.23b. The spacer layer was introduced to ensure good separation between Fe and RF-sputtered a-C to avoid inter-diffusion after annealing, and the thickness of Cu was varied between 2 nm and 8 nm. The results confirmed a reduction in the magnetic properties at Fe/RF-sputtered a-C interfaces as the thickness of the spacer layer increase. The effect was completely quenched when the Cu thickness reached 8 nm.

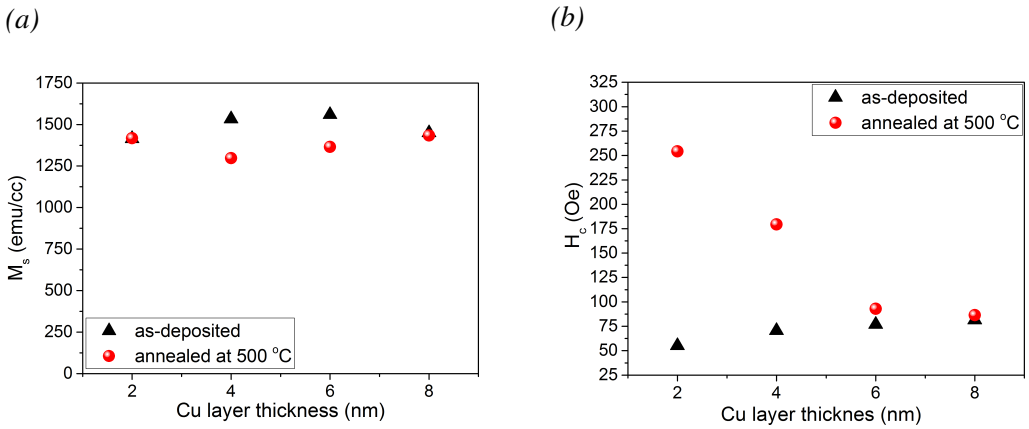

Figure 4.23: Room temperature (a) saturation magnetisation and (b) coercivity as a function of Cu layer thickness for Fe(10 nm)/RF-sputtered a-C(5 nm) capped by 5 nm of Ta and measured before and after annealing at 500 °C . The spacer layer was varied from 2 nm to 8 nm.

4.10 Conclusion

In this chapter, magnetic properties of Fe/RF-sputtered a-C interfaces before and after annealing were studied. The findings highlight the role that hybridisation and charge transfer effects across the interfaces may have on the spin ordering at the interface and/or in the iron film. Before annealing the Fe/RF-sputtered a-C, the results show that the change in magnetisation at room temperature is dependent on the thickness of the metallic layer with a peak when the Fe layer is less than 10 nm as shown in section 4.2. When the Fe layer becomes thick $>$ 10 nm the bulk properties dominate and the interfacial effect between the Fe and RF-sputtered a-C is quenched. The coercivity has also shown thickness dependence when it measured at room temperature where the coercivity reduced compared with control samples without the RF sputtered a-C. This reduction makes the Fe/RF-sputtered a-C softer. RF-sputtered a-C thickness-dependent M_s and H_c measurements tend to indicate that the maximum changes in the magnetic properties between Fe and RF-sputtered a-C take place when the RF-sputtered a-C layer is 5 nm or thicker.

The study also highlighted the effect of annealing in altering the magnetic properties. The significant change has been observed when the annealing temperature reaches above 500 °C where both magnetisation and coercivity has reached maximum change of 1300 emu/cc and 600 Oe respectively, compared with the as-deposited samples. The large change in the coercivity makes the Fe/RF-sputtered a-C harder in comparison to the control samples without RF-sputtered a-C. Decoupling the interface with Cu leads to the prevention of any charge transfer or hybridisation arising at the metal/organic interface.

We then considered the magnetic energy product in the Fe/sputtered a-C system. The results show a maximum magnetic energy product of about 53 kJ/m^3 for 5 nm of RF-sputtered a-C grown on top of a 10 nm thick layer of Fe similar to that of Alnico and ferrites.

Tri-layer samples of Fe/RF-sputtered a-C/Fe system measured at room temperature indicate the possibility that the system can be made softer before annealing with com-

pression to the control sample. However, different thicknesses of RF-sputtered a-C in between 6.5, 10 and 20 nm of Fe exhibited higher values in the coercivity when the RF-sputtered a-C thickness was over 2 nm, and coercivity increases as the RF-sputtered a-C thickness is increased. The saturation magnetisation in this system dropped up to 80% when the temperature was increased. These changes in the M_s and H_c were possibly caused by the inter-diffusion of the carbon after annealing, and production of iron carbide. The inter-diffusion of RF-sputtered a-C in the thin film after annealing has been confirmed using TEM where an amount of graphitisation at the Fe/RF-sputtered a-C interface was revealed.

The results obtained using Raman spectroscopy show changes in the G position and I(D)/I(G) ratio in the Fe/RF-sputtered a-C system were observed after annealing the samples. This enhancement in the Raman spectrum gives evidence that the RF-sputtered a-C layer changes into nanocrystalline graphite and that the orbital hybridisation changes from (20%) sp^3 to (0%) sp^3 [126, 130].

Finally, Kerr microscopy measurements of Fe/RF-sputtered a-C clearly reveal changes in the domain size before and after annealing. The domains observed at the coercive field in Fe with RF-sputtered a-C over-layer become much smaller and with lower contrast once the sample is annealed. This change in the coercivity of the samples and the magnetic images can be explained by the large increase in the density of pinning points when the Fe/RF-sputtered a-C is diffused and crystallised.

In summary, we have tailoring the possibility of tuning the hardness and softness of iron thin films by using nanocarbon. We have achieved coercivties between $\sim$ 10 Oe and 700 Oe without changing thickness or magnetisation for Fe thin films more than 10-50% which is useful in identifying the origin of novel magnetic phenomena in metallic-nanocarbon structures.

CHAPTER 5

Magnetic properties of $Fe_xN_{(1-x)}$/RF-sputtered a-C interfaces

5.1 Introduction

$Fe_xN_{(1-x)}$ thin films may show a variety of magnetic properties, and structures such as $Fe_{16}N_2$ phase present a very high magnetic moment of up to 2.6 μ_B , which is higher than the moment in pure Fe [159–161]. The magnetic properties are very sensitive to the nitrogen concentration, which means that $Fe_xN_{(1-x)}$ with small x will be non-ferromagnetic properties whereas $Fe_xN_{(1-x)}$ with high x are ferromagnetic [162–164]. Recently, $Fe_{16}N_2$ foils have shown high coercivities (H_c) of 1910 Oe, with a BH product about 159 kJ/m^3 at room temperature [50, 155]. Many studies have been done in free-RE permanent magnetic materials searching for low cost, large H_c and high Curie temperatures [50]. This work aims to get free-RE permanent magnetic materials by using nanocarbon. We are trying to increase the magnetic moment and coercivity to maximise BH product while considering as well different hybridisation in $Fe_xN_{(1-x)}$/RF-sputtered amorphous carbon.

In this chapter we investigate the structural and magnetic properties of $Fe_xN_{(1-x)}$ thin films coupled with RF-sputtered a-C. We will also present XRR, SQUID magnetometry and Raman spectroscopy measurements in these films.

5.2 Characterisations of $Fe_xN_{(1-x)}$ thin films

In order to investigate the interfacial effects in $Fe_xN_{(1-x)}$/RF-sputtered a-C, $Fe_xN_{(1-x)}$ thin films were deposited on Si/SiO_2 substrates in a high vacuum where the base pressure in the chamber was approximately 10^{-8} Torr. The $Fe_xN_{(1-x)}$ layer was deposited via DC magnetron sputtering of pure iron target in a fixed argon gas flow rate of 23 SCCM (standard cubic centimetres per minute), while nitrogen gas was introduced into the chamber at different flow rates from 5 to 30%. In order to ensure that $Fe_xN_{(1-x)}$ was deposited and that the layer did result from reactive sputtering, the ratio of nitrogen added to the system was measured against voltage. The thickness of the deposited $Fe_xN_{(1-x)}$ layer and the magnetic properties were measured at the different percentages of N_2 in the mixture of Ar/N_2.

Figure 5.1 shows the voltage across the magnetron measured as function of the pressure and percentage of nitrogen. The results indicate an increase in the voltage with increased nitrogen flow. This provides evidence that the pressure in the system increased and also the Fe target was sputtered normally with increasing N_2 ratio, as opposed to being sputtered reactively.

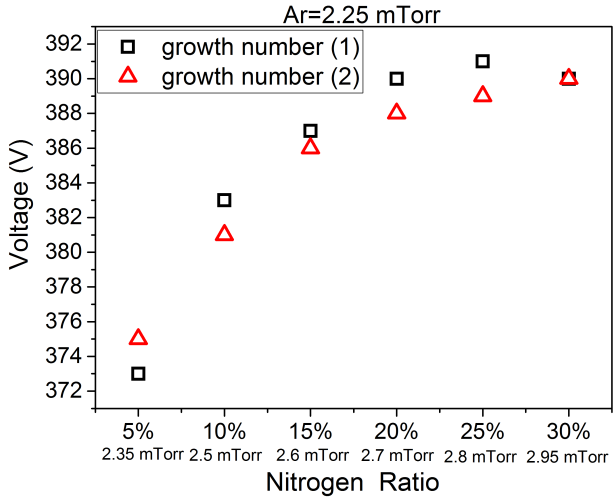

Figure 5.1: The graph illustrates the voltage across the magnetron as a function of the different nitrogen ratio between 5% and 30%. The argon was fixed at 2.25 mTorr and the nitrogen flow varied from 5% to 30%. Here,the growth time was fixed at 100 (s) for all the thin films.

The deposition rates for a range of samples show a decrease in the deposition rate with increasing N_2/Ar ratio as shown in Figure 5.2. This could suggest that the particle pressure of the N_2 flow increased and affected the deposition rates. This change in the deposition rate could be corresponding to the sputter yield and/or the density of Fe. The sputter yield drops with rising the nitrogen partial pressure owing to the high dissociation energy of nitrogen [162].

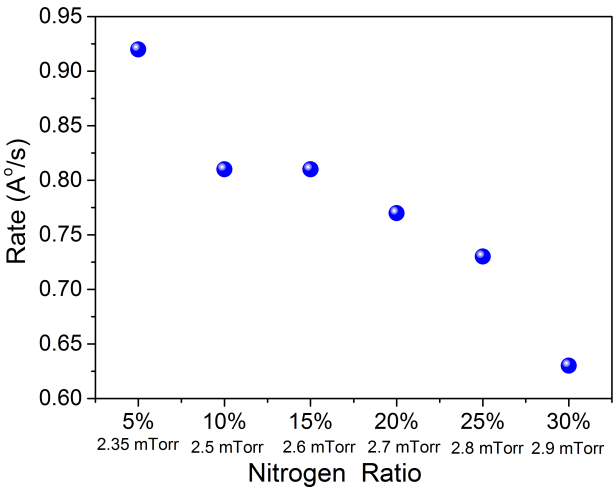

Figure 5.2: Dependence of the rate of Si/SiO_2/$Fe_xN_{(1-x)}$ thin films on the nitrogen ratio, where the nitrogen was varied from 5% to 30%. The data shows that increasing the N_2 flow lead to drop the deposition rates.

Figure 5.3 shows the low angle XRR of un-annealed and annealed samples. The XRR measurements indicate that 10 nm of $Fe_xN_{(1-x)}$ grown at 15% N_2 ratio have less diffusion after annealing at 500 °C for one hour in a vacuum of about 10^{-5} Torr as presented in Figure 5.3a. However, $Fe_xN_{(1-x)}$ samples of 10 nm thickness grown at 10% N_2 ratio show changes in the critical angle as shown in Figure 5.3b that give signs of Fe diffusion after annealing. The deposited $Fe_xN_{(1-x)}$ films have also annealed at 500 °C and the roughness has been compared to the as-deposited films. The XRR reflectivity data of $Fe_xN_{(1-x)}$ thin film with 10% of N_2 ratio fitted with Bede software and showed an increase in roughness after annealing at 500 °C, as shown in Figure 5.3c. This may due to crystalline the thin films after annealing. Figure 5.3d shows the XRD scan for Si/SiO_2/$Fe_xN_{(1-x)}$ (100 nm) grown at 10% nitrogen and there is a peak observed at 2θ = 43.2° which could be corresponded to Fe_2N [165].

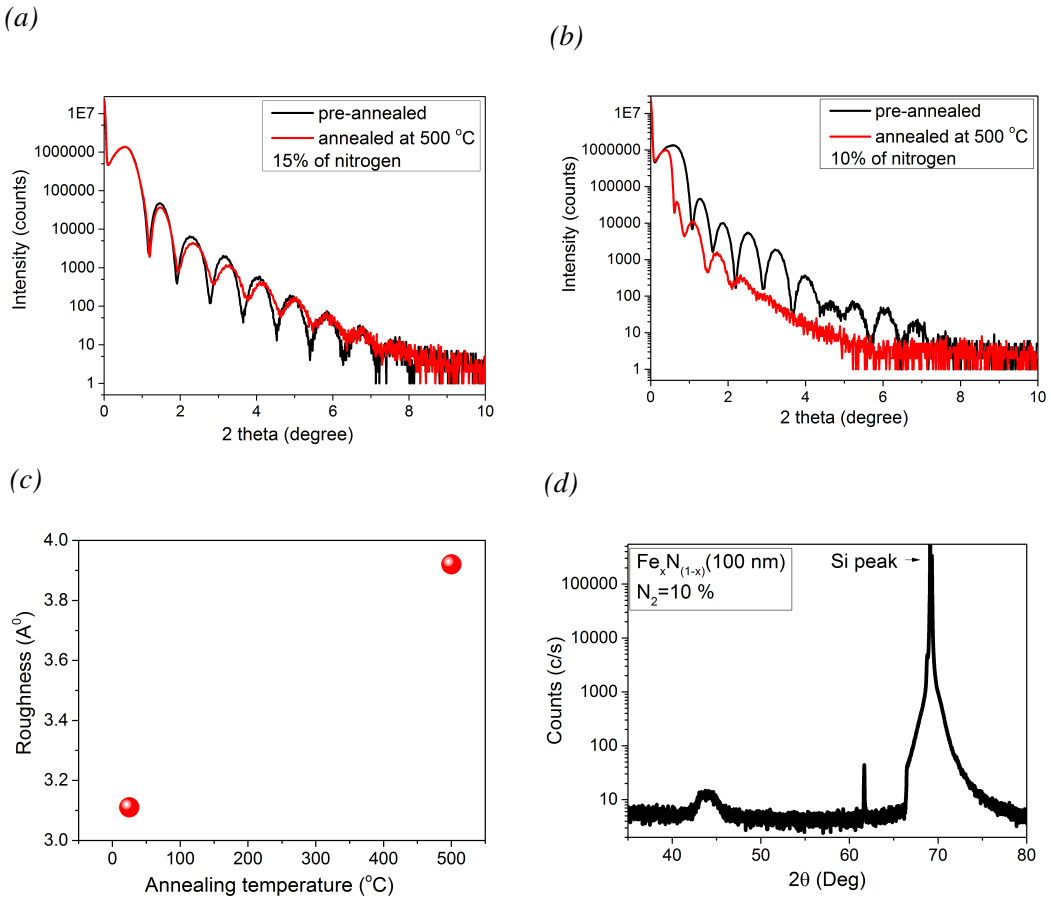

Figure 5.3: X-ray reflectivity measurements for $Si/SiO_2/Fe_xN_{(1-x)}$(10 nm) grown at different nitrogen ratios: (a) 15% (b) 10%. The XRR data was taken for as-deposited samples and annealed samples at 500 °C. The nitrogen ratio of 10% and 15% are equivalent to thickness of 10 nm for both samples. (c) The roughness of $Si/SiO_2/Fe_xN_{(1-x)}$(10nm) grown at 10% nitrogen ratio as a function of annealing temperature was obtained using Bede fitting software. (d) X-ray diffraction for $Si/SiO_2/Fe_xN_{(1-x)}$ (100 nm) grown at 10% nitrogen show a peak at $2\theta = 43.2°$ that may be corresponded to Fe_2N [165].

5.3 Magnetometry of $Fe_xN_{(1-x)}$ thin film

The magnetic properties of the deposited $Fe_xN_{(1-x)}$ films have been characterised using SQUID magnetometry before and after annealing. Figures 5.4 and 5.5 show the magnetisation and coercivity as a function of the N_2 ratio, where the $Fe_xN_{(1-x)}$ thickness was varied from 7 nm to 11 nm (Figure 5.4) and from 24 nm to 39 nm (Figure 5.5). For as-deposited thin films, the magnetisation curve shows a decrease in the M_s as the N_2 to Ar ratio increases. The same behaviour was observed when the films were annealed at 250 °C. However, annealing the films at 500 °C showed a slight increase in M_s from 350 emu/cc to 600 emu/cc with nitrogen content. The coercivity in the as-deposited film was very close to that of pure Fe films. However, H_c increased from $\sim$ 50 to 400 Oe after the samples were annealed at 500 °C, which is higher than a literature value (200 Oe) for annealed FeN, and smaller than the value observed in $Fe_{16}N_2$ [60, 155]. These changes in M_s and H_c after annealing could be due to the percentage of nitrogen atoms around the Fe atoms. As a result, the hybridisation is quenched with increasing the nitrogen concentration [162].

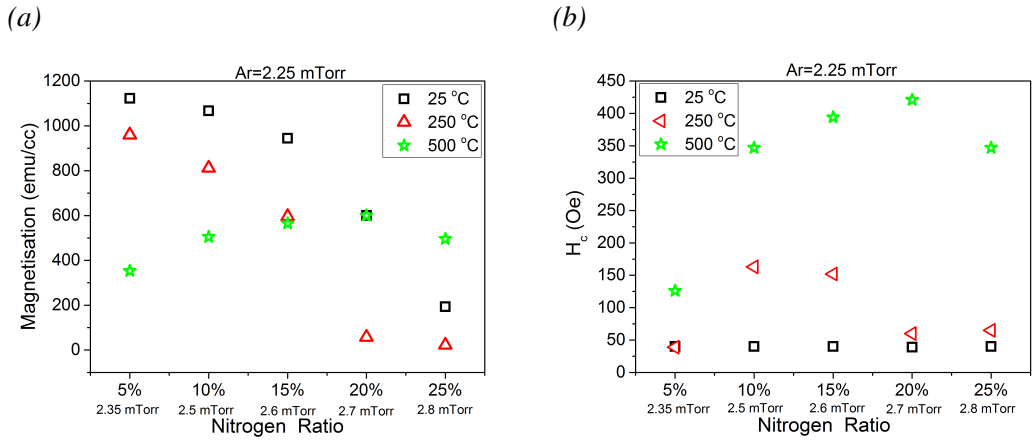

Figure 5.4: Room temperature(a) magnetisation and (b) coercivity as a function of nitrogen ratio measured after annealing $Si/SiO_2/Fe_xN_{(1-x)}(t)$ thin films at different temperatures. The thickness of the $Fe_xN_{(1-x)}$ samples was 9±2 nm.

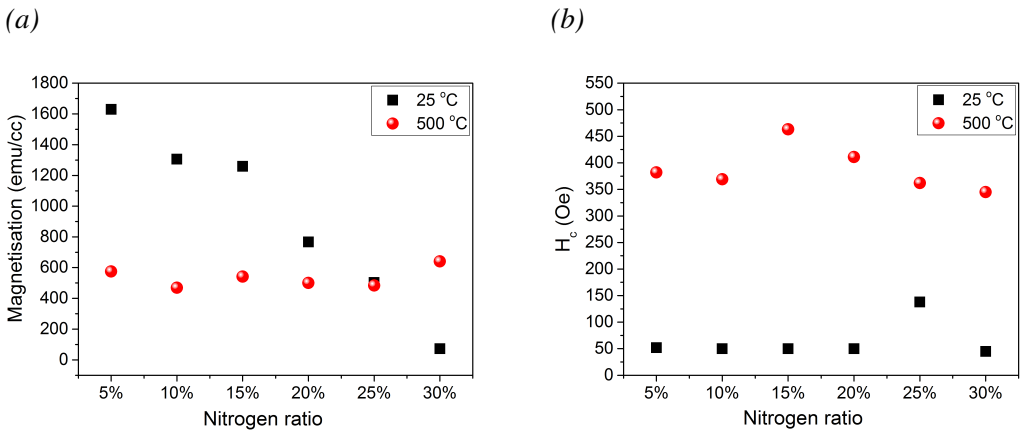

Figure 5.5: Room temperature magnetometry measurement of $Fe_xN_{(1-x)}$ thin films (a) magnetisation (b) coercivity measured as deposited and annealed at 500 °C. With the sample structure of $Si/SiO_2/Fe_xN_{(1-x)}(t)$, all the $Fe_xN_{(1-x)}$ thin films here in the range 23-40 nm thick.

5.4 Magnetometry of Ferromagnetic/RF-sputtered a-C bilayers

In this chapter, we are interested in whether the introduction of nitrogen creates changes at $Fe_xN_{(1-x)}$/RF-sputtered a-C interfaces and whether it has any significant effect on the magnetic properties.

In this work first, the $Fe_xN_{(1-x)}$ films were deposited using DC magnetron sputtering of pure iron at a fixed argon gas flow and different concentrations of nitrogen gas. After depositing the $Fe_xN_{(1-x)}$ films, RF-sputtered a-C was grown on top. The samples have a typical structure of Ta(3 nm)/$Fe_xN_{(1-x)}$ (11 nm)/RF-sputtered a-C(5 nm)/Al(5 nm), where the $Fe_xN_{(1-x)}$ layer was grown at different N_2 ratios, as shown in Figure 5.6. M_s showed no significant change when the samples were annealed to 500 °C, but further annealing to 550 °C causes a 83% drop in M_s. This could be due to the introduction of nitrogen to the Fe, for our thin films that might be contribute to preform a $Fe_xN_{(1-x)}$ phase with lower saturation magnetisation and an increase in H_c [106]. The magnetic measurements of $Fe_xN_{(1-x)}$ (11 nm, 10% nitrogen ratio) coupled with 5 nm of RF-sputtered a-C exhibited a maximum change in the H_c from 50 Oe for as-deposited samples to 150±20 Oe after annealing at 500 °C when the N_2 fraction is 10%, after annealing at 550 °C, H_c was 90±20 Oe.

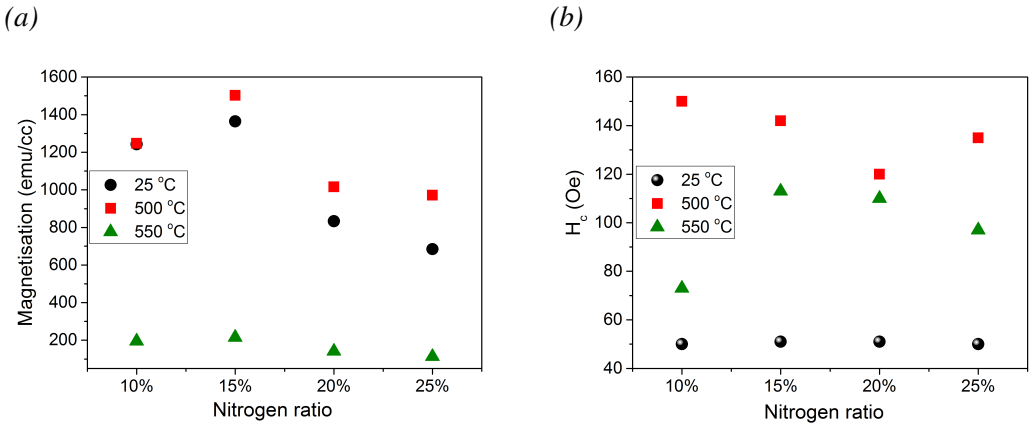

Figure 5.6: (a) M_s and (b) H_c measurements as a function of different N_2 ratios measured by SQUID before (25 °C) and after annealing at different temperatures: 500 and 550 °C. The sample structure is Ta(3nm)/ $Fe_xN_{(1-x)}$ (11 nm)/RF-sputtered a-C(5 nm)/Al(5 nm) grown on silicon oxide substrates.

5.4.1 Room temperature magnetic behaviour

The samples studied are thin films of Ta(3 nm)/$Fe_xN_{(1-x)}$(t)/RF-sputtered a-C(5 nm)/ Al(5 nm), where the thickness of the $Fe_xN_{(1-x)}$ layer was varied between 2 nm and 11 nm. The samples were grown in a mixture of Ar/N_2, at 10% and 15% flow rates of N_2. The percentages of N_2 (10% and 15%) have chosen due to a good magnetic properties as seen in Figure 5.6.

Figure 5.7 shows the differences in the magnetisation of these films. The saturation magnetisation $\sim$ 1200 emu/cc is slightly lower than for pure Fe [151]. The saturation magnetisation changes only slightly when the $Fe_xN_{(1-x)}$ thickness and the N_2 flow rate are varied, and the effect of nitrogen on the magnetisation of the $Fe_xN_{(1-x)}$ thin films was found to be consistent with previous studies [166]. The M_s values increase as the N_2 flow is decreased in many previous studies which N_2 has an effect on the saturation magnetisation of Fe [151]. Figure 5.8 shows changes in the coercivity compared with control samples. The results indicate very small changes in the coercivity, even when the percentage of N_2 is varied. Nitrogen contents in the system appear to prevent the hybridisation between Fe and RF-sputtered a-C and we do not observe the systematic reduction in H_c that we measured for pure Fe/RF-sputtered a-C (see section 4.2.1). However, there is still a reduction in M_s with RF-sputtered a-C , at least for

15% N_2, that is similar to that seen in pure Fe/RF-sputtered a-C which suggest that there is still an interfacial coupling between $Fe_xN_{(1-x)}$ and RF-sputtered a-C , even though the anisotropy is not changed as drastically as for pure Fe. The coercivity for samples grown at 10% and 15% of N_2 was 50 Oe which is lower than of some previously measured $Fe_xN_{(1-x)}$ thin films [60][167].

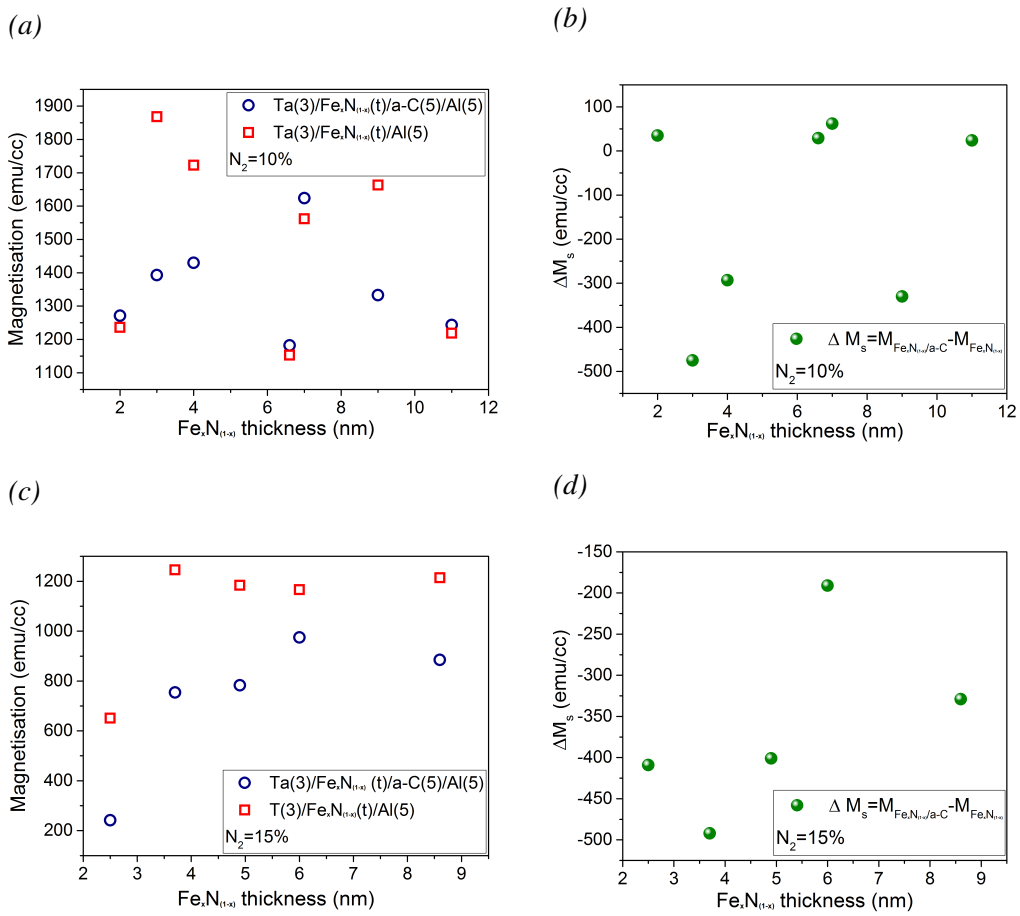

Figure 5.7: (a) Magnetisation and (b) differences in magnetisation ΔM_s as a function of iron nitride films with various thicknesses grown at 10% of N_2 . (c) M_s and (d) ΔM_s for samples grown at 15% of N_2. The sample structure is Ta(3nm)/$Fe_xN_{(1-x)}$(t)/a-C(5nm)/Al(5nm), compared with control samples of Ta(3 nm)/$Fe_xN_{(1-x)}$(t)/Al(5nm), where (t) is varying $Fe_xN_{(1-x)}$ thickness from 2 to 11 nm measured at 300 K. The error bars are smaller than the data points.

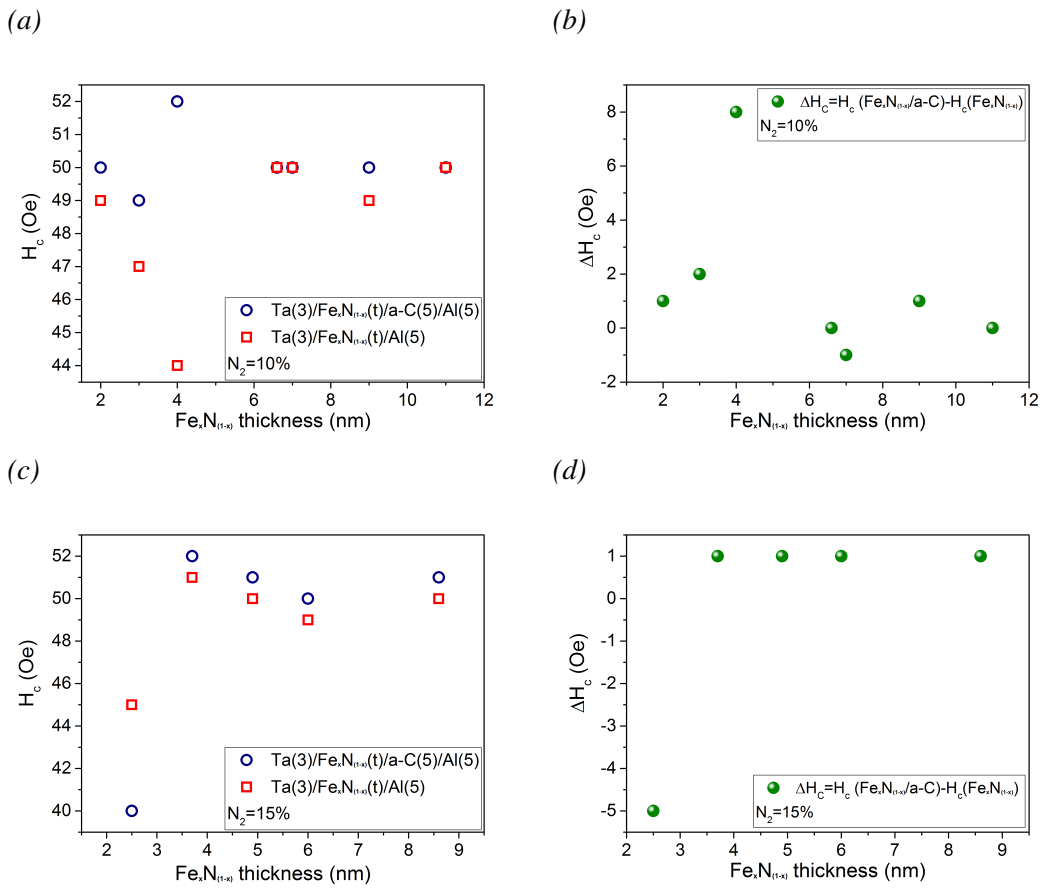

Figure 5.8: Coercivity of $Fe_xN_{(1-x)}$/RF-sputtered a-C and $Fe_xN_{(1-x)}$ thin films as a function of thicknesses grown at different Ar/N_2 ratios. (a) H_c and (b) H_c for samples grown at 10% of N_2, (c) H_c and (d) H_c for samples grown at 15% of N_2 . All the data was extracted from hysteresis M(H) loops measured at room temperature. H_c represents the change in H_c between the pure $Fe_xN_{(1-x)}$ samples and the $Fe_xN_{(1-x)}$ samples with RF-sputtered a-C samples.

5.4.2 Effects of annealing on the saturation magnetisation (M_s)

The $Fe_xN_{(1-x)}$/RF-sputtered a-C samples grown at 10% and 15% N_2 ratios were annealed for one hour at 10^{-5} Torr, at temperatures of 500 °C, 550 °C and 600 °C. Figures 5.9a and 5.9b show the M_s measurements as a function of $Fe_xN_{(1-x)}$ thicknesses. It can be seen that the M_s decreased up to 80% as the annealing temperature was increased. Figure 5.9 also show that M_s is enhanced with increasing the $Fe_xN_{(1-x)}$ thickness for both systems $Fe_xN_{(1-x)}$/RF-sputtered a-C and $Fe_xN_{(1-x)}$. This enhancement starts for

thickness above 3 nm. This could be result of increasing Fe content in the films [167]. The as-deposited control samples exhibit a M_s value close to the bulk value of Fe. This could have been caused by specific formation of a $Fe_xN_{(1-x)}$ phase where $Fe_xN_{(1-x)}$ with small x will be non-ferromagnetic properties whereas $Fe_xN_{(1-x)}$ with high x are ferromagnetic [162–164]. The reduction in M_s after annealing up to 550 °C when it is coupled with the nanocarbon interface could indicate the effect of the hybrid interface and the charge transfer in the $Fe_xN_{(1-x)}$/RF-sputtered a-C system.

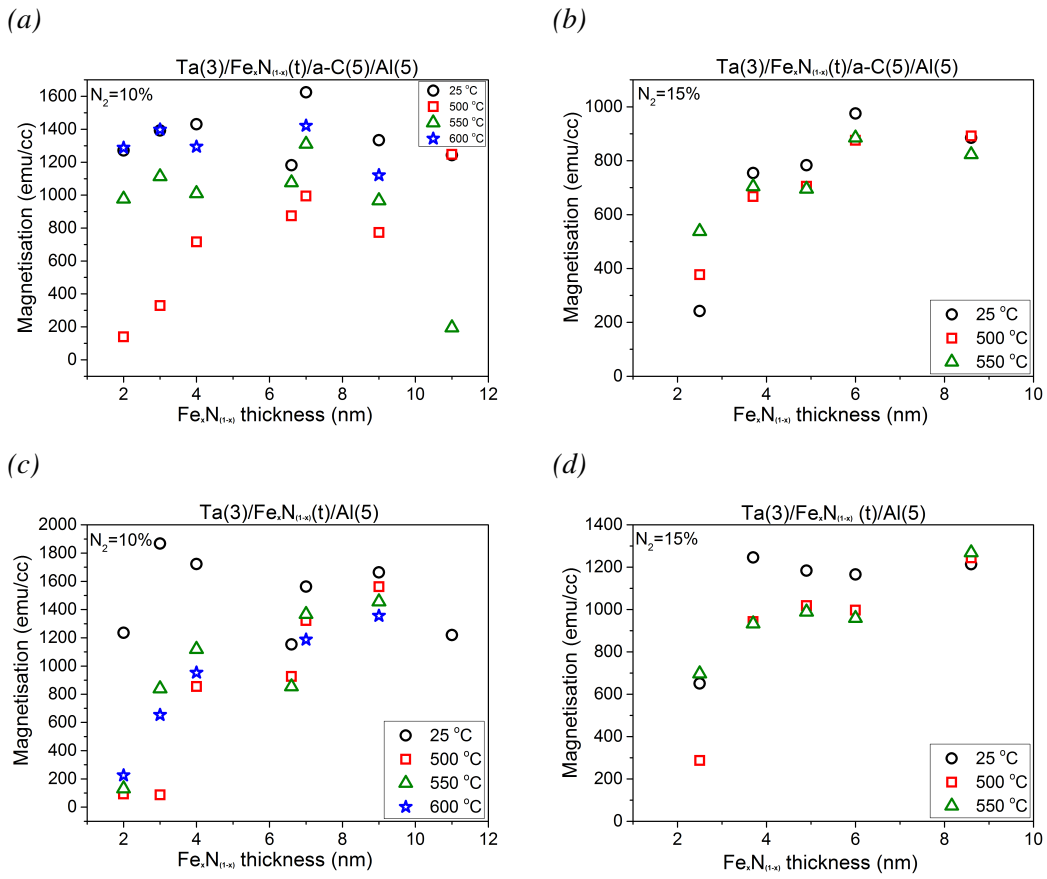

Figure 5.9: Magnetisation as a function of thickness of the $Fe_xN_{(1-x)}$ measured at 300 K for the thin films $Fe_xN_{(1-x)}$/RF-sputtered a-C grown at (a) 10% nitrogen fraction and (b) 15% nitrogen fraction and annealed at temperatures between 500 °C and 600 °C (c) M_s for the control samples of Ta(3 nm)/$Fe_xN_{(1-x)}$(t)/Al(5 nm) as a function of various $Fe_xN_{(1-x)}$ thicknesses measured at room temperature grown at N_2 fractions of 10% and (d)15%.

5.4.3 Annealing effects on the coercivity (H_c)

The coercivity as a function of $Fe_xN_{(1-x)}$ thickness was measured after annealing for the samples used in section 5.4.2. at 10% fraction of N_2. Figure 5.10a shows that the coercivity increased to 550 Oe in $Fe_xN_{(1-x)}$/ RF-sputtered a-C at 500 °C, and slightly decreased when the annealing temperature was increased to 550 °C, which is similar to the results observed in Fe/RF-sputtered a-C systems (see Section 4.3.1.2). When the N_2 fraction is equal to 15%, H_c showed a gradual increase from 50 Oe to 350 Oe when the $Fe_xN_{(1-x)}$ layer becomes thicker and annealed to higher temperatures, as shown in Figure 5.10b. Similar behaviour is observed for $Fe_xN_{(1-x)}$ layers where the change in H_c after annealing is about 100 Oe, see Figures 5.10c and 5.10d. The change in H_c for both $Fe_xN_{(1-x)}$/RF-sputtered a-C and $Fe_xN_{(1-x)}$ samples when they are annealed could give an indication of the effect of nitrogen content on the magnetic properties that could be quench the hybridisation, also the crystallinity of the $Fe_xN_{(1-x)}$ before and after annealing may also contribute to explaining the changes in H_c. The results indicate the formation of inter-diffusion which takes place during annealing the thin films and that depends on the N_2 fraction. The film with 15% N_2 exhibited less diffusion, whereas at 10% N_2 , diffusion was clearly present in the system. Interestingly, the change in the H_c with the RF-sputtered a-C is significant compared to the control samples especially with 15% N_2 ratio which could be due to the charge transfer that occurs at the $Fe_xN_{(1-x)}$/RF-sputtered a-C interface.

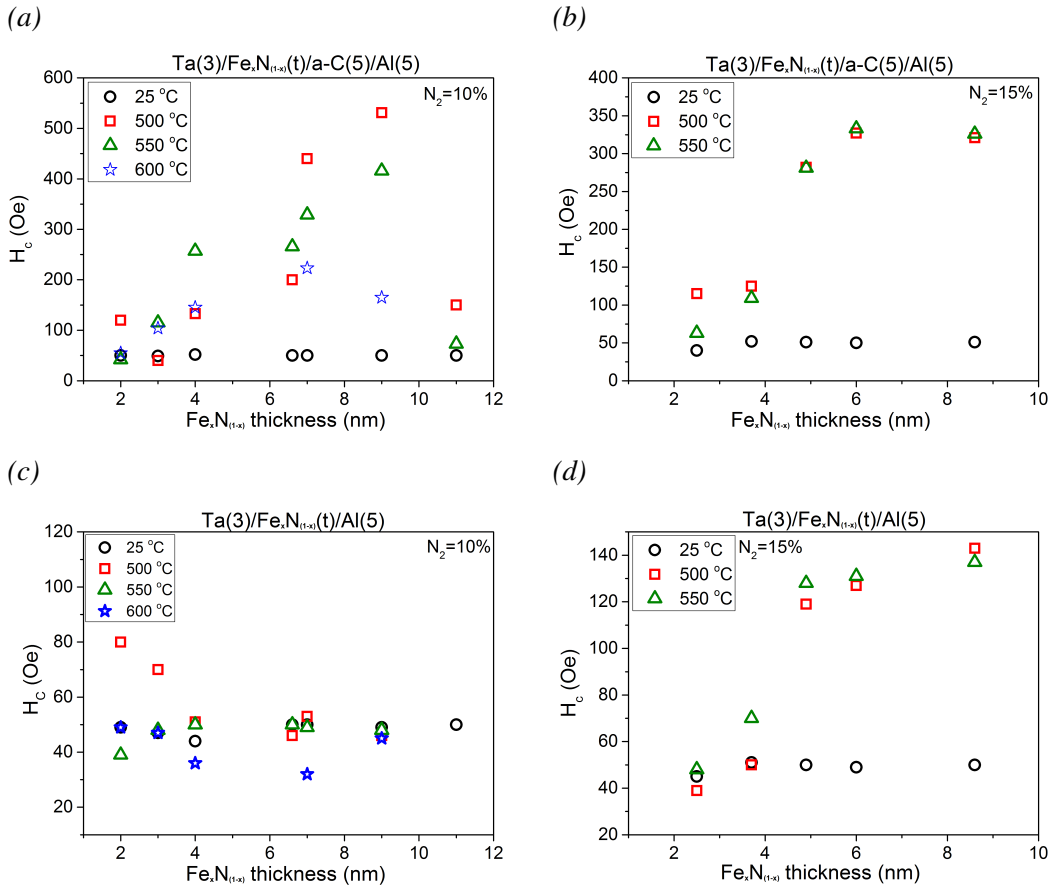

Figure 5.10: Changes in coercivity as a function of $Fe_xN_{(1-x)}$ thickness at 300 K for thin films of Ta(3 nm)/$Fe_xN_{(1-x)}$(t)/RF-sputtered a-C(5 nm)/Al(5 nm) grown at (a) 10% fraction of nitrogen and (b) 15% nitrogen, and annealed at 500 to 600 °C. (c) H_c for the control samples of Ta(3 nm)/$Fe_xN_{(1-x)}$(t)/Al(5 nm) as a function of various $Fe_xN_{(1-x)}$ thicknesses measured at room temperature grown at 10% N_2 and (d) 15% N_2.This data showed the interfacial effect of $Fe_xN_{(1-x)}$/RF-sputtered a-C(5 nm) on the H_c before and after annealing.

Figure 5.11 presents the X-ray reflectivity (XRR) spectra for two samples of $Fe_xN_{(1-x)}$(5)/RF-sputtered a-C(5 nm)/Al(5 nm) and $Fe_xN_{(1-x)}$(5)/Al(5 nm) before and after annealing at 500 °C. These data show clearly the inter-diffusion of RF-sputtered a-C into iron nitride (Figure 5.11a) compared with a control sample as shown in Figure 5.11b.

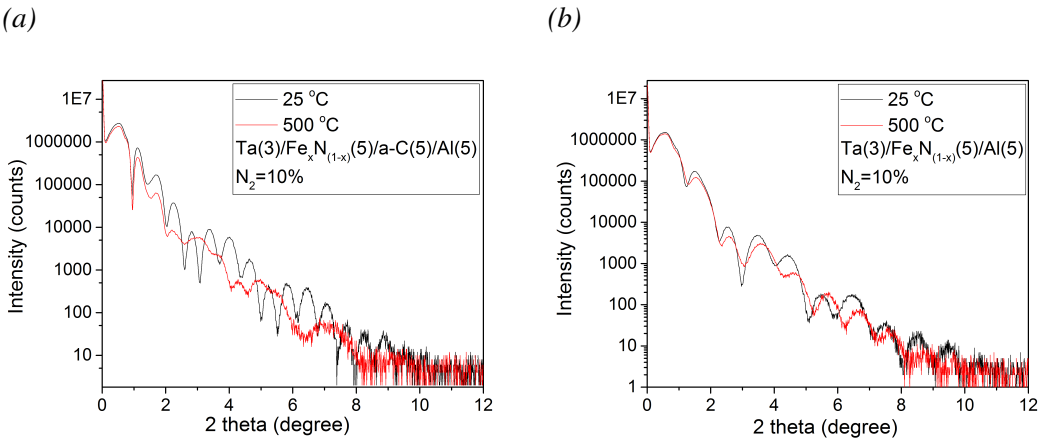

Figure 5.11: X-ray reflectivity of a typical film (b) $Si/SiO_2/Ta(3\ nm)/Fe_xN_{(1-x)}(5)$/RF-sputtered a-C(5 nm)/Al(5 nm) and (b) $Si/SiO_2/Ta(3\ nm)/Fe_xN_{(1-x)}(5)$/Al(5 nm) before and after annealing. The samples grown at 10% of N_2. The samples were annealed at 500 °C for one hour in a vacuum about 10^{-5} Torr.

Figure 5.10a shows that the H_c reaches the maximum when the $Fe_xN_{(1-x)}$ layer is 7 nm - 9 nm. Based on this result, Figure 5.12 shows the coercivity and the saturation magnetisation for layers with this thickness range as a function of annealing temperature for $Fe_xN_{(1-x)}$ coupled with RF-sputtered a-C (Figures 5.12a and 5.12c) and $Fe_xN_{(1-x)}$ as a control (Figure 5.12b). The samples were grown in a 10% fraction of N_2. It is clear that H_c peaks when the annealing temperature is 500 °C, and then drops at higher temperature. From Figure 5.12c, it can be seen that M_s decreases as the annealing temperature was increased. So the most effective annealing temperatures in the $Fe_xN_{(1-x)}$/RF-sputtered a-C system are between 500 °C and 550 °C. These results are probably due to the nitrogen concentration can affect the motion of the magnetic domain and leads to increase coercivity and decrease M_s [168]. On the other hand, the H_c for control samples present approximately no change for both sample thicknesses

at different annealing temperatures as shown in Figures 5.12b. Therefore, the growth of $Fe_xN_{(1-x)}$ is very important due to the nitrogen pressure that can affect the magnetic properties [162] in our $Fe_xN_{(1-x)}$/RF-sputtered a-C thin films. The thickness of the metallic layer may be not accurate that could be due to growth condition such as substrate alignment or deposition pressure and variations in volume.

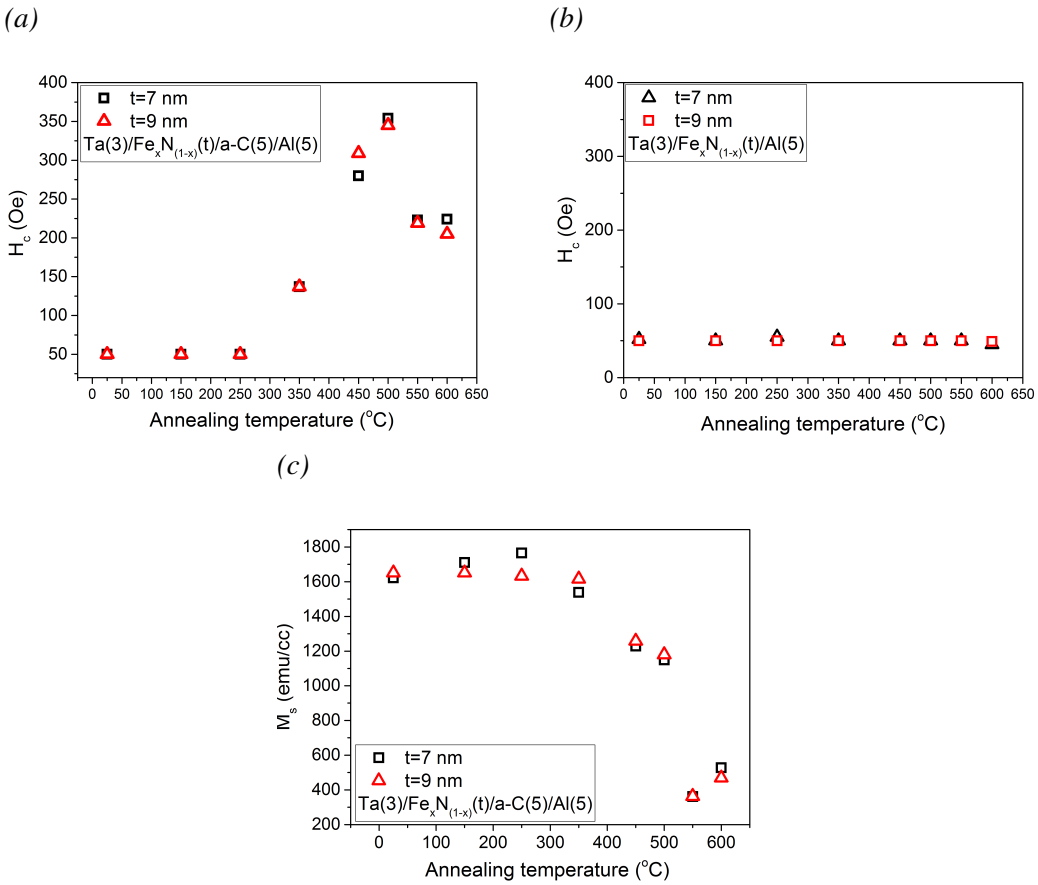

Figure 5.12: Dependence of (a-b) coercivity and (c) the saturation magnetisation on the annealing temperatures.(a-c) the sample grown at 10% of N_2 with structure of $Si/SiO_2/Ta(3\ nm)/Fe_xN_{(1-x)}(t)$/RF-sputtered a-C(5 nm)/Al(5 nm) and (b) $Si/SiO_2/Ta(3\ nm)/Fe_xN_{(1-x)}(t)/Al(5\ nm)$, where (t) are 7 nm and 9 nm. The samples were annealed from 150 °C to 600 °C for one hour in a vacuum about 10^{-5} Torr.

5.5 Magnetic energy product $(BH)_{max}$ in the $Fe_xN_{(1-x)}$/RF-sputtered amorphous carbon system

Figure 5.13 shows the BH_{max} energy product as a function of $Fe_xN_{(1-x)}$ thickness grown with a 10% fraction of N_2. The maximum value of BH_{max} was observed for 9 nm of $Fe_xN_{(1-x)}$ and 5 nm of RF-sputtered a-C at about 9 kJ/m^3 after it was annealed at 500 °C. This could be due to the nitrogen content in the $Fe_xN_{(1-x)}$/RF-sputtered a-C thin films can be reasonable for affecting the magnetic moment in this system [169]. However, the possibility of increasing the $(BH)_{max}$ value to 53 kJ/m^3 was shown in Fe/RF-sputtered a-C which was annealed at 500 °C. In Section 2.7 the calculation of BH_{max} has been discussed.

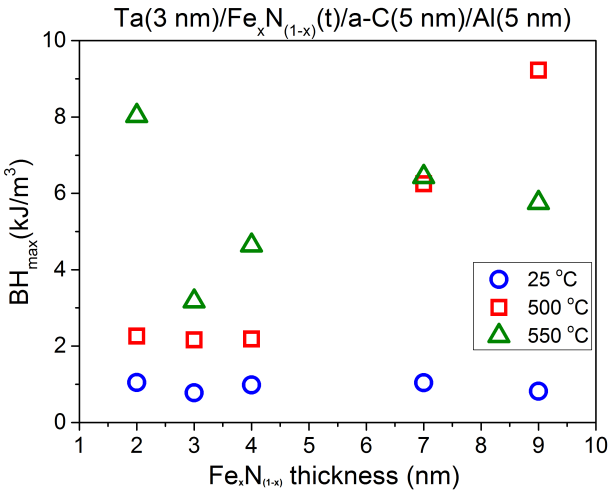

Figure 5.13: The dependence of $(BH)_{max}$ product as a function of $Fe_xN_{(1-x)}$ thickness for Ta (3 nm)/$Fe_xN_{(1-x)}$(t)/RF-sputtered a-C(5 nm)/Al(5 nm) grown with a 10% fraction of N_2, where (t) ranges from 2 nm to 9 nm. In order to calculate the $(BH)_{max}$ product, all the samples were measured at room temperature, both as-deposited and after annealing at 500 °C and 550 °C.

5.6 Raman spectra of $Fe_xN_{(1-x)}$/RF-sputtered amorphous carbon after annealing

In order to observe the hybridisation effect on $Fe_xN_{(1-x)}$/RF-sputtered a-C systems, Raman spectroscopy was used. Samples presented in Figure 5.6, the Raman spectra for these samples show a shift in G position to higher frequencies and an increase in the I(D)/I(G) ratio with higher annealing temperatures as a function of N_2 fractions from 10% to 25% as shown in Figure 5.14. This points to the appearance of nanocrystalline graphite carbon after annealing. The data also shows lower I(D)/I(G) ratio and G position at 25% of N_2 that might be caused by the addition amount of nitrogen N_x [170].

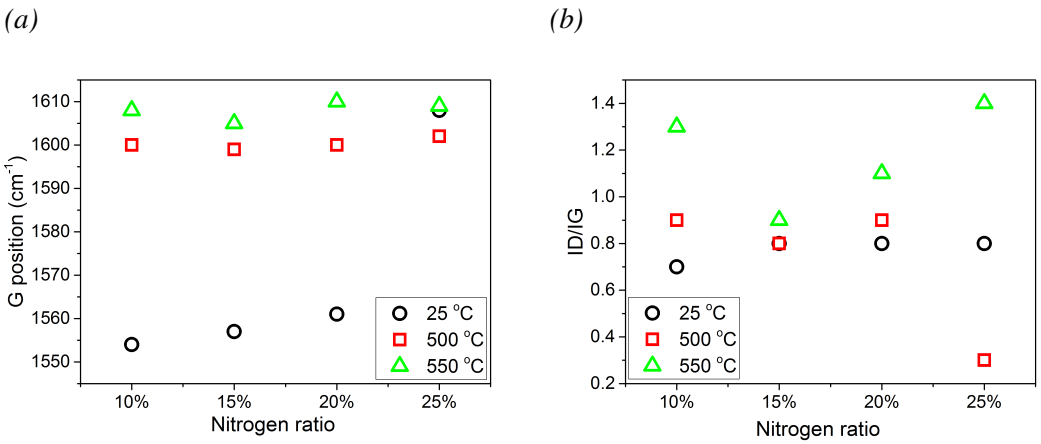

Figure 5.14: Raman spectra measurements for Ta(3nm)/$Fe_xN_{(1-x)}$(11nm)/RF-sputtered a-C(5nm)/Al(5nm), showing (a) G peak position and (b) I(D)/I(G) ratio as a function of different N_2 ratios. The data are from as-deposited samples, and samples post-annealed at 500 °C and 550 °C.

5.6 Raman spectra of $Fe_xN_{(1-x)}$/RF-sputtered amorphous carbon after annealing

We were able to classify the type of carbon through the sp^3 and sp^2 bonds before and after annealing using Raman spectroscopy to try and correlate the results with changes in both M_s and H_c of the studied samples with N_2 fractions of 10% and 15%.

Figure 5.15 displays the G peak position extracted from the Raman spectra as a function of $Fe_xN_{(1-x)}$ thickness for samples measured in section 5.4.2 and 5.4.3. The results reveal shifts to higher frequencies after annealing, indicating that the sp^2 clusters became large enough to allow observation of nanocrystalline graphite structures. Raman spectra for Fe/RF-sputtered a-C thin films have shown the same trend that we observe in $Fe_xN_{(1-x)}$/RF-sputtered a-C thin films.

The I(D)/I(G) ratio is presented as a function of $Fe_xN_{(1-x)}$ thickness before and after annealing in Figure 5.16. There is an increase in the I(D)/I(G) ratio after annealing due to the conversion of sp^3 bonds to sp^2 bonds. We have seen annealing sp^3 orbitals into sp^2 orbitals leads to change the magnetic properties [58]. This confirms the changes in the M_s and H_c due to the crystalline carbon layer which is altering the orbital states leads to the bonding changes which cause unbalance in the charge transfer hence altering the magnetic properties.

5.6 Raman spectra of $Fe_xN_{(1-x)}$/RF-sputtered amorphous carbon after annealing

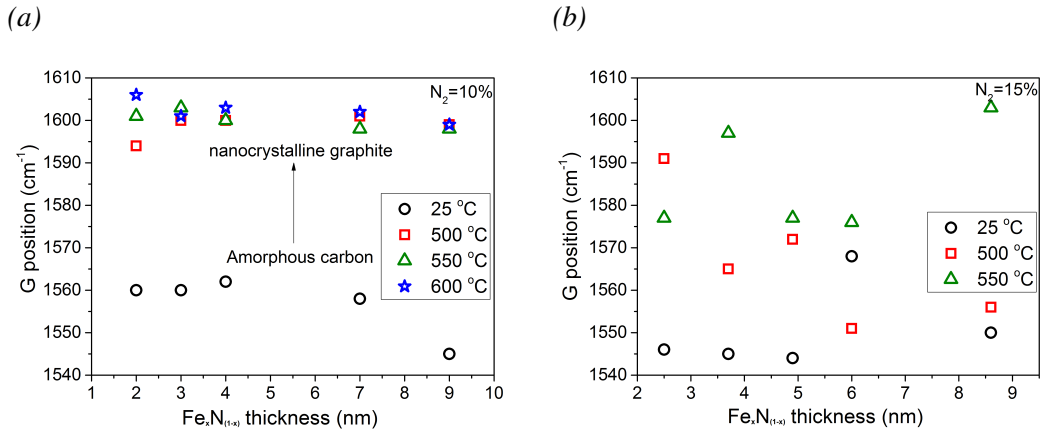

Figure 5.15: G position as a function of $Fe_xN_{(1-x)}$ thickness for samples of Ta(3 nm)/ $Fe_xN_{(1-x)}$(t)/RF-sputtered a-C(5 nm)/Al(5nm), where (t) is varied from 2 nm to 9 nm. The samples were deposited at (a) 10% fraction of nitrogen and (b) 15% fraction of nitrogen. Here, as the temperature increases, the G peak moves from ∼ 1545 to 1600 cm^{-1}. All the data were extracted from Raman spectra for as-deposited and annealed samples.

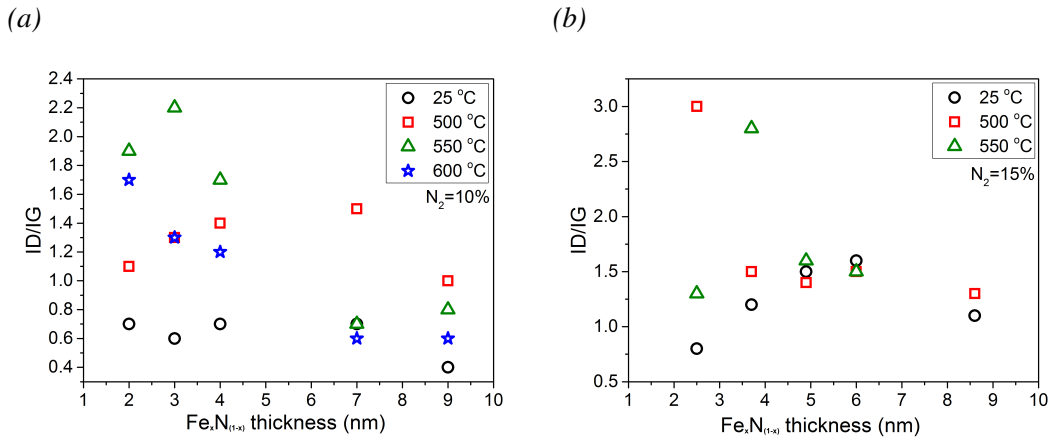

Figure 5.16: I(D)/I(G) is plotted against $Fe_xN_{(1-x)}$ thickness for samples of Ta(3 nm)/ $Fe_xN_{(1-x)}$(t)/RF-sputtered a-C(5 nm)/Al(5nm), where (t) ranges from 2 nm to 9 nm. The samples were deposited at (a) 10% fraction of N_2 and (b) 15% fraction of N_2. An increase of I(D)/I(G) was observed between 0.5 and 3 after annealing. All the data were extracted from Raman spectra for as-deposited and annealed samples.

5.7 Conclusion

In this chapter, the magnetic properties of $Fe_xN_{(1-x)}$ samples with and without RF-sputtered a-C were studied. $Fe_xN_{(1-x)}$ films have been grown with a fixed argon flow but with varies N_2 ratios. The films were annealed over a wide temperature range to investigate the changes in the magnetic properties.
The results obtained using XRR emphasise the impact of annealing the $Fe_xN_{(1-x)}$ where the crystallinity can be improved after annealing [60]. Samples with 15% of N_2 ratio showed less diffusion compared to the samples with 10% N_2 ratio. The data obtained using SQUID shows the effect of N_2 fraction on the magnetic properties of the thin films.

$Fe_xN_{(1-x)}$/RF-sputtered a-C thin films measured at room temperature illustrate small changes in M_s and H_c when compared to the Fe/RF-sputtered a-C system discussed in Chapter 4. In the case of Fe/RF-sputtered a-C system, the change in the magnetic properties is due to hybridisation effect between the carbon and 3d metal bands in Fe at the interfaces, so as-deposited samples show no inter-diffusion which is approved by TEM. Whereas, the hybridisation effect is not presented in $Fe_xN_{(1-x)}$/RF-sputtered a-C because it is quenched with nitrogen.
The $Fe_xN_{(1-x)}$/RF-sputtered a-C thin films grown at 10% and 15% fractions of N_2 rise in coercivity after annealing at 550 °C. However, the value of saturation magnetisation becomes lower after annealing. This change in the magnetic properties could be caused by the different nitrogen concentrations, hence different $Fe_xN_{(1-x)}$ phases. This also could results in different hybrid interfaces between $Fe_xN_{(1-x)}$ and RF-sputtered a-C.

The magnetic energy product (BH) was calculated in the $Fe_xN_{(1-x)}$/RF-sputtered a-C system after annealing at 500 °C. The results show a maximum magnetic energy product of about 9 kJ/m^3 for 5 nm of RF-sputtered a-C grown on top of a 9 nm thick layer. However, a maximum magnetic energy product of about 53 kJ/m^3 was observed in the Fe/RF-sputtered a-C after annealing this system at 500 °C.

The Raman spectra indicated a shift in the G peak to higher frequencies and the ratio of I(D)/I(G) increases when carbon is annealed at a higher temperature. The

changes in the Raman spectra give evidence that the RF-sputtered a-C layer changes into nanocrystalline graphite, and the orbital hybridisation changes from sp^3 to sp^2 accordingly. This change of sp^3 orbitals into sp^2 orbitals after annealing leads to confirms the corresponding changes in the magnetic properties.

CHAPTER 6

Magnetic properties of 3d transition metals with C_{60} thin films

6.1 Introduction

In this chapter, we investigate the magnetic properties of Fe/C_{60} bilayers at room temperature and the impact of annealing at 100 - 150 - 200 °C. The study is similar to Fe/RF-sputtered a-C interfaces, except that a-C is replaced with C_{60}. We used C_{60} because the molecules are easily deposited on the top of metals [57, 70, 171] and because C_{60} has a simple structure with a higher spin orbit coupling and potentially large charge transfer [17]. We also study the magnetic properties of Co/C_{60} thin films. SQUID-VSM magnetometry was used to measure the magnetic moment of the samples at 300 K, 5 K and 3 K after cooling down to 2 K or 3 K in a high field of 70 kOe. These magnetometry results contribute significantly to the findings of this study. The effect of annealing on the magnetic properties at room and low temperatures of Co/C_{60} thin film is also investigated .
We used transport measurements in the metallo-molecular systems to probe the magnetic structure and the hybridisation effect at the metallo-molecular interfaces [21, 83]. Our research suggests the possibility that charge transfer at the Co/C_{60} interface may affect the transport properties. The behaviour of resistance as a function of magnetic field at different temperatures was also investigated in the Co/C_{60} thin films.

6.2 Effect of annealing on the magnetic properties of Fe with C_{60} thin films

6.2.1 Magnetisation of Fe/C_{60} interfaces before and after annealing

The samples studied had the same structure as those in the previous chapter, but the RF-sputtered a-C was replaced by C_{60}. The metal films were grown by sputtering deposition, and C_{60} molecules were thermally sublimated in-situ in a chamber with a base pressure of 10^{-8} Torr. Structures of Ta(5 nm)/Fe(t)/C_{60}(R)/Ta(10 nm) were grown on silicon oxide substrates, with 0.5 nm $<$ t $<$ 16 nm and the C_{60} thicknesses (R) were fixed at 10 nm, 20 nm and 50 nm. The samples were annealed from 100 °C to

200 °C for 2 hours in a vacuum of approximately 10^{-5} Torr. The Fe/C_{60} magnetometry measurements were compared to those of control samples without C_{60}. TEM measurements by Wheeler show smooth interfaces in C_{60}/Co multilayer thin films [70]. C_{60} layer becomes continuous and smooth when the thickness is about (10-20) nm [91].

First, the magnetic moment for all samples was measured at room temperature before annealing. The magnetic field was applied in-plane along the easy axis of the samples, as determined by the growth field. We observed in the magnetometry measurements that the magnetisation at room temperature was lower when the Fe was coupled with C_{60}. As the metallic layer became thicker the bulk properties dominated. Figure 6.1a shows changes in the magnetisation after annealing at different temperatures as a function of Fe thickness. The results indicate a decrease in room temperature M_s as the annealing temperature is increased, beginning after 150 °C. This behaviour may be attributed to charge transfer from Fe to the molecular C_{60}. The characteristics of the hybridisation depend on the contact geometry and electronic properties of the contact metal. These can be tuned and lead to changes in the electronic structure of the metal, just as the molecular leads to change in the density of states. The molecular orbitals may broaden and shift towards the Fermi level in the metallic system [83]. Figure 6.1b shows results for the control samples of Ta(5 nm)/Fe(t)/Ta(10 nm), which were fabricated by sputter deposition without molecular C_{60}. The control samples show less change in the M_s as the thin films were annealed, which indicates that coupling Fe with C_{60} leads to changes in magnetic moment at the Fe/C_{60} interface. The decrease in magnetisation is dependent on the thickness of the Fe layer as shown in Figure 6.1c whereas the positive changing in the magnetisation appears at the thinner thickness of Fe . This reduction in M_s could be due to hybridisation between d and p orbitals at the Fe/C_{60} interface.

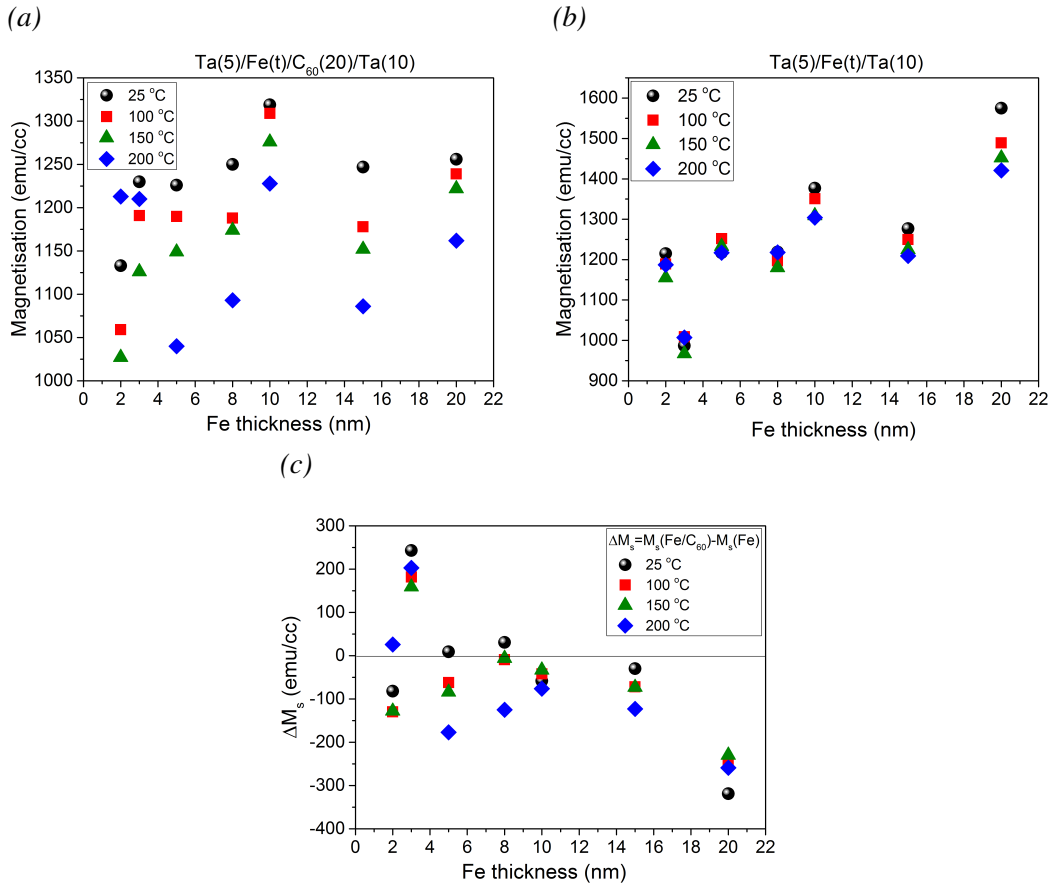

Figure 6.1: Magnetisation measurements as a function of Fe thickness. (a) M_s for Ta(5 nm)/Fe(t)/C_{60}(20 nm)/Ta(10 nm). (b) M_s for Ta(5 nm)/Fe(t)/Ta(10 nm) for different annealing temperatures. The bulk magnetisation in Fe which is about 1750 emu/cc [150, 151]. (c) Changes in M_s for Ta(5 nm)/Fe(t)/C_{60}(20 nm)/Ta(10 nm) and control samples Ta(5 nm)/Fe(t)/Ta(10 nm) measured by SQUID magnetometer at room temperature. The samples show dependence of the magnetisation on the Fe film thickness before and after annealing.The uncertainty in M_s that could be due to sputtering parameters such as growth pressure or substrate alignment or to variations in volume.

Figure 6.2 shows that M_s is dependent on the thickness of the Fe and C_{60}, as the C_{60} layer used is thinner (10 nm) or thicker (50 nm). The samples were measured first at room temperature and then annealed up to 200 °C for 2h in a vacuum of $\sim 10^{-5}$ Torr. Measuring all structures at room temperature (black data) shows a decrease in M_s values with increasing the C_{60} thickness, which indicates dependence on the C_{60}

thickness [83], as shown in Figures 6.1a ,6.2a and 6.2b. The same trend is observed in the M_s in our thin films after annealing up to 200 °C, as shown in Figure 6.2. The average of all structures confirmed that there is dependent on the C_{60} thickness (see Figures 6.1c, 6.2c and 6.2d). This could be due to an increase in the content area of C_{60} in the thin films, resulting in a smooth interface between the Fe/C_{60} after annealing.

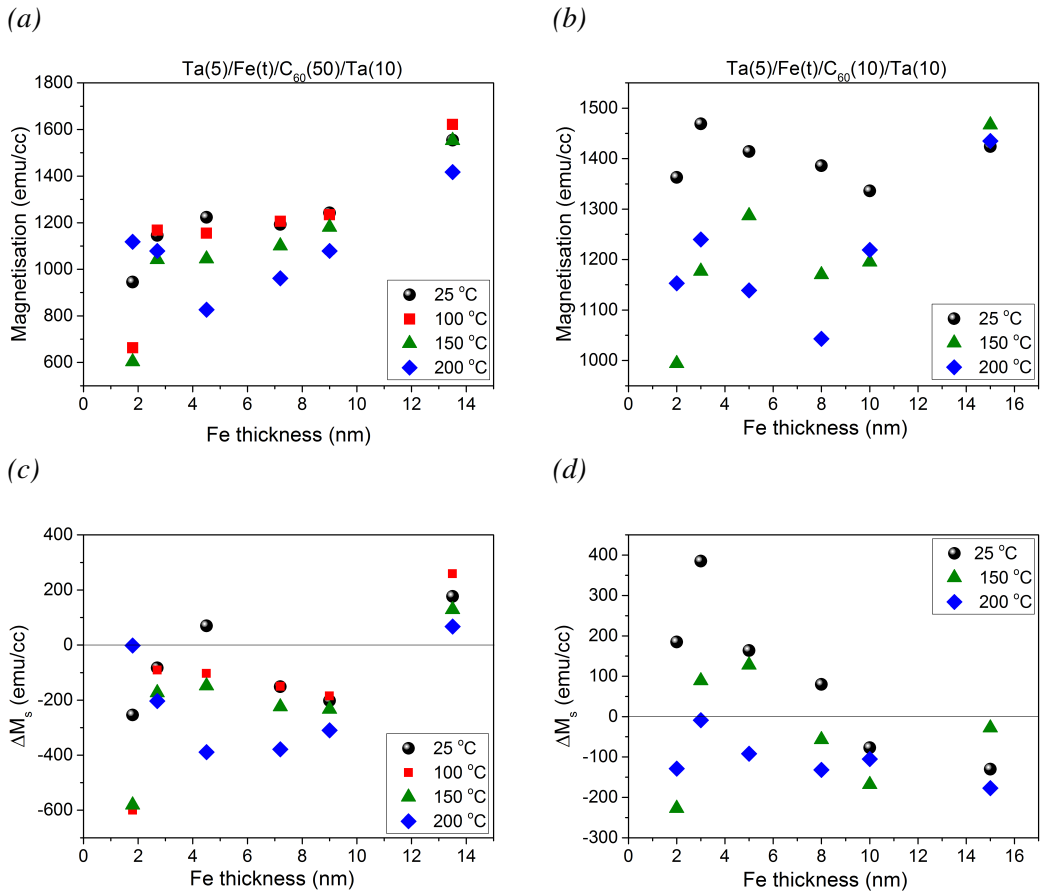

Figure 6.2: The magnetisation of the films as a function of Fe thin film thickness at different annealing temperatures. This shows that M_s decreases with increasing the annealing temperature up to 200 °C. Each data point is measured at 300 K. (a) M_s for Ta(5 nm) /Fe(t)/C_{60}(50 nm)/Ta(10 nm) (b) M_s for Ta(5 nm) /Fe(t)/C_{60}(10 nm)/Ta(10 nm). Changes in M_s for (c) Fe(t)/C_{60}(50 nm) and (d) Fe(t)/C_{60}(10 nm) with respect to control samples without a C_{60} layer where ΔM_s is (ΔM_s=M_s(Fe-C_{60}) - M_s(Fe)).

6.2.2 Coercivity of Fe/C_{60} interfaces before and after annealing

The in-plane coercivities for the same sample structure of Ta(5)/Fe(t)/C_{60}(20)/Ta(10) are shown in Figure 6.3 for Fe/C_{60} interfaces and control samples without C_{60} at room temperature before and after annealing. In Figure 6.3a and 6.3b there are significant changes before annealing and the data shows thickness-dependent coercivity. Significant changes were observed in thinner Fe layers of 2 and 3 nm after annealing at 150 °C. The coercivity increases by 50%, compared to control samples, when the samples are annealed at 150 °C as shown in Figure 6.3b. The results also show variation in the coercivity behaviour after annealing the thin film at different temperatures. As the temperature increases from 150 °C to 200 °C the H_c starts to decrease. This could be interpreted as evidence that the iron/carbon diffuses at a specific effective annealing temperature. Figure 6.3a also demonstrates that H_c rises with increased Fe thickness. In comparison with the control sample in Figure 6.3b, changes in H_c are clearly observed, see Figure 6.3c. Thus, altering the density of states at the Fe/C_{60} interface is possible due to hybridisation between the molecular p_z orbital and the 3d bands of Fe. Changes in H_c are highly dependent on Fe thickness.

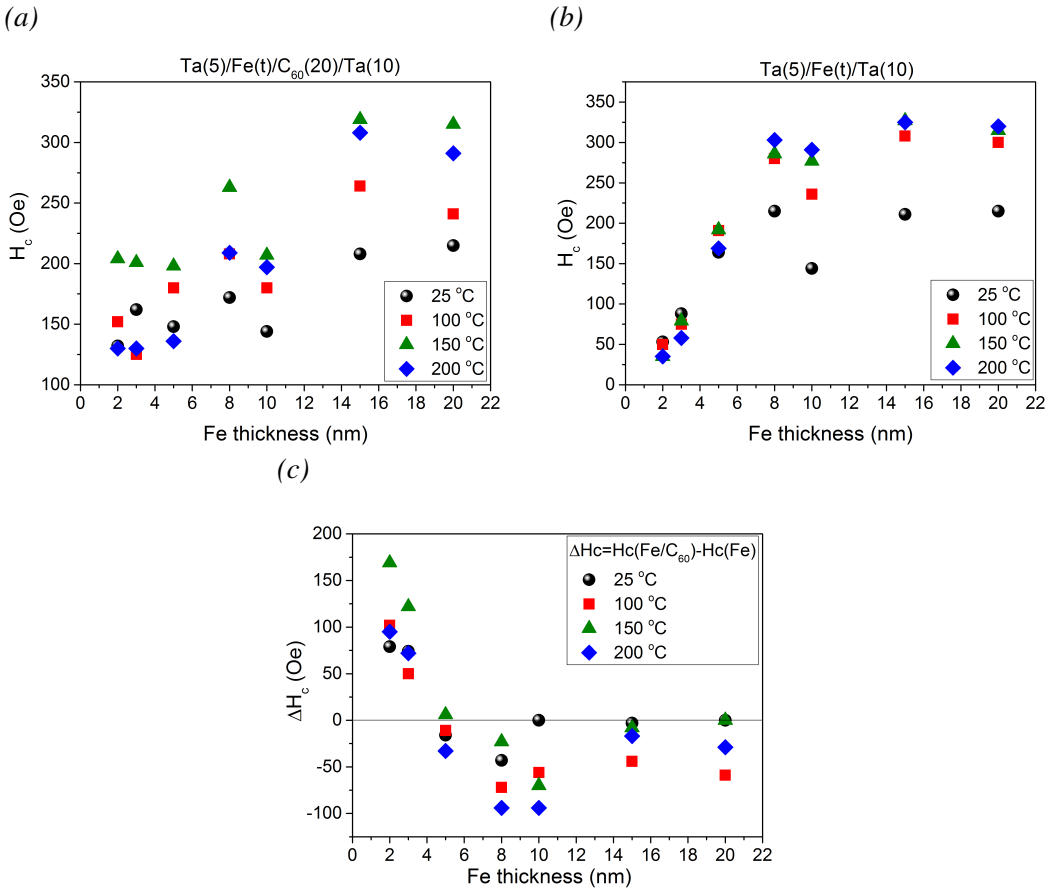

Figure 6.3: Illustrates the coercivity as a function of Fe thin film thickness at each of the annealing temperatures, when measured at room temperature: (a) for Ta(5 nm)/Fe(t)/C_{60}(20 nm)/Ta(10 nm) and (b) for control samples Ta(5 nm)/Fe(t)/Ta(10 nm). (c) shows changes in H_c (ΔH_c=H_c(Fe-C_{60}) - H_c(Fe)) as a function of Fe thickness, with enhanced coercivity below 4 nm. The interface becomes less relevant as the Fe layer grows thicker until the bulk properties of Fe dominate at 20 nm.

The same trend was observed with further increases in the thickness of the C_{60} layer as shown in Figure 6.4e and 6.4d, where the coercivity is enhanced when the Fe layer thickness is less than 4 nm, then starts to drop above 4 nm until the bulk properties of Fe dominate at 20 nm. Due to to the increase in magnetic anisotropy, this kind of behaviour in H_c after annealing was observed in the thinnest layer of Fe [28, 32].

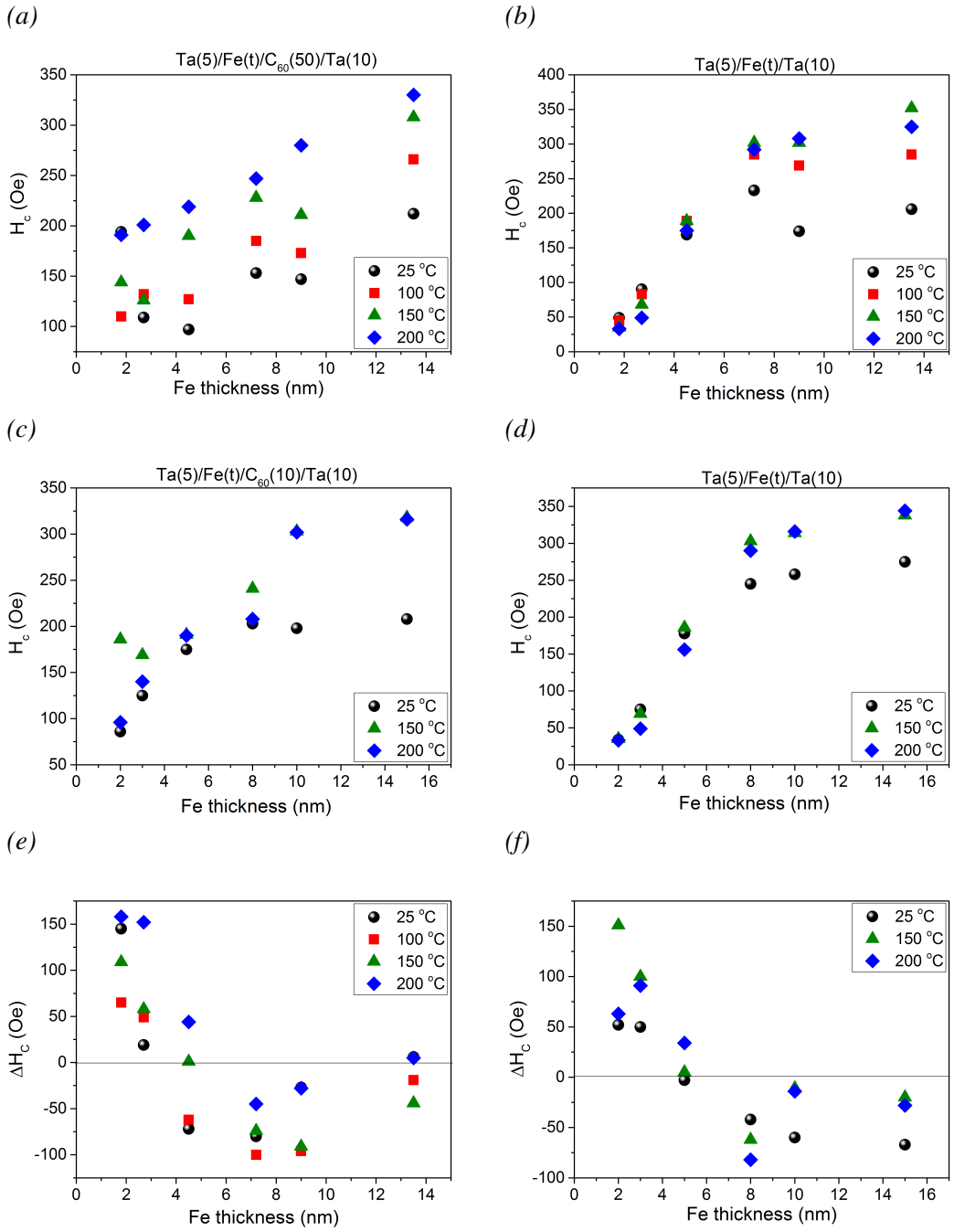

Figure 6.4: Dependence of H_c on the Fe thin film thickness for different thicknesses of C_{60} layer: (a) for Ta(5 nm)/Fe(t)/C_{60}(50 nm)/Ta(10 nm) and (b) control samples without C_{60}. (c) shows Ta(5 nm) /Fe(t)/C_{60}(10 nm)/Ta(10 nm) and (d) control samples without C_{60}. (e) and (f) show ΔH_c for Fe thin film coupled with 50 nm and 10 nm of C_{60}, respectively. It can be seen that for all samples H_c is enhanced after annealing and these changes in H_c are clearly dependent on the Fe thin film thickness, whereby ΔH_c is at its maximum when the Fe layer is thinnest.

6.3 Temperature dependent magnetisation and coercivity

Here, the M_s and H_c of the annealed samples of Fe/C_{60} were measured at low temperatures from 300 K to 2 K, in an in-plane applied field up to 5 kOe to ensure that the sample was fully saturated. Figure 6.5 shows the M_s and H_c of Ta(5 nm)/Fe(1.8 nm)/C_{60}(20 nm)/Ta(10 nm) and their control samples. The M_s(T) measurements for these samples were taken before and after annealing them in the tube furnace for two hours under a vacuum of 10^{-5} Torr. In Figure 6.5a, it can be seen that decreasing the temperature to 2 K led to an increase in M_s. The same effect can also be clearly observed in H_c, as indicated in Figure 6.5c. This behaviour is different from the control samples, Ta(5 nm)/Fe(1.8)/Ta(10 nm), which suggests that the effect is due to the coupling of Fe with C_{60}, as shown in Figures 6.5b and 6.5d. The results in Figure 6.5 show that coupling the Fe and C_{60} does not improve the H_c and M_s beyond 100 K. At 90 K, a high order transition is observed where the rotational degrees of freedom have been frozen [172, 173]. This may indicate that after 100 K there is no charge transfer or hybridisation between 3d bands in the Fe and the carbon orbitals as a result no enhancement in M_s and H_c as shown in Figure 6.5a and Figure 6.5c.
For each temperature, the ΔM_s and ΔH_c were extracted from the hysteresis loops and these values are plotted in Figures 6.5e and 6.5f. This indicates that temperatures in the region of 100 K yielded no further increase in the values of H_c and M_s.

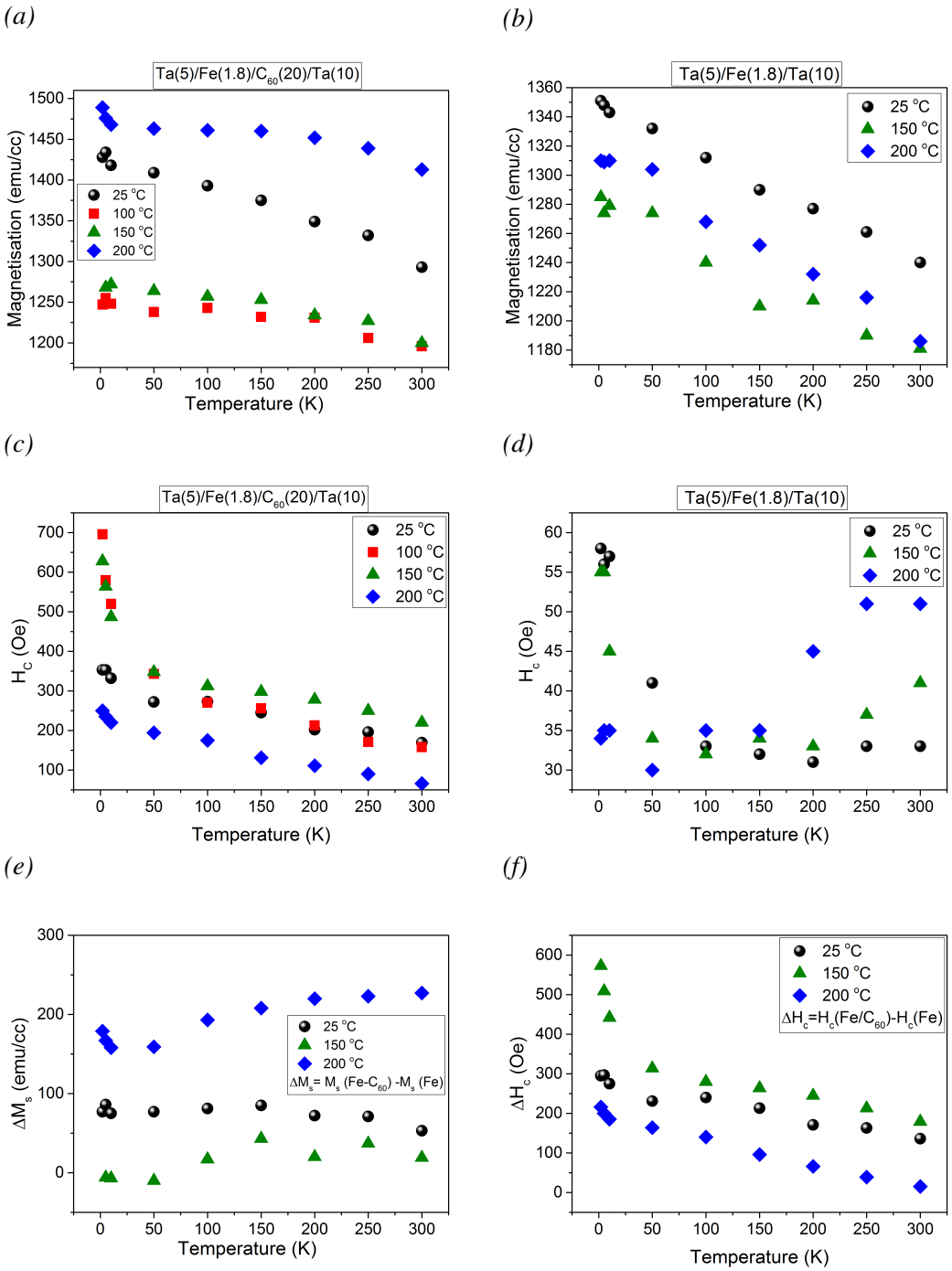

Figure 6.5: M_s versus T curves for (a) Ta(5 nm)/Fe(1.8 nm)/C_{60}(20 nm)/Ta(10 nm) and (b) Ta(5 nm)/Fe(1.8 nm)/Ta(10 nm). H_c versus T curves for (c) Ta(5 nm)/Fe(1.8 nm)/C_{60}(20 nm) and for (d) Ta(5 nm)/Fe (1.8 nm)/Ta(10 nm). (e) Magnetisation change (ΔM_s) and (f) coercivity change (ΔH_c), as a function of measuring temperature. The samples show the dependence of magnetisation and coercivity on the temperature. The results show that the largest increases in magnetisation and coercivity are obtained in the low temperature region (2 K).

The data were fitted using Blochs $T^{3/2}$ law, which describes the temperature dependence of magnetisation of magnetic materials [174]. The magnetisation as a function of temperature is given by

$$M(T) = M_0 \left[1 - \left(\frac{T}{T_c} \right)^{\frac{3}{2}} \right]^{\beta}, \tag{6.1}$$

where M_0 is the spontaneous magnetisation at absolute zero, T_c is the Curie temperature and β is a critical exponent. From Equation 6.1 we can use a modified version of Blochs law to take into account the anisotropy and behaviour close to T_c , as seen in Figure 6.6. After annealing, fitting to Blochs law for Fe(1.8 nm)/Ta(10 nm) shows the value of T_c to be 1000±40 K, which is close to the bulk value of Fe (1043 K) [174] whereas Fe(1.8 nm)/C_{60}(20 nm)/Ta(10 nm) shows 1400±100 K , which is higher than the bulk value of Fe . The observed Curie temperature in Fe/C_{60} that could be owing an exchange interaction between Fe and C_{60}. Another possibility for increasing T_c in the Fe/C_{60} system after annealing is the formation of domains. In order to confirm this new results, it is not possible to anneal C_{60} above 300 K. Using RF-sputtered a-C could be useful to explore this changing in T_c in Fe/RF-sputtered a-C system.

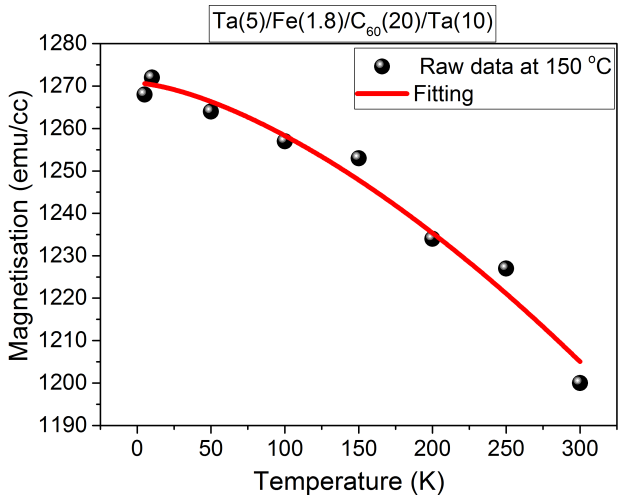

Figure 6.6: Magnetisation versus temperature for Fe(1.8 nm)/C_{60}(20 nm)/Ta(10 nm) film after annealing at 150 °C . The red line is a fit using the Bloch $T^{3/2}$ law and this gives the value of Curie temperature 1400±100 K which is higher than the bulk value of Fe (1043 K). Here β = 0.5 where the best fitting is obtained.

Similar measurements were done for the same sample structure but with a thicker Fe layer of 5 nm (Figure 6.7). These measurements support the previous results, where H_c increases gradually as the temperature decreases in iron layers coupled with C_{60}, but no change is observed in the control sample. Also, the M_s showed 250 emu/cc difference between the molecular coupled and the un-coupled sample when annealed at 200 °C.

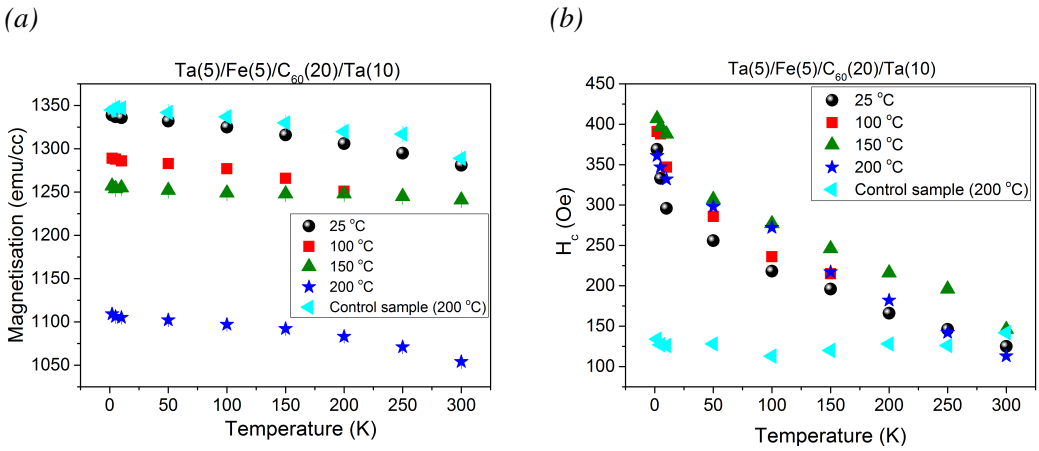

Figure 6.7: (a) M_s and (b) H_c as a function of temperature for un-annealed and annealed samples, as indicated in the inset, for structures of Ta(5 nm)/Fe(5)/C_{60}(20 nm)/Ta(10 nm) and the control sample, which was annealed at 200 °C only. The data shows the effect of annealing on M_s and H_c with 5 nm thick Fe.

Next we looked at thinner C_{60} films of 10 nm instead of 20 nm, as shown in Figure 6.8. The samples were annealed at 150 °C for 2h in a vacuum about 10^{-5} Torr. The H_c(T) curve clearly shows a compensation point around 100 K and the H_c also depends on the thickness of the Fe layer. A high order transition is observed at 90 K, where the rotational degrees of freedom have been frozen at 90 K [172, 173].

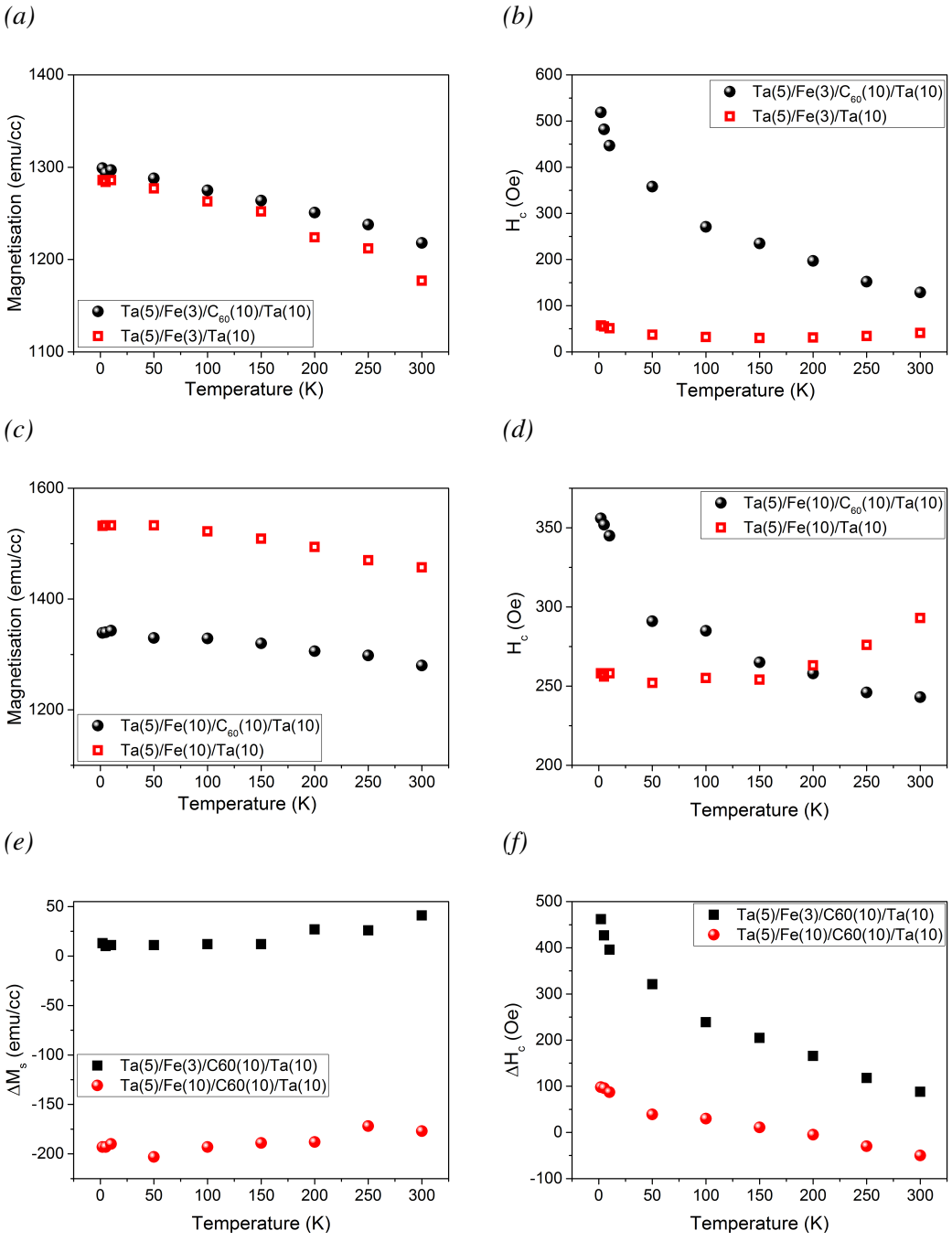

Figure 6.8: The temperature dependence for different structures of Ta(5 nm)/Fe(t)/C_{60}(10 nm)/Ta(10 nm) where t is 3 nm and 10 nm (a) M_s (b) H_c for 3 nm Fe layer and (c) M_s (d) H_c for 10 nm Fe layer. Control samples without C_{60} for each sample are plotted in the same graph. The data for the samples shows that increasing the Fe film thickness leads to a corresponding reduction in ΔM_s, see Figure (e). However, ΔH_c increases in the low temperature region of about 450 Oe and 100 Oe, for 3 nm and 10 nm of Fe, and depends on the thickness of the Fe thin film, as presented in (f). Here, the samples annealed at 150 °C for 2 hours in a vacuum $\sim 10^{-5}$ Torr.

The M_s and H_c were then observed, this time keeping the Fe layer constant while varying the thickness of the C_{60} layer without annealing.

Figure 6.9 shows how the magnetic behaviour is dependent on temperature. The coercive field was obtained from the hysteresis loops indicate increases in H_c as temperatures were lowered. The C_{60} layers were varied at 20 nm, 30 nm and 50 nm, and similar behaviour was observed at all thicknesses. The H_c(T) curve clearly shows that the thickness of the C_{60} may contribute to changes in the amounts of charge transfer and anisotropy. The hybridisation effect between the π carbon orbital and 3d metals band could play a significant role in altering the magnetic properties in interfacial coupling [28].

Low temperature results obtained from SQUID-VSM of an Fe/C_{60} hybrid structure show a thickness dependence for both the metallic and molecular layer. The temperature dependent coercivity reveal repression above 100 K, where H_c starts to reach a minimum. The maximum values for H_c observed at 2 K and this may indicate a change in the magnetic behaviour of Fe/C_{60} at low temperature.

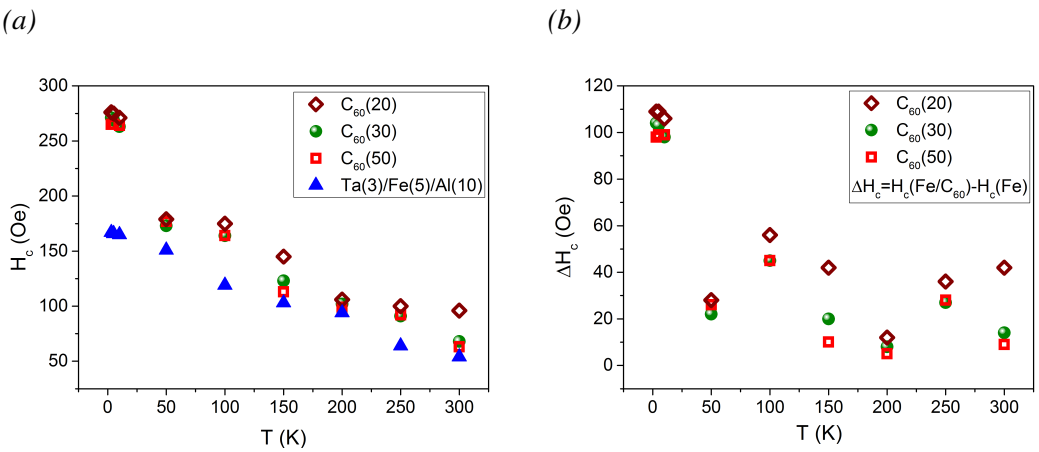

Figure 6.9: The temperature dependence of (a) coercivity and (b) ΔH_c for un-annealed samples of Ta(3 nm)/Fe(5)/C_{60}(t nm)/Al(10 nm), where t is 20 nm, 30 nm and 50 nm. Results show that coercivity increases as temperature is lowered.

6.4 Co/C_{60} interfaces

6.4.1 Magnetometry of Co/C_{60} bilayers

In this section, we focus on the transition metal Co and its interface with C_{60}. First we measured the samples with the structure Ta(3 nm)/Co(t)/Ta(10 nm), where (t) varied from 2 nm to 15 nm. The purpose of using a wide range of Co thicknesses is to check the presence of a magnetically-inactive layer (dead layer) by linear extrapolation of the magnetic moment over area versus thickness. This dead layer exists at the Co/Ta interface and is about 1 nm thick with a small error as indicated in Figure 6.10.

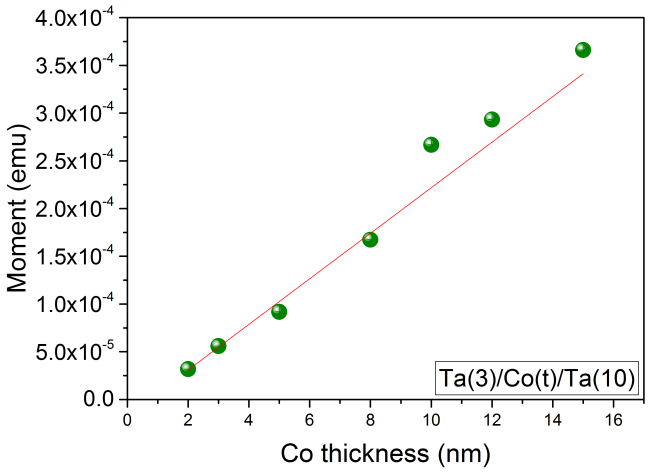

Figure 6.10: The linear extrapolation of magnetic moment as a function of Co thickness indicates that there is a dead layer of ∼ 1 nm thick.

In order to explore the influence of coupling Co with C_{60}, different thicknesses of Al cap layer were used: 2 nm, 5 nm, and 10 nm. This is because the aluminium cap plays a key role in preventing oxidation of the sample, giving a clean interface between the Co and C_{60}. The influence of coupling and the capping layer thickness was studied by measuring the hysteresis loops at 5 K after cooling in a high field of 70 kOe. Co(3 nm) with C_{60}(35 nm) samples show an increase in the coercive field when the thickness of the Al cap is increased as demonstrated in Figure 6.11a.The changes in

H_c observed in Figure 6.11a could be because of having a pristine interface when Al is thick enough, as oxygen would not penetrate and hence would not affect the coupling between the Co and C_{60} when the thickness of the Al cap is much thinner. This increase also in H_c could be attributed to pinning and antiferromagnetic interactions that indicate the transfer of charge from the Al cap to the Co/C_{60} system, since when two materials of different chemical potentials come into contact then charge transfer takes place [70, 90, 175]. Another possibility is that the increase in H_c points to a complex system of a hard and a soft layer, each with a different coercive field: a so-called exchange spring [176–178]. This phenomenon has been observed in many systems, for example SmCo/Fe [177]. Within the region the spin is hard to saturate and a pinning effect takes place whereby the point in the soft layer flows into the applied magnetic field; however, when it moves toward the interfaces the pinning become stronger [179]. Thus, the Co/C_{60} become harder to saturate in this region.

A control sample without C_{60} with the structure of Ta(4 nm)/Co(3 nm)/Al(10 nm) was measured in the same conditions and cooled in a 70 kOe magnetic field from room temperature and measured at 5 K, as shown in Figure 6.11b. As expected, no change in H_c was observed in the control sample, which indicates that the effect in Figure 6.11a appears due to coupling the Co with C_{60}.

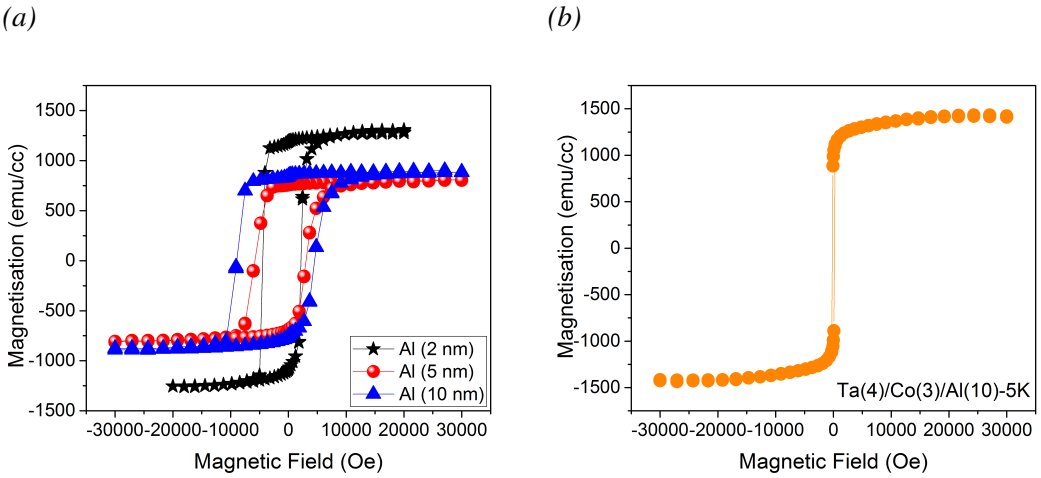

Figure 6.11: Magnetisation vs magnetic field (a) for a structure of Ta(4 nm)/Co(3 nm)/C_{60}(35 nm)/Al(t), where (t) is 2 nm, 5 nm and 10 nm, cooled in a field of 70 kOe and measured at 5 K. (b) Control sample of Ta(4 nm)/Co(3 nm)/Al(10 nm) measured at 5 K. The samples show that coercivity rises as the Al thickness is increased after cooling the Co/C_{60} at high field, whereas the H_c did not change in the control sample.

We have also demonstrated the effect of temperature on a bilayer system of Co/C_{60} after warming the samples up to 350 K. Hysteresis loops of the Ta(3 nm)/Co(6 nm)/C_{60} (35 nm)/Al(5 nm) sample were measured at different temperatures. First, the sample was heated to 350 K under a pressure of 4 mTorr in a He atmosphere in a magnetometry device (SQUID-VSM) with a magnetic field of 70 kOe. The sample was then cooled down to 2 K under a high field (70 kOe) and the hysteresis loops for each temperature were recorded, see Figure 6.12a. The M_s and H_c were extracted from the hysteresis loops and plotted as a function of temperature as shown in Figure 6.12b and 6.12c. Both M_s and H_c show an increase at 2 K. The coercivity appears at 2 K about 2 kOe after cooling down to 2 K under a high field (70 kOe). Annealing the Co/C_{60} sample could lead to a change in its crystallinity and morphology. From these results it appears that the coercive field of the Co/C_{60} bilayer sample is enhanced by compressing the control samples as illustrated in Figure 6.12b, and the M_s is also increased, see Figure 6.11a. This enhancement in the H_c of Co/C_{60} may be related to an antiferromagnetic coupling at the Co/C_{60} interface which takes place between the Co and the first layer of C_{60} [70]. Another possibility for this enhancement in H_c is the formation of pinned domains [180–182]. Due to disorder in the Co/C_{60} system, applying a high

field during the cooling process leads to alignment of the frustrated states where Co has hybridised with C_{60}. The magnetic anisotropy can be enhanced by coupling Co/C_{60} as reported in research on graphene/Co thin films [183].
The application of a large reversal field is then required to flip these magnetic domains. To ensure that the effect is due to Co/C_{60} coupling and not to intrinsic Co behaviour, a control sample with the same structure but without the C_{60} layer was measured under the same conditions, see Figure 6.12. The H_c of the control sample showed no change with temperature, which provides clear evidence of the role of Co/C_{60} coupling. The M_s of bulk Co has been found to be approximately 1400 emu/cc [184].

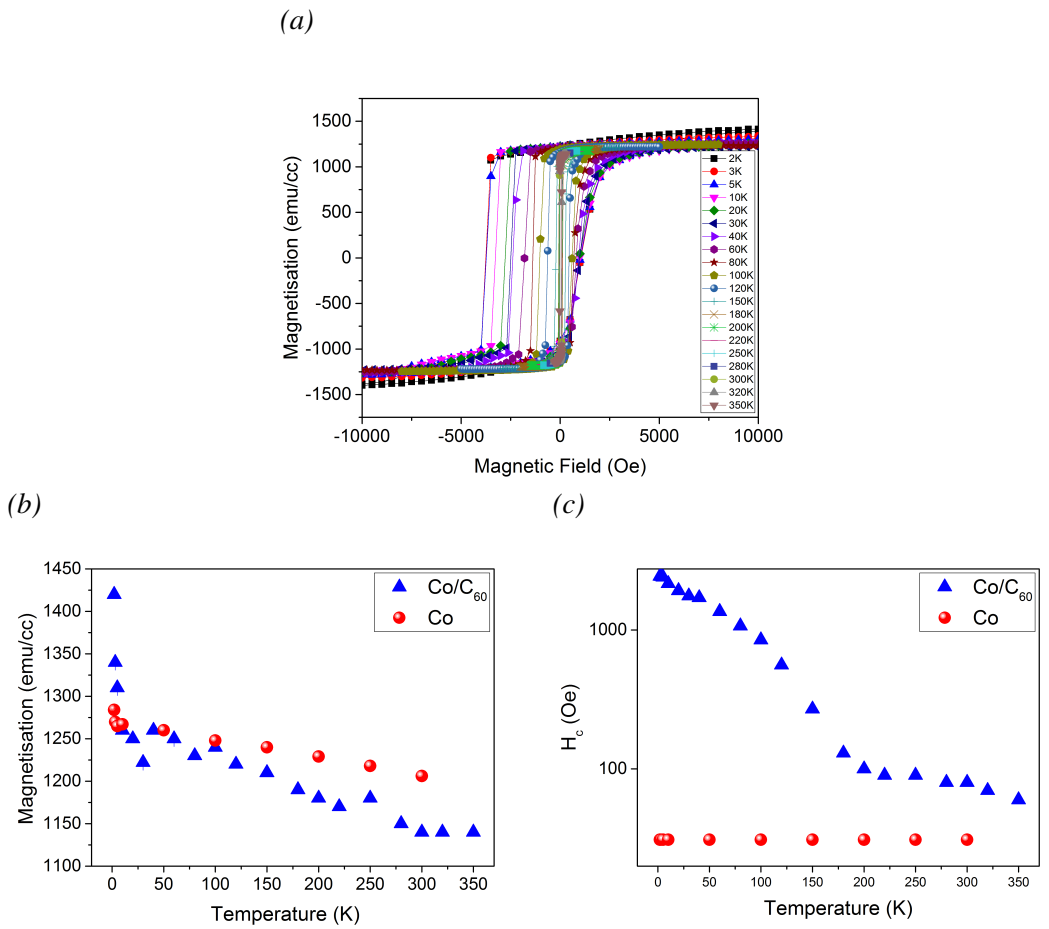

Figure 6.12: The field-cooled data for a structure of Ta(3 nm)/Co(6 nm)/C_{60}(35 nm)/Al(5 nm) and a control sample of Ta(3 nm)/Co(3 nm)/Ta(10 nm) measured at different temperatures using SQUID-VSM. (a) The hysteresis loops for a structure of Ta(3 nm)/Co(6 nm)/C_{60}(35 nm)/Al(5 nm) measured at different temperatures. The temperature dependence of (b) the M_s and (c) the H_c, where we observed an increase in $M_s(T)$ and $H_c(T)$ in the low temperature region. The $H_c(T)$ in a control sample (red curve) indicates no change with temperature. Each data point presented in the $M_s(T)$ and $H_c(T)$ curves was extracted from the hysteresis loops at each temperature. The hysteresis loops at different temperatures were taken along the easy axis after cooling in 70 kOe.

Here we compare C_{60} coupling between Co and Fe. Equivalent multilayers were studied with Co and Fe, with the structure of Ta(4 nm)/Co(3 nm)/C_{60}(35 nm)/Al(8 nm) and Ta(5 nm)/Fe(2 nm)/C_{60}(20 nm)/Ta(10 nm) respectively. The samples were warmed up to 359 K, then both systems were measured at 3 K after being field-cooled in a magnetic field of 70 kOe. The magnetic field was applied in-plane along the easy axis of the thin film. In the Fe/C_{60} system, the results indicated changes in H_c rising to 1400 Oe at 3 K, whereas the Co/C_{60} showed a massive increase in H_c when a positive field was applied. $H_c{}^+$ is 3300 Oe, whereas in a negative applied field $H_c{}^-$ is about -11400 Oe and the approximate value for the exchange bias (H_{ex}) is about -4100 Oe, as seen in Figures 6.13b and 6.13d. These results are evidence that the coupling of Co/C_{60} is stronger than that of Fe/C_{60}. This could suggest that the charge transfer and hybridisation is greater at Co/C_{60} interfaces than at Fe/C_{60} interfaces. Co also shows large exchange bias when coupled with the C_{60} [185]. The magnetic hardening effect could take place [8, 186] in our Co/C_{60} thin films where C_{60} can contribute to making our Co/C_{60} thin film a hard system, owing to the exchange bias effect at the interface where there is a shift in the hysteresis loop of the FM [186].

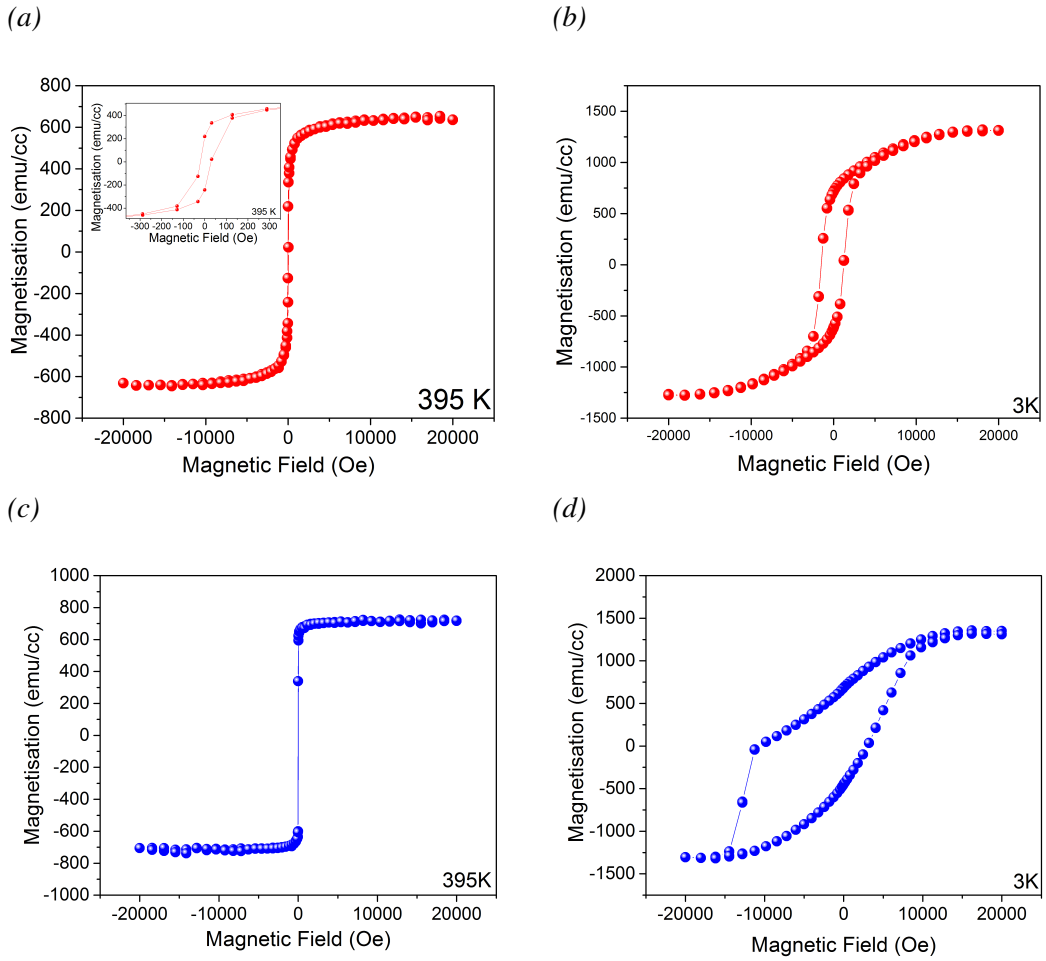

Figure 6.13: Magnetisation versus applied field curves for thin films of Ta(5 nm)/Fe(2 nm)/C_{60}(20 nm)/Ta(10 nm) (red curves) and Ta(4 nm)/Co(3 nm)/C_{60}(35 nm)/Al(8 nm) (blue curves) measured after heating to 395 K (a) and (c), and then cooling to 3 K (b) and (d). Measuring at 3 K shows a rise in H_c and is the largest effect observed in the Co/C_{60} system.

To investigate the impact of annealing, the bilayer Co/C_{60} sample was annealed at 200 °C for 2 h in a vacuum of $\sim 10^{-5}$ Torr. The annealed sample was cooled down in SQUID under a magnetic field of (70 kOe) and measured at 5 K, then the system was heated to 300 K and measured at that temperature, as shown in Figure 6.14. The annealed sample shows a $\sim$ 4 times increase in H_c than that observed in the un-annealed sample. For the annealed sample, the coercive field when a positive field is applied ($H_c{}^+$) is 7300 Oe, whereas with a negative field, the $H_c{}^-$ is about -15500 Oe and the approximate value for the H_{ex} is about -4100 Oe. The un-annealed sample shows the coercive field $H_c{}^+$ = 4500 Oe when a positive field is applied, whereas with a negative field $H_c{}^-$ = -9200 Oe with the approximate value for the H_{ex} = -2400 Oe. This indicates that annealing the Co/C_{60} leads to an increase in magnetic anisotropy and molecular coupling. This could originate from a decrease in the grain size of C_{60} that increases the density of the C_{60} film and the surface coupling to Co atoms [187]. There is therefore also the possibility of increasing the Co contact in the film as well as the magnetic anisotropy [188].

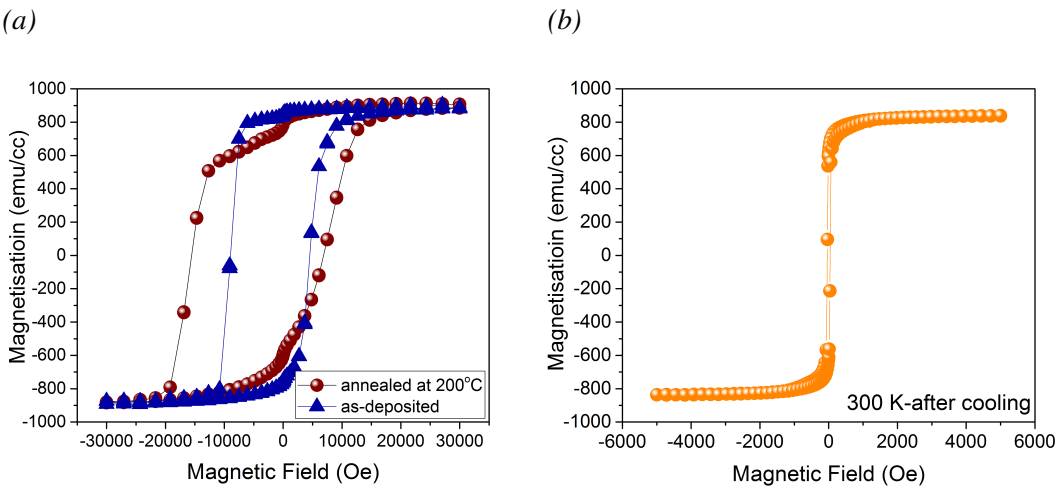

Figure 6.14: M_s dependence of the magnetic field of (a) Ta(4 nm)/Co(3 nm)/C_{60}(35 nm)/Al(10 nm) as-deposited (blue curve) and after annealing at 200 °C (red curve) where it was measured at 5 K and (b) the annealed sample measured at 300 K after warming the system to room temperature shows quenching of the effect observed in (a). The hysteresis loops for both annealed and as-deposited samples become broader after being cooled to a low temperature (5 K) under a magnetic field of (70 kOe).

6.4.2 Transport measurements of Co/C_{60} thin films

Anisotropic magnetoresistance (AMR) is a change in electrical resistance when a ferromagnetic thin film is subjected to an applied magnetic field due to spin orbital coupling [189]. AMR can indicate a strong spin orbital coupling (SOC) at an interface, as reported in [190]. Transport properties in the Co/C_{60} system were investigated. In this section, the behaviour of resistance as a function of magnetic fields was observed at different temperatures. The studied sample is a bilayer Co/C_{60} film with the structure Ta(4 nm)/Co(3 nm)/C_{60}(35 nm)/Al(10 nm). Figure 6.15 shows the field dependence of the resistance in the studied sample. The longitudinal MR for Co(3 nm)/C_{60}(35 nm) at each temperature was measured twice (first field sweep and second field sweep). The MR was measured at different temperatures of 5 K, 50 K and 100 K as presented in Figure 6.15. The MR at 100 K shows no change in resistence between the different sweeps ,whereas the MR at 50 K shows a change in resistance between the different sweeps that is due to temperature drift. At 5 K, the longitudinal MR exhibits a strong field dependence (first sweep) which is consistent with the magnetometry measurement (see Figure 6.11a for the sample with 10 nm of Al cap). In the first magnetic field sweep, formation of domain pinning [180–182] leads to incompletely aligned Co spins in the negative magnetic field region between 0 kOe and -20 kOe [185, 191]. The imperfect alignment of the Co layer to the magnetic field could reduce scattering in the cross-section of orbitals due to Co resistance (R) [185]. The second sweep could be indicate different switch mechanism after the first sweep. The data obtained in Figure 6.15 show the temperature dependence of the MR which is progressively reduced when the temperature reaches 100 K.

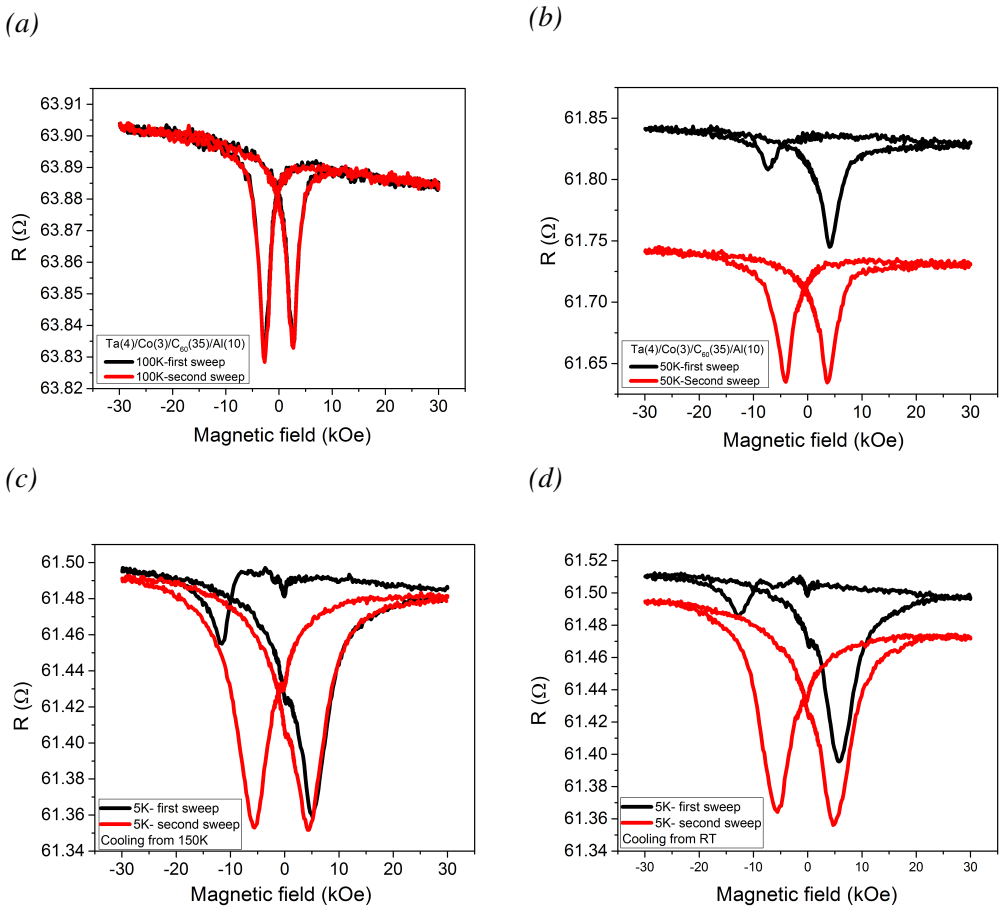

Figure 6.15: Field-dependent raw resistance for a sample with the structure Ta(4 nm)/Co(3 nm)/C_{60}(35 nm)/Al(10 nm) measured at different temperatures: (a) 100 K, (b) 50 K, (c) 5 K, where the sample was cooled under a magnetic field (30 kOe) from 150 K to 5 K and (d) 5 K, where the sample was cooled under a magnetic field (30 kOe) from room temperature to 5 K. The data also shows the temperature dependence in the first and second magnetic field sweep. The illustrated AMR obtained at 5 K and 50 K during the first magnetic field sweep showed a significant shift, whereas the second magnetic field sweep showed saturation behaviours for both temperatures. All measurements were taken after field-cooling (FC) with +30 kOe.

To confirm that the magnetic state is affected by the way the sample is cooled down, we measured the same sample but under different cooling conditions as presented in Figure 6.16. First, in Figure 6.16a, the sample was cooled from 300 K to 5 K without applying any magnetic field. Then, the resistance as a function of magnetic field was measured at 5 K. The curve showed a symmetric loop as observed before (Figure

6.15a). Second, a negative magnetic field of -30 kOe was applied to the sample at 300 K, then the sample was cooled down with this field to 5 K, and a resistance curve was recorded as a function of the magnetic field (Figure 6.16b). The same steps were followed to obtain the results in Figure 6.16d, but a positive field was applied while cooling the sample. Two sweeps were run for each measurement. The first sweeps MR in each measurement, for both negative and positive applied fields, give clear evidence that is due to the magnetisation reversal without the formation of a domain wall, as shown in Figures 6.16b and 6.16d. The direction of the magnetic field shows a strong effect on the AMR, as reported in a Co/MOEP system [185]. However, different reversal mechanism after the first sweep, which could be due to the physical realignment of the molecules as illustrated in Figure 6.16c and 6.16e.

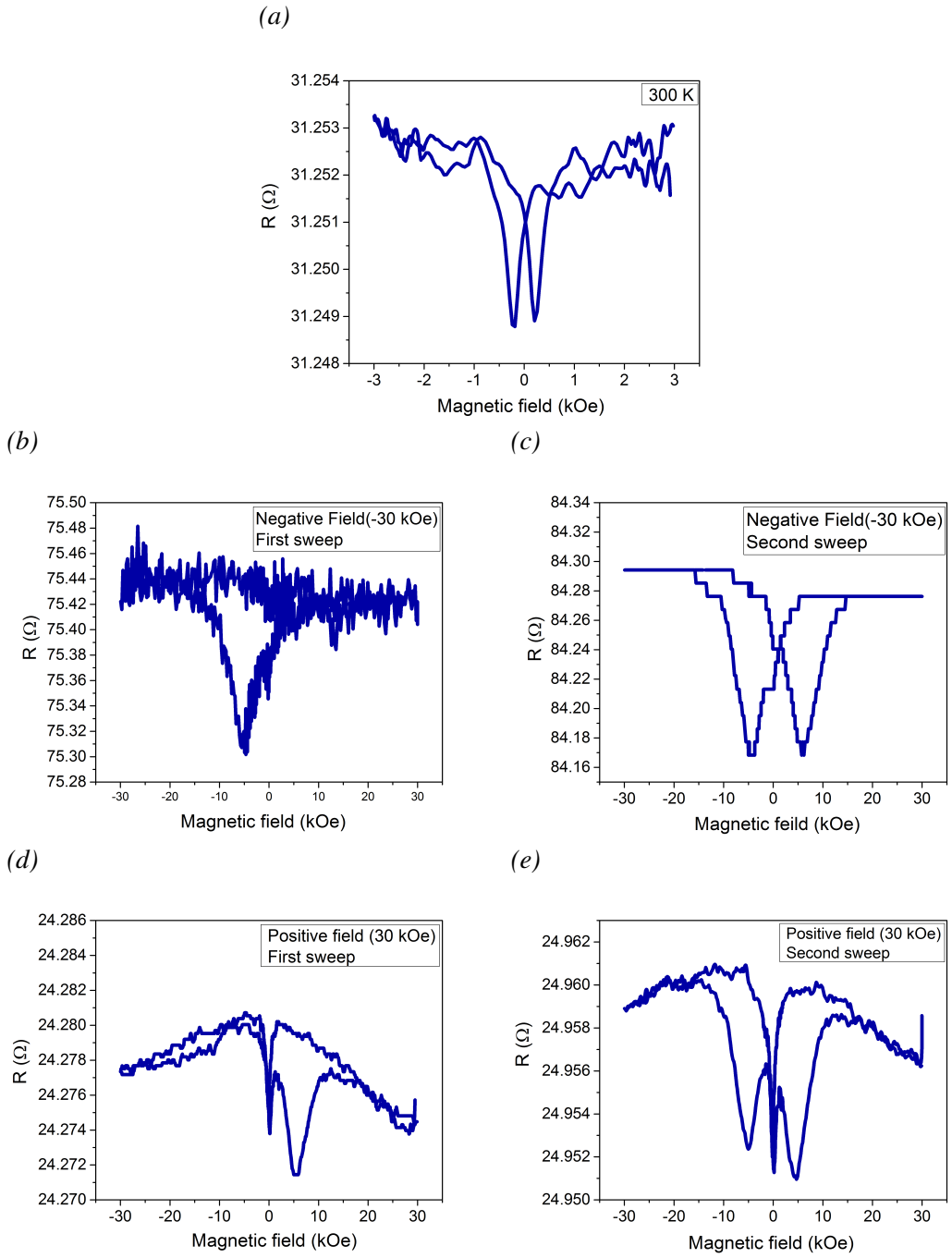

Figure 6.16: Magnetic field dependence of the resistance at 5 K but with different cooling conditions for Ta(4 nm)/Co(3 nm)/C_{60}(35 nm)/Al(10 nm). (a) Sample cooled from 300 K without any applied field and measured at 5 K. In (b) and (c) a negative field of 30 kOe was applied while cooling down. (d) and (e) show the sample cooled down with a positive field of 30 kOe. The magnetic field was aligned parallel to the thin film plane and the current.

6.5 Conclusion

In this chapter, we have looked at the effects on the magnetic properties of thin films when coupling C_{60} with two transition metals, Fe and Co. First, Fe/C_{60} interfaces were studied in bilayer systems embedded between two Ta layers. The magnetic properties of these samples were measured and compared with control samples without the C_{60} layer. Our findings show changes in both M_s and H_c when the metallic layer is coupled with C_{60}. This could give an indication of hybridised states between Fe and C_{60} that confirm a charge transfer from the ferromagnetic layer into the molecular C_{60} film. Further study of the magnetic properties was carried out by annealing the samples at different temperatures, resulting in a further reduction of the magnetic moment of Fe/C_{60} interfaces and an enhancement in H_c. low temperature magnetometry measurements of Fe/C_{60} thin films suggest that it is not possible to improve the coupling of Fe and C_{60} beyond 100 K.

Second, the coupling between C_{60} and Co was studied with Al as a cap layer. Co/C_{60} samples showed a massive increase in H_c when the sample was cooled down to 5 K under a high field of 70 kOe , which was not observed in the control sample without C_{60}. This could be the result of an antiferromagnetic coupling between Co and the first C_{60} layer and/or the formation of an exchange spring magnet at the interface. To exclude any effect due to oxidation related to the Al cap, different thicknesses of Al cap were deposited on the top of Co/C_{60} bilayer and a thickness-dependent coercivity was demonstrated. The maximum coercive value appears for the thicker 10 nm Al cap, which may suggest that the Al cap contributes to charge transfer to the C_{60} layer, changing the coupling with the ferromagnet or that 10 nm are needed to completely avoid oxidation. Also, magnetometry measurements were performed on Ta(4 nm)/Co(3 nm)/C_{60}(35 nm)/Al(10 nm) after annealing at 200 °C for 2h in a vacuum of 10^{-5} Torr. A large exchange bias existed of $\sim$ - 4100 Oe compared to 2 kOe without annealing after cooling the sample up to 5 K with a field of 70 kOe . This increase in H_c could be the result of good crystallinity in the thin film after annealing. The enhancement in coercive field in the Co/C_{60} system before and after annealing opens the door to the potential for replacing rare earth permanent magnets. Besides magnetometry, AMR transport measurements of the same sample structure were observed at

different temperatures in fields of up to 30 kOe , in a direction parallel to the current. The findings show a strong AMR-dependent field at a low temperature of 5 K, which is in agreement with the data obtained by SQUID magnetometry. Our research findings also demonstrate manipulation of the AMR due to changes in the magnetisation reversal processes, which is dependent on the field applied during the cooling process [185].

CHAPTER 7

Conclusion and future work

This research explores the interactions between nanocarbon and/or molecules and 3d transition metals, and whether these significantly affect the magnetic structure through spin-dependent hybridisation effects.

We optimised the growth of RF-sputtered amorphous carbon (a-C) thin films by RF magnetron sputtering from a graphite target. Our RF-sputtered a-C showed a surface roughness of about 5.5$\pm$0.1 Å, which is in agreement with previous research [56]. In order to acquire a fuller understanding and characterisation of RF-sputtered a-C, we looked at the effect of growing it on a Si/SiO_2 substrate and then annealing it at temperatures of up to 400 °C. Raman spectroscopy measurements indicated the type of carbon that was present before and after annealing process, as described by Ferrari and Robertson [124], which can be defined within a three stage model as illustrated in Chapter 3. Raman spectra showed that the structure of the RF-sputtered carbon films was amorphous in the as-deposited films, however, annealing the films changed the structure to nanocrystalline graphite.

The structural and magnetic properties of Fe/RF-sputtered a-C were studied extensively before and after annealing using Raman spectroscopy, TEM, Kerr microscopy and SQUID-VSM. Our magnetometry results for as-deposited samples show that the saturation magnetisation (M_s) and coercivity (H_c), were dependent on the thickness of the metallic layer. When the metallic layer was $>$ 10 nm, the bulk properties dominated and the interfacial effect between Fe and RF-sputtered a-C was quenched. At thicknesses of under 10 nm, changes in the magnetic properties were observed. These changes could be influenced by charge transfer and hybridisation at the interface between RF-sputtered a-C and the 3d band of Fe. These magnetic properties of Fe/RF-sputtered a-C were altered when the films annealed at different temperatures. Annealing Fe/RF-sputtered a-C at 500 °C showed a significant change in the coercivity and magnetisation with a maximum change of 600 Oe and 1300 emu/cc respectively, which means that it is possible to make Fe/RF-sputtered a-C harder by annealing. Decoupling the interface using copper quenches the change in magnetic properties. The magnetic energy product of the Fe/RF-sputtered a-C was approximately 53 kJ/m^3 for 5 nm of RF-sputtered a-C grown on top of a 10 nm Fe layer, similar to that of Alnico and fer-

rites.

Experiments with trilayer and multilayer samples of Fe/RF-sputtered a-C systems revealed the possibility of making the system softer with a coercivity about 10 Oe before annealing. After annealing, trilayer samples of Fe/RF-sputtered a-C and multilayer samples showed increases in coercivity up to 700 Oe and decreases in magnetisation up to 200 emu/cc that indicate inter-diffusion at the interfaces.
Raman spectroscopy showed that RF-sputtered a-C layer changes from amorphous carbon into nanocrystalline graphite upon annealing at 500-550 °C and that the orbital hybridisation changes from 20% sp^3 to 0% sp^3. Changes in magnetic the domain size were observed after annealing using Kerr microscopy. The results illustrate changes in the H_c where the magnetic images show evidence of the large increase in the density of pinning points in Fe/RF-sputtered a-C after annealing which we attribute to carbon diffusion in grain boundaries and/or the formation of carbides.

This research also investigated the effect of the hybrid interface on the magnetic properties of RF-sputtered a-C coupled with $Fe_xN_{(1-x)}$. Iron nitride films were deposited with various percentages of N_2 by magnetron sputtering. The magnetic properties were studied before and after annealing for N_2/Ar fractions of 10% and 15%. Room temperature magnetometry data revealed small changes in the saturation magnetisation and coercivity after annealing. The maximum changes in H_c were achieved after annealing at 500 °C when the value of $(BH)_{max}$ obtained for $Fe_xN_{(1-x)}$/RF-sputtered a-C grown with 10% nitrogen was 9 kJ/m^3. This value is small compared to the interface between pure Fe and RF-sputtered a-C becuse the nitrogen in $Fe_xN_{(1-x)}$/ RF-sputtered a-C system quenched the hybridisation between Fe and RF-sputtered a-C. Similar to Fe/RF- sputtered a-C films, the Raman spectra of $Fe_xN_{(1-x)}$/RF-sputtered a-C for as-deposited and annealed samples showed a shift in the G peak to higher frequencies and the ratio of I(D)/I(G) increased when annealed at a higher temperature at 550 °C indicating a change to nanocrystalline graphite.

The coupling of C_{60} interfaces with Fe and Co was also studied in this research. Magnetometry results showed a change in the saturation magnetisation and coercivity before and after annealing when Fe was coupled with C_{60} from 90 Oe to 200 Oe. The

enhancement in H_c was less as that achieved in the Fe/RF-sputtered a-C, indicating less diffusion of carbon in the Fe/C_{60} system. The data also showed the thickness dependence of saturation magnetisation and coercivity. At low temperature measurements in SQUID, the M_s and H_c data show no improvement in the coupling between C_{60} and Fe beyond 100 K. The magnetometry results of Co/C_{60} hybrid structures showed an increase in H_c after cooling under a high field (70 kOe), both before and after annealing, and this increase was found to be dependent on the Al cap thickness. With a 10 nm Al cap, a large increase in H_c was observed after annealing. This may have been due to good C_{60} coverage of the Co film after annealing at 200 °C for 2 hours in a vacuum (10^{-5} Torr).

Low transport measurements corroborated the data obtained by magnetometry where Co/C_{60} thin films cooled down to 5 K in a high field (70 kOe) show a change in AMR after the first magnetic field sweep. In the first magnetic field sweep no AMR peak observed near zero field. This is due to the formation of domain pinning and incompletely aligned Co spins [180–182, 185]. To clarify the hybrid interfacial interaction between Co and C_{60} layers, the second magnetic field sweep was measured to demonstrate a different reversal mechanism, which may be due to the physical realignment of the C_{60}. In the second magnetic field sweep AMR peaks appear for both forward and backward sweeps. This also indicates the observation result in the first magnetic field sweep due to an exchange spring effect [176–178]. Our transport measurement finding show a strong AMR-dependent field at a low temperature of 5 K, which is in agreement with the data obtained via magnetometry where the large coercivity observed.

In conclusion, the magnetic interfacial effects between 3d transition metals and nanocarbon were investigated in this research. Annealing was found to alter the magnetic properties, leading to the possibility for creating free-RE element based permanent magnetic materials and ultra-soft single element magnets and a tunability of these properties through heat treatments. This could be important for applications requiring excellent combinations of high maximum energy product $(BH)_{max}$ and coercivity.

It is possible that future research may be able to tune the magnetic properties of FM/nanocarbon and FM/molecular interfaces and that observing the reaction times of

annealing Fe/RF-sputtered a-C could lead to further increases in the coercivity. We could also explore the domain structure and domain wall speed in Fe/RF-sputtered a-C samples as a function of temperature using variable temperature at high field Kerr microscopy. Another possible way of enhancing the magnetic properties of $Fe_xN_{(1-x)}$/RF-sputtered a-C is to deposit samples with a high substrate temperature in order to increase coercivity and hence obtain high maximum energy products. Controlling the substrates' temperature could also help to improve the quality of the thin films and provide better control on the growth process. Alternative substrate materials and temperatures can be optimised in order to study their influence on the magnetic properties and structure of thin films [192]. Changes in magnetic properties of Co/C_{60} resulting from modifications in the thickness of the Co could lead to the further study of magnetic properties such as coercivity enhancement by annealing. Consequently, it would be interesting to note the extent to which C_{60} changes this feature. Co/C_{60} trilayers could also be studied to explore the effects of annealing on the magnetic properties. Transport measurements could be carried out at low temperatures with varying the thickness of the metallic layer. Using another molecules can be also used to investigate the magnetic properties before and after annealing. Further, ferromagnetic resonance (FMR) could be carried out investigating the temperature dependent FMR properties such as effective magnetisation (M_{eff}) for Fe/RF-sputtered amorphous carbon and Co/C_{60}. Systematic study using XRD and XRR for Co/C_{60}, Fe/C_{60}, Fe/RF-sputtered a-C and $Fe_xN_{(1-x)}$/RF-sputtered a-C could be also help to provide an explanation as to what is happening to the structure before and after annealing.

REFERENCES

[1] V. Ivanov, T. Aminov, V. Novotortsev, and V. Kalinnikov, "Spintronics and spintronics materials," *Russian Chemical Bulletin*, vol. 53, no. 11, pp. 2357–2405, 2004. 2

[2] N. Morley, A. Rao, D. Dhandapani, M. Gibbs, M. Grell, and T. Richardson, "Room temperature organic spintronics," *Journal of Applied Physics*, vol. 103, no. 7, p. 07F306, 2008. 2

[3] L. Schulz, L. Nuccio, M. Willis, P. Desai, P. Shakya, T. Kreouzis, V. K. Malik, C. Bernhard, F. Pratt, N. Morley, *et al.*, "Engineering spin propagation across a hybrid organic/inorganic interface using a polar layer," *Nature materials*, vol. 10, no. 1, p. 39, 2011. 2, 15

[4] A. J. Drew, J. Hoppler, L. Schulz, F. Pratt, P. Desai, P. Shakya, T. Kreouzis, W. Gillin, A. Suter, N. Morley, *et al.*, "Direct measurement of the electronic spin diffusion length in a fully functional organic spin valve by low-energy muon spin rotation," *Nature materials*, vol. 8, no. 2, p. 109, 2009. 2, 3

[5] M. Wohlgenannt, P. Bobbert, B. Koopmans, and F. Bloom, "Magnetoresistance and spin transport in organic semiconductor devices," in *Organic Spintronics*, pp. 73–142, CRC Press, 2010. 2

[6] A. R. Rocha, V. M. Garcia-Suarez, S. W. Bailey, C. J. Lambert, J. Ferrer, and S. Sanvito, "Towards molecular spintronics," *Nature materials*, vol. 4, no. 4, p. 335, 2005. 2

[7] K. V. Raman, "Interface-assisted molecular spintronics," *Applied Physics Reviews*, vol. 1, no. 3, p. 031101, 2014. 2, 19

[8] K. V. Raman, A. M. Kamerbeek, A. Mukherjee, N. Atodiresei, T. K. Sen, P. Lazić, V. Caciuc, R. Michel, D. Stalke, S. K. Mandal, *et al.*, "Interface-engineered templates for molecular spin memory devices," *Nature*, vol. 493, no. 7433, p. 509, 2013. 2, 3, 15, 57, 133

[9] C. Barraud, C. Deranlot, P. Seneor, R. Mattana, B. Dlubak, S. Fusil, K. Bouzehouane, D. Deneuve, F. Petroff, and A. Fert, "Magnetoresistance in magnetic tunnel junctions grown on flexible organic substrates," *Applied Physics Letters*, vol. 96, no. 7, p. 072502, 2010. 2, 3

[10] S. Parkin, "Flexible giant magnetoresistance sensors," *Applied physics letters*, vol. 69, no. 20, pp. 3092–3094, 1996. 2

[11] F. Yan, G. Xue, and F. Wan, "A flexible giant magnetoresistance sensor prepared completely by electrochemical synthesis," *Journal of Materials Chemistry*, vol. 12, no. 9, pp. 2606–2608, 2002. 2

[12] A. Bedoya-Pinto, M. Donolato, M. Gobbi, L. E. Hueso, and P. Vavassori, "Flexible spintronic devices on kapton," *Applied Physics Letters*, vol. 104, no. 6, p. 062412, 2014. 2

[13] Z. V. Vardeny, A. J. Heeger, and A. Dodabalapur, "Fundamental research needs in organic electronic materials," *Synthetic Metals*, vol. 148, no. 1, pp. 1–3, 2005. 2

[14] A. J. DRew, "Why going organic is good," *Nat. Mater.*, vol. 8, p. 691, 2009. 2

[15] J.-W. Yoo, V. Prigodin, and A. Epstein, "Spintronic applications of organic materials," in *Organic Spintronics*, pp. 143–222, CRC Press, 2010. 2

[16] V. A. Dediu, L. E. Hueso, I. Bergenti, and C. Taliani, "Spin routes in organic semiconductors," *Nature materials*, vol. 8, no. 9, p. 707, 2009. 2

[17] D. Huertas-Hernando, F. Guinea, and A. Brataas, "Spin-orbit coupling in curved graphene, fullerenes, nanotubes, and nanotube caps," *Physical Review B*, vol. 74, no. 15, p. 155426, 2006. 2, 5, 114

[18] I. Bergenti, V. Dediu, M. Prezioso, and A. Riminucci, "Organic spintronics," *Philosophical Transactions of the Royal Society A: Mathematical, Physical and Engineering Sciences*, vol. 369, no. 1948, pp. 3054–3068, 2011. 2

[19] Y. Zhan and M. Fahlman, "The study of organic semiconductor/ferromagnet interfaces in organic spintronics: A short review of recent progress," *Journal of Polymer Science Part B: Polymer Physics*, vol. 50, no. 21, pp. 1453–1462, 2012. 2

[20] V. Dediu, M. Murgia, F. Matacotta, C. Taliani, and S. Barbanera, "Room temperature spin polarized injection in organic semiconductor," *Solid State Communications*, vol. 122, no. 3-4, pp. 181–184, 2002. 2

[21] C. Barraud, P. Seneor, R. Mattana, S. Fusil, K. Bouzehouane, C. Deranlot, P. Graziosi, L. Hueso, I. Bergenti, V. Dediu, *et al.*, "Unravelling the role of the interface for spin injection into organic semiconductors," *Nature Physics*, vol. 6, no. 8, p. 615, 2010. 2, 3, 15, 16, 20, 57, 114

[22] M. Cinchetti, V. A. Dediu, and L. E. Hueso, "Activating the molecular spinterface," *Nature materials*, vol. 16, no. 5, p. 507, 2017. 2

[23] R. Otero, A. V. de Parga, and J. Gallego, "Electronic, structural and chemical effects of charge-transfer at organic/inorganic interfaces," *Surface Science Reports*, vol. 72, no. 3, pp. 105–145, 2017. 3

[24] T.-C. Tseng, C. Urban, Y. Wang, R. Otero, S. L. Tait, M. Alcamí, D. Écija, M. Trelka, J. M. Gallego, N. Lin, *et al.*, "Charge-transfer-induced structural rearrangements at both sides of organic/metal interfaces," *Nature Chemistry*, vol. 2, no. 5, p. 374, 2010. 3

[25] J. B. Torrance, "The difference between metallic and insulating salts of tetracyanoquinodimethone (tcnq): how to design an organic metal," *Accounts of chemical research*, vol. 12, no. 3, pp. 79–86, 1979. 3

[26] P. J. Wong, W. Zhang, K. Wang, G. van der Laan, Y. Xu, W. G. van der Wiel, and M. P. de Jong, "Electronic and magnetic structure of c 60/fe 3 o 4 (001): a hybrid interface for organic spintronics," *Journal of materials chemistry C*, vol. 1, no. 6, pp. 1197–1202, 2013. 3

[27] F. Al MaMari, T. Moorsom, G. Teobaldi, W. Deacon, T. Prokscha, H. Luetkens, S. Lee, G. E. Sterbinsky, D. A. Arena, D. A. MacLaren, *et al.*, "Beating the stoner criterion using molecular interfaces," *Nature*, vol. 524, no. 7563, p. 69, 2015. 3, 14, 58, 65

[28] K. Bairagi, A. Bellec, V. Repain, C. Chacon, Y. Girard, Y. Garreau, J. Lagoute, S. Rousset, R. Breitwieser, Y.-C. Hu, *et al.*, "Tuning the magnetic anisotropy at a molecule-metal interface," *Physical review letters*, vol. 114, no. 24, p. 247203, 2015. 3, 16, 18, 57, 119, 127

[29] S. Mallik, S. Mattauch, M. K. Dalai, T. Brückel, and S. Bedanta, "Effect of magnetic fullerene on magnetization reversal created at the fe/c 60 interface," *Scientific reports*, vol. 8, no. 1, p. 5515, 2018. 3

[30] T. L. A. Tran, D. Cakır, P. J. Wong, A. B. Preobrajenski, G. Brocks, W. G. van der Wiel, and M. P. de Jong, "Magnetic properties of bcc-fe (001)/c 60 interfaces for organic spintronics," *ACS applied materials & interfaces*, vol. 5, no. 3, pp. 837–841, 2013. 3, 58

[31] T. L. A. Tran, P. K. J. Wong, M. P. de Jong, W. G. van der Wiel, Y. Zhan, and M. Fahlman, "Hybridization-induced oscillatory magnetic polarization of c 60 orbitals at the c 60/fe (001) interface," *Applied physics letters*, vol. 98, no. 22, p. 222505, 2011. 3, 57

[32] T. Moorsom, M. Wheeler, T. M. Khan, F. Al MaMari, C. Kinane, S. Langridge, A. Bedoya-Pinto, L. Hueso, G. Teobaldi, V. K. Lazarov, *et al.*, "Spin-polarized electron transfer in ferromagnet/c 60 interfaces," *Physical Review B*, vol. 90, no. 12, p. 125311, 2014. 3, 17, 18, 57, 65, 119

[33] Y. S. Dedkov and M. Fonin, "Electronic and magnetic properties of the graphene–ferromagnet interface," *New Journal of Physics*, vol. 12, no. 12, p. 125004, 2010. 3

[34] O. Céspedes, M. Ferreira, S. Sanvito, M. Kociak, and J. Coey, "Contact induced magnetism in carbon nanotubes," *Journal of Physics: Condensed Matter*, vol. 16, no. 10, p. L155, 2004. 3, 4, 15, 57

[35] A. Ōya and H. Marsh, "Phenomena of catalytic graphitization," *Journal of Materials Science*, vol. 17, no. 2, pp. 309–322, 1982. 4

[36] A. Ōya and S. Ōtani, "Catalytic graphitization of carbons by various metals," *Carbon*, vol. 17, no. 2, pp. 131–137, 1979. 4

[37] F. Derbyshire, A. Presland, and D. Trimm, "Graphite formation by the dissolutionprecipitation of carbon in cobalt, nickel and iron," *Carbon*, vol. 13, no. 2, pp. 111–113, 1975. 4

[38] F. Derbyshire and D. Trimm, "Kinetics of the deposition of pyrolytic carbon on nickel," *Carbon*, vol. 13, no. 3, pp. 189–192, 1975. 4

[39] G. Nover, J. Stoll, and H. BGR, "Graphitisation of carbon-ap, t-laboratory experiment," in *Protocol on the 19th Colloquium" Electromagnetic Depth Research", German Geophysical Society*, 2001. 4

[40] K. Oohashi, T. Hirose, and T. Shimamoto, "Shear-induced graphitization of carbonaceous materials during seismic fault motion: Experiments and possible implications for fault mechanics," *Journal of Structural Geology*, vol. 33, no. 6, pp. 1122–1134, 2011. 4

[41] A. Ramirez, T. Itoh, and R. Sinclair, "Crystallization of amorphous carbon thin films in the presence of magnetic media," *Journal of applied physics*, vol. 85, no. 3, pp. 1508–1513, 1999. 4

[42] T. Konno and R. Sinclair, "Crystallization of amorphous carbon in carboncobalt layered thin films," *Acta metallurgica et materialia*, vol. 43, no. 2, pp. 471–484, 1995. 4, 81

[43] S. Tajima and S. Hirano, "Synthesis and properties of fe 3 c film by rf magnetron sputtering," *Journal of materials science*, vol. 28, no. 10, pp. 2715–2720, 1993. 4, 68

[44] A. Wu, D. Liu, L. Tong, L. Yu, and H. Yang, "Magnetic properties of nanocrystalline fe/fe 3 c composites," *CrystEngComm*, vol. 13, no. 3, pp. 876–882, 2011. 4, 65

[45] R. Sinclair, T. Itoh, and R. Chin, "In situ tem studies of metal–carbon reactions," *Microscopy and Microanalysis*, vol. 8, no. 4, pp. 288–304, 2002. 4

[46] M. Humphries, "Rare earth elements: the global supply chain," 2013. 4, 76

[47] N. Poudyal and J. P. Liu, "Advances in nanostructured permanent magnets research," *Journal of Physics D: Applied Physics*, vol. 46, no. 4, p. 043001, 2012. 4, 5, 77, 78

[48] X. Crispin, V. Geskin, A. Crispin, J. Cornil, R. Lazzaroni, W. R. Salaneck, and J.-L. Bredas, "Characterization of the interface dipole at organic/metal interfaces," *Journal of the American Chemical Society*, vol. 124, no. 27, pp. 8131–8141, 2002. 4, 5

[49] C.-B. Rong, V. Nandwana, N. Poudyal, J. P. Liu, M. E. Kozlov, R. H. Baughman, Y. Ding, and Z. L. Wang, "Bulk fept-based nanocomposite magnets with enhanced exchange coupling," *Journal of Applied Physics*, vol. 102, no. 2, p. 023908, 2007. 5

[50] D. Li, Y. Li, D. Pan, Z. Zhang, and C.-J. Choi, "Prospect and status of iron-based rare-earth-free permanent magnetic materials," *Journal of Magnetism and Magnetic Materials*, 2018. 5, 92

[51] M. Sagawa, S. Fujimura, N. Togawa, H. Yamamoto, and Y. Matsuura, "New material for permanent magnets on a base of nd and fe," *Journal of Applied Physics*, vol. 55, no. 6, pp. 2083–2087, 1984. 5

[52] M. Kitada and N. Shimizu, "Magnetic properties of sputtered co-pt thin films," *Journal of applied physics*, vol. 54, no. 12, pp. 7089–7094, 1983. 5

[53] M. L. Plumer, J. Van Ek, and D. Weller, *The physics of ultra-high-density magnetic recording*, vol. 41. Springer Science & Business Media, 2012. 5

[54] S. Vorobiov, I. Lytvynenko, T. Hauet, M. Hehn, D. Derecha, and A. Chornous, "The effect of annealing on magnetic properties of co/gd multilayers," *Vacuum*, vol. 120, pp. 9–12, 2015. 5

[55] T. Y. Lee, Y. Chan Won, D. Su Son, S. Ho Lim, and S.-R. Lee, "Effects of co layer thickness and annealing temperature on the magnetic properties of inverted [pt/co] multilayers," *Journal of Applied Physics*, vol. 114, no. 17, p. 173909, 2013. 5

[56] S. H. Vijapur, D. Wang, and G. G. Botte, "The growth of transparent amorphous carbon thin films from coal," *Carbon*, vol. 54, pp. 22–28, 2013. 5, 41, 82, 143

[57] A. V. Khaetskii and Y. V. Nazarov, "Spin-flip transitions between zeeman sublevels in semiconductor quantum dots," *Physical Review B*, vol. 64, no. 12, p. 125316, 2001. 5, 114

[58] F. Al MaMari, M. Rogers, S. Alghamdi, T. Moorsom, S. Lee, T. Prokscha, H. Luetkens, M. Valvidares, G. Teobaldi, M. Flokstra, *et al.*, "Emergent magnetism at transition-metal–nanocarbon interfaces," *Proceedings of the National Academy of Sciences*, vol. 114, no. 22, pp. 5583–5588, 2017. 9, 14, 16, 79, 109

[59] R. King, "Carbon, part 2: diamond," *Geology Today*, vol. 24, no. 3, pp. 112–118, 2008. 9

[60] X. Feng, W. Mi, and H. Bai, "Investigation of structure and magnetic properties of the as-deposited and post-annealed iron nitride films by reactive facing-target sputtering," *Applied Surface Science*, vol. 257, no. 16, pp. 7320–7325, 2011. 9, 10, 11, 96, 100, 111

[61] D. Chung, "Review graphite," *Journal of materials science*, vol. 37, no. 8, pp. 1475–1489, 2002. 9

[62] D. P. Manage, *Structural and optical characterization of hydrogenated amorphous carbon thin films.* University of Toronto, 2000. 9, 10, 12

[63] M. S. Dresselhaus, G. Dresselhaus, and P. C. Eklund, *Science of fullerenes and carbon nanotubes: their properties and applications*. Elsevier, 1996. 9

[64] R. Silva and S. Silva, *Properties of amorphous carbon*. No. 29, Iet, 2003. 9, 10, 34

[65] J. Robertson, "Diamond-like amorphous carbon," *Materials science and engineering: R: Reports*, vol. 37, no. 4-6, pp. 129–281, 2002. 10, 12, 34, 82

[66] H. W. Kroto, J. R. Heath, S. C. O'Brien, R. F. Curl, and R. E. Smalley, "C 60: Buckminsterfullerene," *Nature*, vol. 318, no. 6042, p. 162, 1985. 13

[67] R. Lin, F. Wang, M. Wohlgenannt, C. He, X. Zhai, and Y. Suzuki, "Organic spin-valves based on fullerene c 60," *Synthetic Metals*, vol. 161, no. 7-8, pp. 553–557, 2011. 13

[68] S. Braun, W. R. Salaneck, and M. Fahlman, "Energy-level alignment at organic/metal and organic/organic interfaces," *Advanced materials*, vol. 21, no. 14-15, pp. 1450–1472, 2009. 13

[69] T. Ohno, Y. Chen, S. Harvey, G. Kroll, J. Weaver, R. Haufler, and R. Smalley, "C 60 bonding and energy-level alignment on metal and semiconductor surfaces," *Physical Review B*, vol. 44, no. 24, p. 13747, 1991. 13, 14

[70] M. C. Wheeler, *Manipulation of fullerene C60 spintronic devices via ferromagnetic resonance*. PhD thesis, University of Leeds, 2014. 13, 14, 34, 38, 39, 40, 43, 45, 114, 115, 129, 130

[71] P. A. Heiney, J. E. Fischer, A. R. McGhie, W. J. Romanow, A. M. Denenstein, J. P. McCauley Jr, A. B. Smith, and D. E. Cox, "Orientational ordering transition in solid c 60," *Physical Review Letters*, vol. 66, no. 22, p. 2911, 1991. 14

[72] L.-S. Wang, J. Conceicao, C. Jin, and R. Smalley, "Threshold photodetachment of cold c- 60," *Chemical physics letters*, vol. 182, no. 1, pp. 5–11, 1991. 14

[73] R. Lof, M. Van Veenendaal, B. Koopmans, H. Jonkman, and G. Sawatzky, "Band gap, excitons, and coulomb interaction in solid c 60," *Physical Review Letters*, vol. 68, no. 26, p. 3924, 1992. 14

[74] J. Weaver, J. L. Martins, T. Komeda, Y. Chen, T. Ohno, G. Kroll, N. Troullier, R. Haufler, and R. Smalley, "Electronic structure of solid c 60: experiment and theory," *Physical review letters*, vol. 66, no. 13, p. 1741, 1991. 14

[75] P.-M. Allemand, K. C. Khemani, A. Koch, F. Wudl, K. Holczer, S. Donovan, G. Grüner, and J. D. Thompson, "Organic molecular soft ferromagnetism in a fullerene c 60," *Science*, vol. 253, no. 5017, pp. 301–302, 1991. 14

[76] B. Narymbetov, A. Omerzu, V. V. Kabanov, M. Tokumoto, H. Kobayashi, and D. Mihailovic, "Origin of ferromagnetic exchange interactions in a fullerene–organic compound," *Nature*, vol. 407, no. 6806, p. 883, 2000. 14

[77] S. Steil, N. Großmann, M. Laux, A. Ruffing, D. Steil, M. Wiesenmayer, S. Mathias, O. L. Monti, M. Cinchetti, and M. Aeschlimann, "Spin-dependent trapping of electrons at spinterfaces," *Nature Physics*, vol. 9, no. 4, p. 242, 2013. 15

[78] D. Gatteschi, "Molecular magnetism: A basis for new materials," *Advanced Materials*, vol. 6, no. 9, pp. 635–645, 1994. 15

[79] J. S. Miller and D. Gatteschi, "Molecule-based magnets," *Chemical Society Reviews*, vol. 40, no. 6, pp. 3065–3066, 2011. 15

[80] M. Verdaguer, "Molecular electronics emerges from molecular magnetism," *Science*, vol. 272, no. 5262, pp. 698–699, 1996. 15

[81] H. M. McConnell, "Ferromagnetism in solid free radicals," *The Journal of Chemical Physics*, vol. 39, no. 7, pp. 1910–1910, 1963. 15

[82] J. S. Miller, A. J. Epstein, and W. M. Reiff, "Ferromagnetic molecular charge-transfer complexes," *Chemical Reviews*, vol. 88, no. 1, pp. 201–220, 1988. 16

[83] S. Sanvito, "Molecular spintronics: The rise of spinterface science," *Nature Physics*, vol. 6, no. 8, p. 562, 2010. 16, 19, 20, 114, 115, 117

[84] V. A. Dediu, "Organic spintronics: Inside the interface," *Nature Physics*, vol. 9, no. 4, p. 210, 2013. 16

[85] M. Gruber, F. Ibrahim, S. Boukari, L. Joly, V. Da Costa, M. Studniarek, M. Peter, H. Isshiki, H. Jabbar, V. Davesne, *et al.*, "Spin-dependent hybridization between molecule and metal at room temperature through interlayer exchange coupling," *Nano letters*, vol. 15, no. 12, pp. 7921–7926, 2015. 16, 18

[86] N. Morley, A. Drew, H. Zhang, K. Scott, S. Hudziak, and D. Morgan, "Study of the magnetic–alq3 interface in organic spin-valves," *Applied Surface Science*, vol. 313, pp. 850–857, 2014. 17, 18

[87] N. Morley, R. Dost, A. Lingam, and A. Barlow, "Investigations of the polymer/magnetic interface of organic spin-valves," *Applied Surface Science*, vol. 359, pp. 704–713, 2015. 17

[88] D. Langreth, B. I. Lundqvist, S. D. Chakarova-Käck, V. Cooper, M. Dion, P. Hyldgaard, A. Kelkkanen, J. Kleis, L. Kong, S. Li, *et al.*, "A density functional for sparse matter," *Journal of Physics: Condensed Matter*, vol. 21, no. 8, p. 084203, 2009. 19

[89] N. Atodiresei, V. Caciuc, P. Lazic, and S. Blügel, "Chemical and van der waals interactions at hybrid organic-metal interfaces," -, 2000. 19

[90] J. B. Neaton, M. S. Hybertsen, and S. G. Louie, "Renormalization of molecular electronic levels at metal-molecule interfaces," *Physical review letters*, vol. 97, no. 21, p. 216405, 2006. 19, 129

[91] F. A. Al MaMari, *Emergent Spin Ordering at C_{60} interfaces*. PhD thesis, University of Leeds, 2016. 21, 34, 52, 74, 115

[92] J.-H. Park, *Magnetoresistive devices with perpendicular magnetic anisotropy for spin-torque driven applications*. PhD thesis, Carnegie Mellon University, 2010. 22

[93] R. C. Temple, *Spin accumulation and transport studied in double magnetic tunnel junctions*. PhD thesis, University of Leeds, 2014. 22

[94] S. Blundell, "Magnetism in condensed matter: oxford master series," *Condensed Matter Physics (Oxford Series Publications, 2001)*, 2001. 22, 24, 25, 28, 29

[95] B. Cullity and C. Graham, "Introduction to magnetic materials, a john wiley & sons," *Inc., NJ*, 2009. 22

[96] P. M. Shepley, *Effect of piezoelectric strain on the magnetic properties of Pt/Co thin films*. PhD thesis, University of Leeds, 2015. 23, 53

[97] N. A. Spaldin and N. D. Mathur, "Magnetic materials: fundamentals and device applications," *Physics Today*, vol. 56, no. 12, pp. 62–63, 2003. 23

[98] H. Xing, *Perpendicular exchange bias in ferromagnetic/antiferromagnetic multilayers and magnetization switching*. University of Houston, 2009. 23

[99] M. Johnson, P. Bloemen, F. Den Broeder, and J. De Vries, "Magnetic anisotropy in metallic multilayers," *Reports on Progress in Physics*, vol. 59, no. 11, p. 1409, 1996. 23

[100] J. M. Coey, *Magnetism and magnetic materials*. Cambridge university press, 2010. 25

[101] E. C. Stoner, "Collective electron ferronmagnetism," *Proceedings of the Royal Society of London. Series A. Mathematical and Physical Sciences*, vol. 165, no. 922, pp. 372–414, 1938. 25

[102] S. Von Oehsen, *Spin-polarized Currents for Spintronic Devices: Point-contact Andreev Reflection and Spin Filters*. Cuvillier Verlag, 2007. 26, 27

[103] J. Janak, "Uniform susceptibilities of metallic elements," *Physical Review B*, vol. 16, no. 1, p. 255, 1977. 27

[104] M. Ghezelbash, S. Darbani, A. Majd, and A. Ghasemi, "Temperature dependence of magnetic hysteresis loop of ndfeb with uniaxial anisotropy by libs technique," *Journal of Superconductivity and Novel Magnetism*, vol. 30, no. 7, pp. 1893–1898, 2017. 30

[105] K. Seshan, "Handbook of thin film deposition techniques principles, methods, equipment and applications," *Second Editon*, 2002. 32, 33

[106] R. Gupta, A. Tayal, S. Amir, M. Gupta, A. Gupta, M. Horisberger, and J. Stahn, "Formation of iron nitride thin films with al and ti additives," *Journal of Applied Physics*, vol. 111, no. 10, p. 103520, 2012. 33, 98

[107] K. Ellmer, "Magnetron sputtering of transparent conductive zinc oxide: relation between the sputtering parameters and the electronic properties," *Journal of Physics D: Applied Physics*, vol. 33, no. 4, p. R17, 2000. 34

[108] J. D. Lamb and J. A. Woollam, "Dielectric properties of diamondlikecarbon prepared by rf plasma deposition," *Journal of applied physics*, vol. 57, no. 12, pp. 5420–5423, 1985. 34

[109] P. Davidse, "Theory and practice of rf sputtering," *Vacuum*, vol. 17, no. 3, pp. 139–145, 1967. 34

[110] E. Williams, "An introduction to sputtering of magnetic and magneto-optic thin films for data recording," *Journal of magnetism and magnetic materials*, vol. 95, no. 3, pp. 356–364, 1991. 34, 35

[111] D. Maurya, A. Sardarinejad, and K. Alameh, "Recent developments in rf magnetron sputtered thin films for ph sensing applicationsan overview," *Coatings*, vol. 4, no. 4, pp. 756–771, 2014. 35

[112] B. Bhushan, J. V. Coe Jr, and B. Gupta, "Method for coating fullerene materials for tribology," Sept. 24 1996. US Patent 5,558,903. 37

[113] R. Feidenhans, "Surface structure determination by x-ray diffraction," *Surface Science Reports*, vol. 10, no. 3, pp. 105–188, 1989. 39

[114] E. Lifshin, *X-ray Characterization of Materials*, vol. 38. Wiley Online Library, 1999. 39

[115] J. Als-Nielsen and D. McMorrow, *Elements of modern X-ray physics*. John Wiley & Sons, 2011. 40

[116] U. Pietsch, V. Holy, and T. Baumbach, *High-resolution X-ray scattering: from thin films to lateral nanostructures*. Springer Science & Business Media, 2013. 40

[117] M. Woolfson, *An introduction to X-ray crystallography*. Cambridge University Press, 1997. 40

[118] M. Sugawara, M. Kondo, S. Yamazaki, and K. Nakajima, "Exact determination of superlattice structures by small-angle x-ray diffraction method," *Applied physics letters*, vol. 52, no. 9, pp. 742–744, 1988. 41

[119] M. Wormington, C. Panaccione, K. M. Matney, and D. K. Bowen, "Characterization of structures from x-ray scattering data using genetic algorithms," *Philosophical Transactions of the Royal Society of London. Series A: Mathematical, Physical and Engineering Sciences*, vol. 357, no. 1761, pp. 2827–2848, 1999. 41

[120] C. V. Raman, "A change of wave-length in light scattering," *Nature*, vol. 121, no. 3051, p. 619, 1928. 42

[121] D. W. Hahn, "Raman scattering theory," *Department of Mechanical and Aerospace Engineering, University of Florida*, 2007. 42, 43, 48

[122] A. C. Ferrari and J. Robertson, "Raman spectroscopy of amorphous, nanostructured, diamond–like carbon, and nanodiamond," *Philosophical Transactions of the Royal Society of London. Series A: Mathematical, Physical and Engineering Sciences*, vol. 362, no. 1824, pp. 2477–2512, 2004. 44, 47, 79

[123] A. C. Ferrari and J. Robertson, "Resonant raman spectroscopy of disordered, amorphous, and diamondlike carbon," *Physical Review B*, vol. 64, no. 7, p. 075414, 2001. 45, 46, 48

[124] A. C. Ferrari and J. Robertson, "Interpretation of raman spectra of disordered and amorphous carbon," *Physical review B*, vol. 61, no. 20, p. 14095, 2000. 46, 47, 49, 50, 143

[125] H. Pang, X. Wang, G. Zhang, H. Chen, G. Lv, and S. Yang, "Characterization of diamond-like carbon films by sem, xrd and raman spectroscopy," *Applied Surface Science*, vol. 256, no. 21, pp. 6403–6407, 2010. 48

[126] H. R. P. Cardoso, T. Falcade, S. R. Kunst, and C. F. Malfatti, "Corrosion and wear resistance of carbon films obtained by electrodeposition on ferritic stainless steel," *Materials Research*, vol. 18, no. 2, pp. 292–297, 2015. 48, 90

[127] K. Wasa, M. Kitabatake, and H. Adachi, *Thin film materials technology: sputtering of control compound materials*. Springer Science & Business Media, 2004. 50

[128] M. Ali, *Growth and study of magnetostrictive FeSiBC thin films for device applications*. PhD thesis, University of Sheffield, 1999. 50

[129] Q. A. Abbas, N. A. Morley, A. Johansson, and T. Thomson, "Influence of ar pressure on the magnetic properties of amorphous fegasib thin films," *IEEE Transactions on Magnetics*, vol. 53, no. 11, pp. 1–4, 2017. 50

[130] A. Ferrari, B. Kleinsorge, N. Morrison, A. Hart, V. Stolojan, and J. Robertson, "Stress reduction and bond stability during thermal annealing of tetrahedral amorphous carbon," *Journal of applied physics*, vol. 85, no. 10, pp. 7191–7197, 1999. 50, 80, 90

[131] M. Tinkham, "Introduction to superconductivity ch. 3 mcgraw-hill," *Inc., New York*, 1996. 51

[132] C. Graham, "High-sensitivity magnetization measurements," *Journal of Materials Sciences and Technology,*, no. 2, pp. 97–101, 2000. 52

[133] J. Clarke and A. I. Braginski, *The SQUID handbook*, vol. 1. Wiley Online Library, 2004. 52

[134] G. Aviv, "Squids-superconducting quantum interference devices," *Department of Physics, Ben-Gurion University of the Negev, Experimental physics course*, 2008. 52

[135] J. Kerr, "Xliii. on rotation of the plane of polarization by reflection from the pole of a magnet," *The London, Edinburgh, and Dublin Philosophical Magazine and Journal of Science*, vol. 3, no. 19, pp. 321–343, 1877. 52

[136] J. Ekin, *Experimental techniques for low-temperature measurements: cryostat design, material properties and superconductor critical-current testing*. Oxford university press, 2006. 53

[137] V. Al'tov, *Stabilization of superconducting magnetic systems*. Springer Science & Business Media, 2013. 53

[138] Rose-Innes, "Low temperature laboratory techniques," -, 1973. 54

[139] M. S. Ferreira and S. Sanvito, "Contact-induced spin polarization in carbon nanotubes," *Physical Review B*, vol. 69, no. 3, p. 035407, 2004. 57

[140] S. Kobe, E. Sarantopoulou, G. Dražić, J. Kovač, M. Janeva, Z. Kollia, and A. Cefalas, "Growth of crystalline/amorphous biphase sm–fe–ta–n magnetic nanodroplets," *Applied Surface Science*, vol. 254, no. 4, pp. 1027–1031, 2007. 58

[141] C.-F. Huang, A.-C. Sun, H. Chang, F.-T. Yuan, S. Chang, and W. Chang, "Improved perpendicular magnetic anisotropy of pr–fe–b films with ta underlayer," *Journal of Alloys and Compounds*, vol. 584, pp. 185–189, 2014. 58

[142] A. C. Finkel, N. Reeves-McLaren, and N. Morley, "Influence of soft magnetic underlayers on the magnetic properties of co90fe10 films," *Journal of Magnetism and Magnetic Materials*, vol. 357, pp. 87–92, 2014. 58

[143] A. Javed, N. Morley, and M. Gibbs, "Thickness dependence of magnetic and structural properties in fe 80 ga 20 thin films," *Journal of Applied Physics*, vol. 107, no. 9, p. 09A944, 2010. 60

[144] S. Amir, M. Gupta, A. Gupta, K. Ambika, and J. Stahn, "Silicide layer formation in evaporated and sputtered fe/si multilayers: X-ray and neutron reflectivity study," *Applied Surface Science*, vol. 277, pp. 182–185, 2013. 60

[145] Y. Cao and C. Zhou, "Thickness dependence of surface roughness and magnetic properties of fenicr thin films," *Journal of Magnetism and Magnetic Materials*, vol. 333, pp. 1–7, 2013. 63, 69

[146] A. Saadi, R. Moubah, H. Lassri, A. El Amiri, Y. Boughaleb, I. Bimaghra, and E. Hlil, "Magnetic and electronic properties of fe/c multilayers: Interfacial effects," *Physica A: Statistical Mechanics and its Applications*, vol. 516, pp. 340–345, 2019. 64

[147] R. Krishnan, H. Gupta, C. Sella, and M. Kaabouchi, "Magnetic and structural studies in sputtered ni/c, co/c and fe/c multilayers," *Journal of Magnetism and Magnetic Materials*, vol. 93, pp. 174–178, 1991. 65, 66, 68, 73, 75

[148] X. Tang, L. Jin, R. Wei, X. Zhu, J. Yang, J. Dai, W. Song, X. Zhu, and Y. Sun, "High-coercivity cofe2o4 thin films on si substrates by sol-gel," *Journal of Magnetism and Magnetic Materials*, vol. 422, pp. 255–261, 2017. 66

[149] N. Nakayama, T. Katamoto, T. Shinjo, and T. Takada, "Structure of fe-c multilayered films (commemoration issue dedicated to professor toshio takada on the occasion of his retirement)," 1986. 66

[150] M. Georgieva, N. Telling, P. Grundy, C. Faunce, and G. Jones, "Magnetically soft, high moment grain-refined fe films: Application to magnetic tunnel junctions," *Journal of applied physics*, vol. 96, no. 5, pp. 2923–2926, 2004. 67, 116

[151] X. Wang, W. Zheng, H. Tian, S. Yu, W. Xu, S. Meng, X. He, J. Han, C. Sun, and B. Tay, "Growth, structural, and magnetic properties of iron nitride thin films deposited by dc magnetron sputtering," *Applied Surface Science*, vol. 220, no. 1-4, pp. 30–39, 2003. 67, 99, 116

[152] H. Baker and H. Okamoto, "Asm handbook. vol. 3. alloy phase diagrams," *ASM International, Materials Park, Ohio 44073-0002, USA, 1992. 501*, 1992. 68

[153] G. Palasantzas, Y.-P. Zhao, J. T. M. De Hosson, and G.-C. Wang, "Roughness effects on magnetic properties of thin films," *Physica B: Condensed Matter*, vol. 283, no. 1-3, pp. 199–202, 2000. 69

[154] A. Javed, N. Morley, and M. Gibbs, "Effect of growth parameters on the structure and magnetic properties of thin polycrystalline fe films fabricated on

si¡100¿ substrates," *Applied Surface Science*, vol. 257, no. 13, pp. 5586–5590, 2011. 73

[155] Y. Jiang, M. Al Mehedi, E. Fu, Y. Wang, L. F. Allard, and J.-P. Wang, "Synthesis of fe 16 n 2 compound free-standing foils with 20 mgoe magnetic energy product by nitrogen ion-implantation," *Scientific reports*, vol. 6, p. 25436, 2016. 76, 92, 96

[156] C. Coutts, M. Arora, R. Hübner, B. Heinrich, and E. Girt, "Magnetic properties of co/ni grain boundaries after annealing," *AIP Advances*, vol. 8, no. 5, p. 056318, 2018. 83

[157] G. Katona, I. Vladymyrskyi, I. Makogon, S. Sidorenko, F. Kristály, L. Daróczi, A. Csik, A. Liebig, G. Beddies, M. Albrecht, *et al.*, "Grain boundary diffusion induced reaction layer formation in fe/pt thin films," *Applied Physics A*, vol. 115, no. 1, pp. 203–211, 2014. 83

[158] R. Brajpuriya, S. Tripathi, A. Sharma, S. Chaudhari, D. Phase, A. Gupta, T. Shripathi, W. Leitenberger, U. Pietsch, and N. Laxmi, "Temperature dependent energy-dispersive x-ray diffraction and magnetic study of fe/al interface," *Applied surface science*, vol. 253, no. 21, pp. 8584–8587, 2007. 86

[159] J. Coey, "The magnetization of bulk α fe 16 n 2," *Journal of Applied Physics*, vol. 76, no. 10, pp. 6632–6636, 1994. 92

[160] K. H. Jack, "The iron-nitrogen system: the preparation and the crystal structures of nitrogen-austenite (γ) and nitrogen-martensite (α'), " *Proc. R. Soc. Lond. A*, vol. 208, no. 1093, pp. 200–215, 1951. 92

[161] H. Jacobs, A. Leineweber, and W. A. Kockelmann, "Order-disorder-phenomena in the ε-phase of the system fe/n," in *Materials Science Forum*, vol. 325, pp. 117–124, Trans Tech Publ, 2000. 92

[162] G.-K. Li, Y. Liu, R.-B. Zhao, J.-J. Shen, S. Wang, P.-J. Shan, C.-M. Zhen, and D.-L. Hou, "Crystallographic phases and magnetic properties of iron nitride films," *Thin Solid Films*, vol. 589, pp. 22–26, 2015. 92, 93, 96, 102, 106

[163] Z. Tao, X. Cui, R. Zhang, X. Xiu, Z. Xie, and Y. Zheng, "Ferromagnetic fe3n films grown on gan (0 0 0 2) substrates by mocvd," *Journal of Crystal Growth*, vol. 312, no. 9, pp. 1525–1528, 2010. 92, 102

[164] J. Coey and P. Smith, "Magnetic nitrides," *Journal of magnetism and magnetic materials*, vol. 200, no. 1-3, pp. 405–424, 1999. 92, 102

[165] Y. Zhang, Y. Xie, Y. Zhou, X. Wang, and K. Pan, "Well dispersed fe 2 n nanoparticles on surface of nitrogen-doped reduced graphite oxide for highly efficient electrochemical hydrogen evolution," *Journal of Materials Research*, vol. 32, no. 9, pp. 1770–1776, 2017. 94, 95

[166] W. Zhong, B. Tay, S. Lau, X. Sun, S. Li, and C. Sun, "Structural and magnetic properties of iron-nitride thin films deposited using a filtered cathodic vacuum arc," *Thin Solid Films*, vol. 478, no. 1-2, pp. 61–66, 2005. 99

[167] V. H. Babu, J. Rajeswari, S. Venkatesh, and G. Markandeyulu, "Effect of thickness on structural and magnetic properties in nanocrystalline fe–n thin films," *Journal of Magnetism and Magnetic Materials*, vol. 339, pp. 1–5, 2013. 100, 102

[168] G. Cui, X. Wei, E. A. Olevsky, R. M. German, and J. Chen, "Preparation of high performance bulk fe–n alloy by spark plasma sintering," *Materials & Design*, vol. 90, pp. 115–121, 2016. 105

[169] H. Naganuma, R. Nakatani, Y. Endo, Y. Kawamura, and M. Yamamoto, "Magnetic and electrical properties of iron nitride films containing both amorphous matrices and nanocrystalline grains," *Science and Technology of Advanced Materials*, vol. 5, no. 1-2, p. 101, 2004. 107

[170] C.-W. Tsai, M.-H. Tu, C.-J. Chen, T.-F. Hung, R.-S. Liu, W.-R. Liu, M.-Y. Lo, Y.-M. Peng, L. Zhang, J. Zhang, *et al.*, "Nitrogen-doped graphene nanosheet-supported non-precious iron nitride nanoparticles as an efficient electrocatalyst for oxygen reduction," *Rsc Advances*, vol. 1, no. 7, pp. 1349–1357, 2011. 108

[171] T. L. A. Tran, "Spintronics using c 60 fullerenes: Interface and devices," *PhD thesis*, 2013. 114

[172] M. Cadek, O. Vostrowsky, and A. Hirsch, "Carbon, 7. fullerenes and carbon nanomaterials," *Ullmann's Encyclopedia of Industrial Chemistry*, 2000. 121, 125

[173] W. David, R. Ibberson, T. Dennis, J. Hare, and K. Prassides, "Structural phase transitions in the fullerene c 60," *EPL (Europhysics Letters)*, vol. 18, no. 3, p. 219, 1992. 121, 125

[174] C. Kittel, P. McEuen, and P. McEuen, *Introduction to solid state physics*, vol. 8. Wiley New York, 1976. 123

[175] M. Gruber, F. Ibrahim, S. Boukari, H. Isshiki, L. Joly, M. Peter, M. Studniarek, V. Da Costa, H. Jabbar, V. Davesne, *et al.*, "Exchange bias and room-temperature magnetic order in molecular layers," *Nature materials*, vol. 14, no. 10, p. 981, 2015. 129

[176] J. S. Jiang, S. Bader, H. Kaper, G. Leaf, R. D. Shull, A. J. Shapiro, V. Gornakov, V. I. Nikitenko, C. Platt, A. Berkowitz, *et al.*, "Rotational hysteresis of exchange-spring magnets," *Journal of Physics D: Applied Physics*, vol. 35, no. 19, p. 2339, 2002. 129, 145

[177] E. E. Fullerton, J. Jiang, and S. Bader, "Hard/soft magnetic heterostructures: model exchange-spring magnets," *Journal of Magnetism and Magnetic Materials*, vol. 200, no. 1-3, pp. 392–404, 1999. 129, 145

[178] A. Bill and H. Braun, "Magnetic properties of exchange springs," *Journal of magnetism and magnetic materials*, vol. 272, pp. 1266–1267, 2004. 129, 145

[179] G. Stenning, G. Bowden, P. de Groot, G. van der Laan, A. Figueroa, P. Bencok, P. Steadman, and T. Hesjedal, "Exchange spring switching in er-doped dyfe 2/yfe 2 magnetic thin films," *Physical Review B*, vol. 92, no. 10, p. 104404, 2015. 129

[180] U. Nowak, K.-D. Usadel, J. Keller, P. Miltényi, B. Beschoten, and G. Güntherodt, "Domain state model for exchange bias. i. theory," *Physical review B*, vol. 66, no. 1, p. 014430, 2002. 130, 136, 145

[181] J. Keller, P. Miltényi, B. Beschoten, G. Güntherodt, U. Nowak, and K.-D. Usadel, "Domain state model for exchange bias. ii. experiments," *Physical review B*, vol. 66, no. 1, p. 014431, 2002. 130, 136, 145

[182] A. Hoffmann, "Symmetry driven irreversibilities at ferromagnetic-antiferromagnetic interfaces," *Physical review letters*, vol. 93, no. 9, p. 097203, 2004. 130, 136, 145

[183] A.-D. Vu, J. Coraux, G. Chen, A. NDiaye, A. Schmid, and N. Rougemaille, "Unconventional magnetisation texture in graphene/cobalt hybrids," *Scientific reports*, vol. 6, p. 24783, 2016. 131

[184] R. Mantovan, M. Georgieva, M. Perego, H. Lu, S. Cocco, A. Zenkevich, G. Scarel, and M. Fanciulli, "Atomic layer deposition of magnetic thin films," *ACTA PHYSICA POLONICA SERIES A*, vol. 112, no. 6, p. 1271, 2007. 131

[185] J. Jo, J. Byun, I. Oh, J. Park, M.-J. Jin, B.-C. Min, J. Lee, and J.-W. Yoo, "Molecular tunability of magnetic exchange bias and asymmetrical magnetotransport in metalloporphyrin/co hybrid bilayers," *ACS nano*, vol. 13, no. 1, pp. 894–903, 2018. 133, 136, 138, 141, 145

[186] S. Boukari, H. Jabbar, F. Schleicher, M. Gruber, G. Avedissian, J. Arabski, V. Da Costa, G. Schmerber, P. Rengasamy, B. Vileno, *et al.*, "Disentangling magnetic hardening and molecular spin chain contributions to exchange bias in ferromagnet/molecule bilayers," *Nano letters*, vol. 18, no. 8, pp. 4659–4663, 2018. 133

[187] B. R. Gautam, T. D. Nguyen, E. Ehrenfreund, and Z. V. Vardeny, "Magnetic field effect spectroscopy of c 60-based films and devices," *Journal of Applied Physics*, vol. 113, no. 14, p. 143102, 2013. 135

[188] W. H. Meiklejohn and C. P. Bean, "New magnetic anisotropy," *Physical Review*, vol. 105, no. 3, p. 904, 1957. 135

[189] Y. Pansong and C. Sirisathitkul, "Anisotropic magnetoresistance of cobalt films prepared by thermal evaporation," *Walailak Journal of Science and Technology (WJST)*, vol. 2, no. 1, pp. 71–80, 2011. 136

[190] K. Meng, J. Xiao, Y. Wu, J. Miao, X. Xu, J. Zhao, and Y. Jiang, "Hybrid magnetoresistance in pt-based multilayers: Effect originated from strong interfacial spin-orbit coupling," *Scientific reports*, vol. 6, p. 20522, 2016. 136

[191] F. Radu, M. Etzkorn, R. Siebrecht, T. Schmitte, K. Westerholt, and H. Zabel, "Interfacial domain formation during magnetization reversal in exchange-biased coo/co bilayers," *Physical Review B*, vol. 67, no. 13, p. 134409, 2003. 136

[192] L. Wang, X. Wang, N. Ma, W. Zheng, D. Jin, and Y. Zhao, "Influence of various substrate materials on the structure and magnetic properties of fe–n thin films deposited by dc magnetron sputtering," *Surface and Coatings Technology*, vol. 201, no. 3-4, pp. 786–791, 2006. 146